Optical Properties of Atmospheric Aerosol using Laser Tweezers

Megan Rose McGrory

A thesis submitted for the degree of Doctor of Philosophy at the University of London

Royal Holloway, University of London

Declaration of Authorship

I, Megan Rose McGrory, hereby declare that this thesis and the work presented in it is entirely my own unless otherwise stated. My contributions to the four co-authored papers that make up the body of this thesis are stated clearly on the cover page of each paper.

Signed:

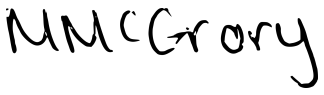

Date: 23-09-2021

Acknowledgments

First of all, I would like to thank my supervisors, Martin and Andy, for giving me this opportunity and for their guidance, patience, and support over the past four years.

I also would not have gotten through this PhD without my friends and office-mates at RAL and Royal Holloway, Zoë, Connor, Amy, Alasdair, Stephen, and Sumanth, who have filled the past four years with so many great memories and were always there to offer support when needed.

My Kiwi and Derry girls; Fran, Seánan, Mollie, Becca and Brenda have all given me so much encouragement and I am so grateful to be surrounded by such strong, kind, and supportive women.

I also want to thank my family, especially my parents, without whose support I would not have been able to even consider doing a PhD. Knowing that my mum is always there to answer my many phonecalls has made the past four years much easier.

Finally, I am grateful to Will for so much, but particularly his help, support and endless patience for all my programming questions, for always finding a way to make me feel better in hard or stressful times, and for providing unlimited encouragement throughout this PhD, especially over the final few months.

Abstract

Atmospheric aerosol is understood to have a significant impact on the Earths climate by directly scattering solar radiation and by acting as cloud condensation nuclei. However, despite decades of research, the impact of atmospheric aerosol remains the most uncertain area of climate science by far. The work presented in this thesis focuses on the scattering of light by aerosol particles. There are many factors affecting how a given aerosol particle will scatter light, including composition, size and morphology. It is therefore necessary for many different studies of various aerosol systems to be carried out to obtain a full understanding of the impact of atmospheric aerosol on the Earths climate. This thesis presents studies on multiple aerosol systems, each providing unique insights into the scattering of light by atmospheric aerosol. A new computational method of determining the optical properties of both homogeneous and core-shell aerosol from their Mie spectra, has also been developed. In all studies in this thesis, optical trapping, Mie spectroscopy, and computational modelling of Mie spectra were used to determine the size and refractive index of aerosol particles. The collective aim of these studies is to decrease the uncertainty of the impact of atmospheric aerosol in climate modelling.

The first and second papers present the study of the optical properties of inorganic homogeneous aerosol particles which are often used as aerosol proxies or for calibration in atmospheric aerosol experiments. Firstly, the optical properties of polystyrene beads were determined as a function of temperature, providing information which will allow for more accurate calibration of aerosol measuring equipment, as well as showcasing a new experimental technique for studying airborne particles at varying temperature. Next, a comprehensive study was carried out on the reliability of the optical properties of four brands of commercially available silica beads.

In the third and fourth papers, polystyrene and silica beads were used to study the Mie scattering of core-shell particles. Firstly, sulfuric acid was shown to form a core-shell morphology when deposited on a silica particle, and to not form a core-shell particle when deposited on a polystyrene particle. Finally, in an unprecedented study, two different real-world samples of organic aerosol, one collected from an urban area (greater London) and the other from burning wood, were both shown to form core-shell particles when deposited on mineral silica particles. The organic core-shell particles were also shown to maintain core-shell morphology

upon oxidation with ozone, an atmospheric oxidant. The morphology of aerosol particles significantly impacts how they interact with light: therefore both of these studies provide insight for the modelling of composite organic/mineral aerosol.

Contents

List of Figures

Chapter 1: Introduction

Chapter 2: Methodology

demonstrated in the top panel. Experimental Mie spectrum of example Whitehouse silica bead with and without adaptive baseline applied shown in the bottom panel.

Figure 2.12: Two-dimensional cross section of the four-dimensional parameter space searched by the grid-scan fitting method.

Figure 2.13: Experimental Mie spectrum of an example Corpuscular silica bead compared with the theoretical best fit spectrum determined from the grid-scan fitting method.

Figure 2.14: Example demonstrating the method used to find the refractive index at a single peak.

Figure 2.15: Example Cauchy curves fitted to refractive indices determined at each peak in a given spectrum as a function of wavelength.

Figure 2.16: Demonstration of the phenomenon discovered that core-shell spectra are much more sensitive to shell thickness than refractive index.

Figure 2.17: Plot of average peak dierence against refractive index for core-shell particles with a 1 nm shell of refractive indices of 1.52 and 1.6.

Chapter 3: Using Mie scattering to measure the wavelength dependant refractive index of polystyrene beads with changing temperature

Figure 0: Table of contents graphic

Figure 1: Optical set-up of laser trap.

Figure 2: Schematic of the cross section of the aluminium trapping cell demonstrating the positioning of the heater.

Figure 3: Change in experimental and calculated Mie spectra, and corresponding Cauchy curves at 22 °C, 100 °C, 176 °C and 234 °C.

Figure 4: The refractive index at 589 nm for all polystyrene beads as a function of temperature.

Figure 5: Cauchy equation parameters A, B/λ^2 and C/λ^4, as a function of temperature.

Figure 6: Radius as a function of temperature for example polystyrene bead, compared with radii based on literature values for the volumetric

thermal expansion coefficient.

Chapter 4: Variation in the size and refractive index of laser trapped silica and glass beads

Figure 1: Example experimental spectrum from each of the bead samples compared with its corresponding theoretically generated spectrum (dashed) of known size and refractive index values.

Figure 2: Cauchy curves showing the wavelength-dependent refractive index of all beads studied, compared with results from Malitsons study on bulk silica (dashed).

Figure 3: Determined radius distribution of all beads studied plotted as bar graphs. The manufacturers values of radius with associated uncertainties are plotted as Gaussian curves for comparison.

Chapter 5: Atmospheric organic matter may form core-shell aerosol particles on mineral surfaces

Figure 0: Table of contents graphic

Figure 1: Typical experimental Mie spectra for two-phase particles created using the aged urban and wood-smoke aerosol samples. The dashed spectra show the corresponding theoretical fit for both spectra generated using core-shell theory.

Figure 2: Mie spectra of silica core, silica/urban aerosol core-shell particle A before reaction and 120s after reaction, demonstrating that the thin film was removed from surface, leaving silica core.

Figure 3: Change in refractive index and shell thickness of both urban and wood-smoke samples as they were oxidised with gas-phase ozone.

Figure 4: Cauchy curves showing the wavelength-dependent refractive index of the organic samples used in this study compared with the determined refractive index of similar samplesused in previous work.

Supplementary Figure 1: Optical set-up used for trapping in air.

Supplementary Figure 2: Silica/wood-smoke core-shell particles became more stable as the shell thickness was increased with multiple collisions.

Supplementary Figure 3: Mie spectra of silica core, silica/urban aerosol core-shell particle B before reaction and 120s after reaction, demonstrating that the thin film was not removed from surface completely, leaving a core-shell particle.

Supplementary Figure 4: Mie spectra of silica core, silica/urban aerosol core-shell particle C before reaction and 120s after reaction, demonstrating that the thin film was not removed from surface completely, leaving a core-shell particle.

Supplementary Figure 5: The top panel shows a plot of refractive index against average peak difference for a range of shell thickness between 1 nm and 50 nm. The bottom panel demonstrates that an equally clear minimum average peak difference can be determined for any thickness of shell from 1 nm.

Chapter 6: Mie scattering from optically levitated mixed sulfuric acid-silica core-shell aerosols: confirmation of core-shell morphology for atmospheric science

Figure 1: Measured and simulated Mie spectra for optically trapped sulfuric acid aerosols.

Figure 2: Experimental refractive index of trapped sulfuric acid aerosols as a function of wavelength are compared to literature values for aqueous sulfuric acid solutions that have different mass ratios of sulfuric acid to water.

Figure 3: Mie spectra showing how the Mie scattering of silica aerosol alters upon growth of a film of sulfuric acid. Core-shell Mie theory was applied to determine thickness of the developing shell.

Figure 4: Graphs depicting (a) the Mie-theory simulated spectra for sulfuric acid film development on the experimental obtained Mie spectrum for pure polystyrene and (b) the experimentally obtained Mie spectra for the growth of a film of sulfuric acid on polystyrene.

Figure 5: The scattering efficiency of a silica, a sulfuric acid and core-shell silica-sulfuric acid aerosol particle as a function of median aerosol diameter.

List of Tables

Chapter 3: Using Mie scattering to measure the wavelength dependant refractive index of polystyrene beads with changing temperature

Chapter 4: Variation in the size and refractive index of laser trapped silica and glass beads

Chapter 5: Mie scattering from optically levitated mixed sulfuric acid-silica core-shell aerosols: confirmation of core-shell morphology for atmospheric science

Chapter 1

Introduction

Atmospheric aerosol is defined as any solid or liquid particles suspended in the Earth's gaseous atmosphere. Atmospheric aerosol significantly impacts the Earth's climate in two ways; direct scattering of solar radiation, and by acting as cloud condensation nuclei [1]. The effects of atmospheric aerosol are the greatest source of uncertainty in climate modelling [2]. This is partially due to the large variety of factors affecting atmospheric aerosol which are difficult to measure exactly or predict. For example, organic thin films of varying compositions forming on atmospheric aerosol particles or the oxidation of atmospheric aerosol can both completely change the optical properties of the aerosol. The purpose of this thesis is to study the optical properties of specific aerosol systems with a focus on core-shell particle morphology to provide new insights into the direct scattering of solar radiation and thus the radiative forcing of certain atmospheric aerosol systems.

The optical properties of atmospheric aerosol, such as size and refractive index, determine how they will scatter light [1]. For the experiments described in this thesis, optical trapping, Mie spectroscopy and computational modelling of homogeneous and core-shell Mie spectra were used to determine the optical properties of different aerosol systems.

1.1 Atmospheric layers and composition

The Earth's atmosphere is a layer of gas surrounding the Earth. It is predominantly composed of nitrogen (78%), oxygen (21%) and noble gases (0.9%), the amounts of which seem to remain largely unchanged with time

[1]. The other 0.1% is made up of trace amounts of other gases, including carbon dioxide, methane, ammonia and many others, the amounts of which present in the atmosphere at a given time are much more varied. The concentration of these trace gases varies due to natural physical, chemical and biological processes both on the Earth's surface, *e.g.* volcanic exhalation, and in the atmosphere, *e.g.* particle formation. There are also variations due to pollution of the atmosphere caused by human activity. For example, in recent years large increases in the amount of CO_2 in the atmosphere due to human activity have been recorded [1].

The Earth's atmosphere is split into layers based on changes in temperature and pressure, as shown in Figure 1.1. The precise altitude of a layer's boundaries varies slightly depending on latitude and the time of year. The troposphere (10–15 km) contains almost all of the water, clouds, and aerosol present in the atmosphere. In the troposphere turbulence, humidity and temperature are all heavily influenced by the Earth's surface. The stratosphere (15–55 km) is home to the ozone layer and contains a significant amount of sulfuric acid aerosol droplets [3]. The mesosphere (55–90 km) is the coldest point in the atmosphere. Above the mesosphere is the thermosphere, where absorption of short-wave radiation causes high temperatures. The ionosphere is a section of the upper mesosphere and lower thermosphere where ions are produced by photoionization. The exosphere is the outermost layer of the atmosphere, where gas molecules with sufficient energy are able to overcome Earth's gravitational force and escape. The tropopause, stratopause, and mesopause are the boundaries between the atmospheric layers [1].

1.2 Radiative forcing by atmospheric aerosol

The temperature of the Earth is determined by the amount of solar radiation entering and leaving the Earth's atmosphere, which is subject to change over time. Perturbations in the atmosphere, such as an increase in the concentration of a particular gas or aerosol, can cause the balance to shift in either direction. As defined by the Intergovernmental Panel on Climate Change (IPCC), Radiative forcing quantifies the change in energy fluxes caused by changes in these drivers (such as gas and aerosol concentrations) for 2011 relative to 1750. Radiative forcing can also be expressed in Watts per square meter (Wm^{-2}) [2]. The amount of radiation entering the top of the atmosphere is basically constant, although the amount

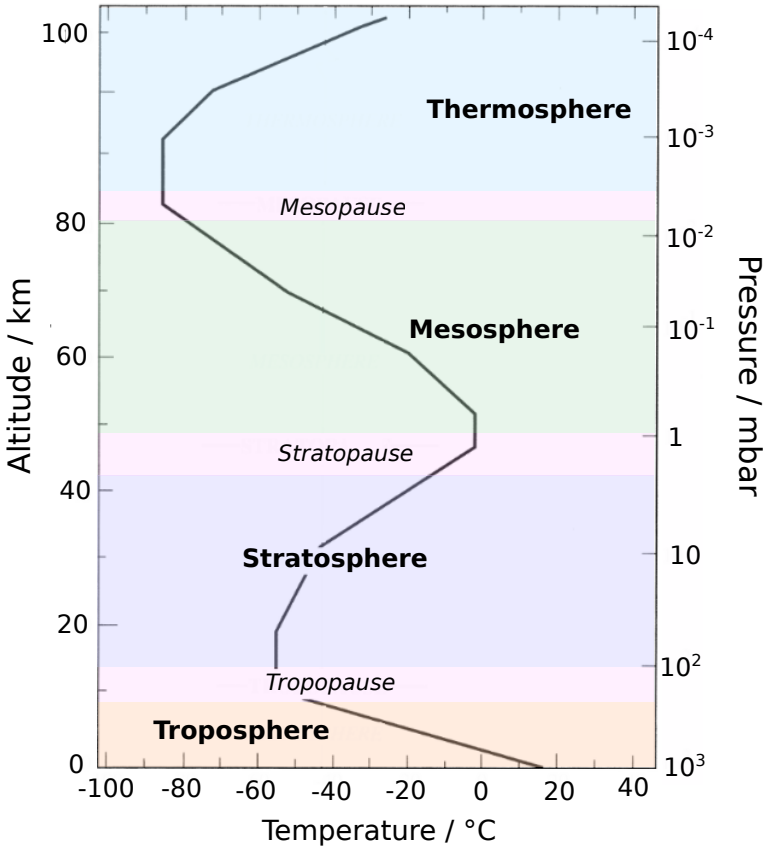

Figure 1.1: Temperature and pressure of the layers of the Earth's atmosphere [1]

leaving is variable. The Earth is currently experiencing positive radiative forcing, as more heat is being trapped in the Earth's atmosphere than is leaving [2, 4]. The total anthropogenic radiative forcing has increased dramatically from 0.57 Wm^{-2} in 1970 to 2.29 Wm^{-2} in 2011.

Atmospheric aerosol has been found to have a huge impact on radiative forcing in two major ways. The first is through reflection and scattering of light [4, 5, 6], and the second is through acting as cloud condensation nuclei (CCN) [7]. The radiative forcing of the total aerosol effect in the atmosphere is 0.9 Wm^{-2}. Figure 1.2 is a graphic from an IPCC report which shows that aerosol-cloud and aerosol-radiation interactions have the largest sources of uncertainty of any radiative forcing agent. Therefore, understanding the radiative forcing caused by atmospheric aerosol is key for the development of accurate climate modelling.

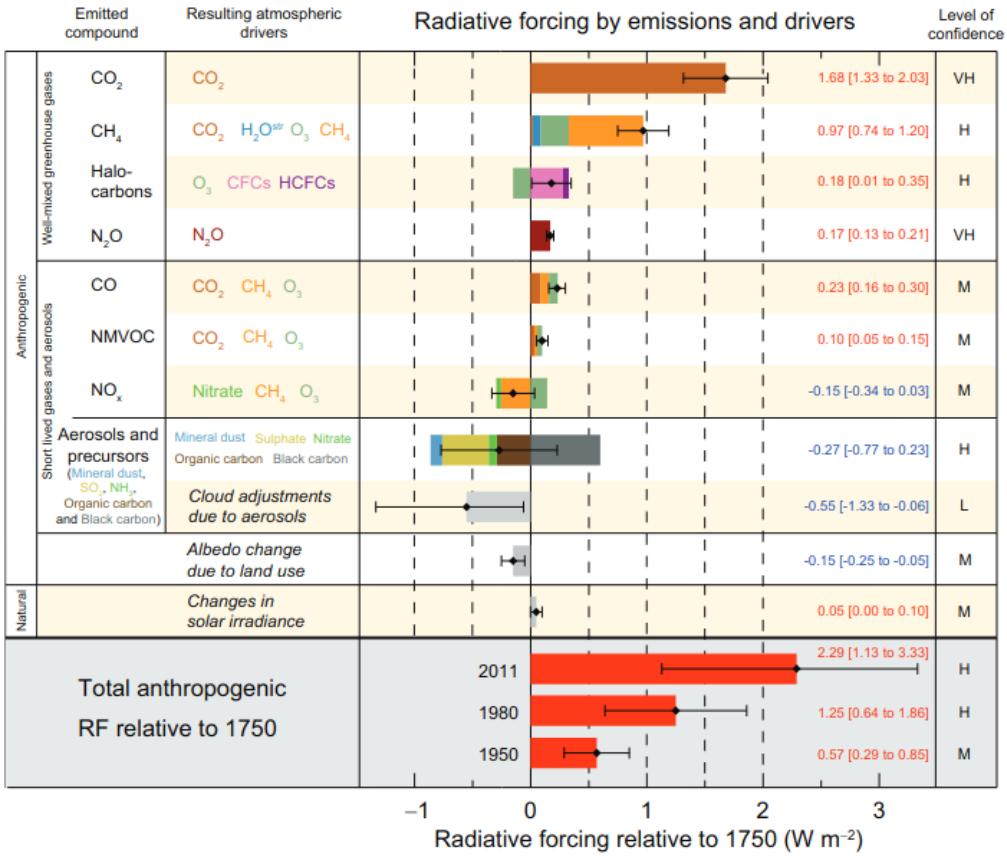

Figure 1.2: Graphic from IPCC report comparing the radiative forcing and associated uncertainties of different forcing agents. Aerosol interactions are shown to have a significantly larger percentage uncertainties than other forcing agents. The level of confidence in the net forcing from each forcing agent is given, where L is low, M is medium, H is high, and VH is very high [2]

1.3 Sources of atmospheric aerosol

The ways in which atmospheric aerosol will scatter light and interact with water vapour to act as CCN are both dependent on the particles size and composition. The work in this thesis will focus on the scattering of light by atmospheric aerosol, therefore the size and refractive index, which is defined by the aerosol composition, are the most important factors to consider.

There is a vast range of sizes (typically 0.01¯m to 100¯m) of atmospheric aerosol particles. There are four main size categories, called "modes", by

which atmospheric aerosol particles are sorted. These are further subcategorized into "fine" and "coarse" modes. The fine modes are the nucleation ($1-10\,\text{nm}$) and Aitken ($10-100\,\text{nm}$) modes, the smallest sizes by far. Although particles in the fine modes make up by far the largest proportion of atmospheric aerosol in terms of numeric quantity, due to their relatively smaller size than those in the coarse mode they make up only a few percent of the total mass of all atmospheric aerosol. The coarse modes include larger particles in the accumulation ($100 - 1,000\,\text{nm}$) and large coarse ($1,000 - 10,000\,\text{nm}$) modes. Aerosol in the accumulation mode is generally created by the condensation or coagulation of Aitken mode particles. Large coarse mode aerosol is produced from condensation or coagulation of accumulation mode aerosol as well as primary sources such as sea-salt and volcanic ash [1].

Atmospheric aerosol is found in the two lowest layers of the atmosphere, the troposphere (0–15 km) and the stratosphere (15–55 km). Each of these layers have different sources of aerosol. The composition, and therefore refractive index, of atmospheric aerosol varies significantly depending on their source. Aerosol can be described as either primary or secondary atmospheric aerosol dependent on its source or mechanism by which it was produced. Primary aerosol are in the original state in which they were emitted into the atmosphere. Direct emission of aerosol is therefore a primary source, for example, sea spray or desert sand. Secondary aerosol is not in its original form, and most primary aerosol will at some point undergo a chemical reaction, becoming secondary aerosol. There are a number of secondary sources of atmospheric aerosol, including gas to particle conversion by the oxidation of gas-phase species [1].

Tropospheric aerosol has many sources, which vary depending on region. For example, aerosol in an urban area will have a much higher percentage of particles from anthropogenic sources, such as the burning of fossil fuels, wood, and petrol and diesel in cars. Aerosol categorized as marine, rural, remote, and polar will have a much higher percentage of aerosol particles from natural sources such as dust, pollen, sea spray and sand [1]. A study by Shepherd *et al.* [8] found aerosol samples from urban, remote, and wood-smoke sources to each have significantly different refractive indices, with a general increase from remote to urban to wood-smoke.

Stratospheric aerosol is made up of a very high percentage of sulfuric acid droplets, sourced from volcanic eruptions and from transfer of sul-

fur from tropospheric aerosol [9, 10, 11]. After volcanic eruptions sharp increases in the amount of sulfuric acid droplets in the stratosphere have been observed [3]. There are also many mineral aerosol particles in the stratosphere introduced by volcanic eruptions [12]. Therefore, mixing of sulfuric acid with mineral aerosol in the stratosphere is a common occurrence [10]. The morphology adopted, and therefore the effect on the scattering of light by a sulfuric acid droplet when it is deposited on a mineral particle is unknown. The effect of sulfuric acid deposited onto mineral aerosol is studied in paper 4 in this thesis.

As there are such a wide range of sizes and composition of atmospheric aerosol particles, many studies are needed on a wide range of atmospheric aerosol from different sources for a full understanding of the properties of aerosol present in the atmosphere. The interactions between different aerosol particles are also an important area of study to gain a complete understanding of the impact of aerosol on the Earth's climate.

1.4 Cloud Condensation Nuclei

Atmospheric aerosol particles act as a surface for water vapour in the atmosphere to condense on to, to form visible water droplets (clouds, fogs etc.). Atmospheric aerosol is necessary for the formation of clouds as water vapour cannot spontaneously nucleate (on Earth). Although the research carried out in this thesis is focused on the scattering of light by aerosol particles, a brief background on atmospheric aerosol acting as cloud condensation nuclei is provided here as this is an equally important area of study for understanding how atmospheric aerosol impacts the Earth's radiative balance.

Size, morphology, and composition have been shown to be the determining factors in the effectiveness of atmospheric aerosol as cloud condensation nuclei (CCN) [7]. A study carried out by Ervens *et al.* [13] compared the aerosol size distribution with the CCN concentration at Chebogue Point, Nova Scotia. A substantial increase in the concentration of CCN was found to correlate with an increase in the size of the aerosol present. A study carried out by Altaf *et al.* [14] compared homogeneous and phase-separated particles as CCN and found particle morphology to have a large impact on the ability of aerosol particles to act as CCN.

The phenomenon of aerosol acting as CCN is described mathematically

by the Kelvin equation,

$$\ln\frac{p}{p_0} = \frac{2\gamma V_m}{rRT}, \tag{1.1}$$

where p is the vapour pressure of the liquid (water in the case of CCN), p_0 is the saturated vapour pressure (vapour pressure on a flat surface), γ is surface tension of the liquid, V_m is the molar volume of the liquid (water), r is the radius of the droplet, R is the universal gas constant, and T is temperature. The Kelvin equation only holds for spheres so atmospheric aerosol particles must be assumed to be spherical for the purpose of this calculation.

Equation 1.1 describes how vapour pressure of H_2O changes due to a curved liquid-vapour interface, as exists in approximately spherical CCN, where a liquid with a high vapour pressure will evaporate more readily than one with a low vapour pressure. As the radius of the particle and the vapour pressure are inversely proportional, a particle with a lower radius will have a higher vapour pressure and will evaporate more readily. Therefore, larger aerosol are more stable, and last longer as CCN. This theory matches with the results found on the effect of particle size on their ability to act as CCN by Ervens *et al.* [13].

Another important factor is the chemical composition of the droplet formed, as substances within the aerosol can potentially react with the water to form impurities. Other substances in the atmosphere can also contaminate the water vapour. Typically, a chemical contaminating the particle will lower the vapour pressure of water, making it less stable as a CNN, as demonstrated by Raoult's law,

$$p_i = p_i^* x_i, \tag{1.2}$$

where p_i is the partial vapour pressure of component i, p_i^* is the vapour pressure of the pure component i and x_i is the mole fraction of component i in the solution. It is therefore easier for droplets to form on insoluble particles, as they will not react with and contaminate the water droplet formed. This idea will be explored further in Section 1.6 where the effect of organic thin films on solid particles is discussed.

A formulation of Köhler theory,

$$\ln\frac{p_w D_p}{p_0} = \frac{4M_w\sigma_w}{RT\rho_w D_p} - \frac{6n_s M_w}{\pi\rho_w D_p^3}, \tag{1.3}$$

incorporates both the impact of curvature and composition by combining the Kelvin and Raoult's equations, where p_w is vapour pressure of the

droplet, D_p is the diameter of the droplet, p_0 is the saturation vapour pressure M_w is the molecular weight of water, σ_W is the surface tension of the droplet, ρ_w is the density of pure water and n_s is the number of moles of the impurity.

Atmospheric aerosol acting as cloud condensation nuclei is still far from completely understood and is therefore an active area of research in climate science. New behaviours and phenomena are continuously being discovered. For example, a study on the impact of chemical composition on CNN in a suburban area in China by Li *et al.* [15], found that particle size and chemical composition showed different effects on the CCN activation ratios in the morning and the afternoon which was not anticipated and led to an interesting area of further study. As demonstrated in Figure 1.2, aerosol-cloud interactions are equally as urgent an area of study for the understanding of aerosol effects on the Earth's climate as aerosol-radiation interactions. However, the work carried out in this thesis is focused on aerosol-radiation interactions.

1.5 Attenuation of light by atmospheric aerosol

Aerosol particles scatter light differently depending on their size parameter, x, where,

$$x = \frac{2\pi r}{\lambda}, \tag{1.4}$$

where r is radius of particle and λ is the wavelength of incident light. For particles which are much smaller than the wavelength of the incident light and therefore have a size parameter $\ll 1$, the Rayleigh approximation,

$$I = I_0 \left(\frac{1+\cos^2\theta}{2R^2}\right)\left(\frac{2\pi}{\lambda}\right)^4\left(\frac{n^2-1}{n^2+2}\right)^2\left(\frac{d}{2}\right)^6 \tag{1.5}$$

can be applied to model the intensity of scattered light, where I is the intensity of the scattered light, I_0 is the intensity of the light before interaction with the particle, θ is the angle of scattering, R is the distance to the particle, λ is the wavelength of incident light, n is the relative refractive index (n of particle/n of medium) of the particle and d is the diameter of the particle [16]. Particles which are approximately the same size as the wavelength of incident light will have a size parameter $\simeq 1$ and will scatter light according to Mie theory. Particles which are much larger than the wavelength of incident light will have a size parameter $\gg 1$ and will follow optical laws of light scattering [16].

For visible light interacting with atmospheric aerosol, Mie scattering is the dominant form of light scattering due to the size of particles of atmospheric aerosol being close to the wavelength of visible light ($\sim$ 0.5µm). The key parameters needed to calculate the Mie scattering of a particle are the size and refractive index. A detailed formalism of Mie scattering theory is given in section 2.4.

Determining the refractive index of aerosol particles is key to understanding how they interact with light, as the refractive index is a numerical expression of light scattering and absorption properties. Refractive index is a complex value, $n = m + ki$, where m and k are the real and imaginary components of the refractive index, describing the phase velocity of light in matter and light absorption respectively and $i = \sqrt{-1}$. Refractive index varies with wavelength.

The Sellmeier equation [17] described by Wilhelm Sellmeier in 1872,

$$n^2 = 1 + \sum_i \frac{A_i \lambda^2}{\lambda^2 - \lambda_i^2}, \tag{1.6}$$

where n is the refractive index, λ_i is the wavelength at which a natural frequency occurs in the material and A_i is a constant proportional to the number of oscillators capable of vibrating at these natural frequencies, describes the relationship between refractive index and the wavelength of incident light.

The Cauchy equation [17] first described by Augustin-Louis Cauchy in 1836,

$$n(\lambda) = A + \frac{B}{\lambda^2} + \frac{C}{\lambda^4}, \tag{1.7}$$

where $n(\lambda)$ is the refractive index, λ is the wavelength, and A, B and C are material dependent constants is a special case of the Sellmeier equation where only the first two terms of the expanded Sellmeier equation are considered and the absorption of light by the material is not accounted for [17].

The Sellmeier equation is more widely applicable than the Cauchy equation. However, when studying the real part of the refractive index in the visible wavelength range the Cauchy equation holds and can be used to accurately describe the real part of the wavelength-dependent refractive index of both light-absorbing and non-light-absorbing aerosol. As the Cauchy equation has less terms than the Sellmeier equation, it is less computationally demanding and therefore an appropriate choice for analysis

of the refractive index of atmospheric aerosol, and is thus commonly used as such [18, 19, 20, 21, 22, 23].

The absorption of light by atmospheric aerosol is important for fully understanding the impact of atmospheric aerosol on radiative forcing. The specific absorption properties of numerous types of aerosol, for example, ambient atmospheric aerosol in a suburban environment [24, 25], brown carbon [26, 27], pollution plumes from the mainland Asian continent [28], and biomass burning emissions [29, 30] have been studied and it has been found that the absorption properties of aerosol are dependent on the chemical composition of the aerosol particle [25, 27, 28, 29, 31, 32], the particle morphology [26, 33, 34, 28], and the size of the aerosol particle [34, 30].

For the work carried out in this thesis, only the real component of the refractive index was studied, as this provides sufficient information to determine the light scattering properties of the aerosol being studied.

1.6 Morphology of atmospheric aerosol

Most calculations of atmospheric light scattering in atmospheric and climate modelling assume spherical homogeneous particles [35]. However, collisions between atmospheric aerosol leads to the formation of non-homogeneous two-phase particles with complex morphologies, typically either core-shell, where a thin film of organic material coats the surface of a spherical solid core, partially-engulfed, where organic material beads up on the surface of the spherical solid core, or liquid-liquid partially-engulfed [36, 37, 38]. Figure 1.3 shows a depiction of the potential two-phase particle morphologies. The morphology of aerosol particles has been shown to have a significant impact on the optical properties, and thus radiative forcing of atmospheric aerosol [39, 37, 40, 41, 42].

There is evidence for both partially-engulfed and core-shell morphology of atmospheric aerosol. Partially-engulfed particles has been shown to form in laboratory experiments. Laskina *et al.* [43] found two-phase particles of ammonium sulfate with succinic acid to phase separate from homogeneous to partially-engulfed morphology due to crystallization of the organic component if the particle is large enough. This is in agreement with work carried out by Veghte *et al.* [41] where organic aerosol composed of ammonium sulfate internally mixed with succinic or pimelic acid was found to undergo phase separation and form a partially-engulfed

Figure 1.3: Schematic of different morphologies of two-phase aerosol particles. From left to right; core-shell with solid core and liquid shell, partially-engulfed with solid core and liquid on surface, partially-engulfed with solid core and liquid droplet on surface, liquid-liquid two-phase particle.

morphology if the particle was large enough (>170 nm for succinic acid and >270 nm for pimelic acid) demonstrating that phase separation of aerosol particles is heavily size dependent. Reid *et al.* [36] found partially-engulfed morphology to be the dominant morphology for two-phase particles of a range organic compounds (including saturated and unsaturated hydrocarbons, aromatics, alcohols, ketones, carboxylic acids, esters, and amines). Dennis-Smither *et al.* [44] found the coagulation of oleic acid aerosol with an aqueous sodium chloride droplet to form a phase-separated particle with two partially-engulfed liquid phases.

In the third and fourth papers in this thesis, two examples of atmospherically realistic two-phase particles were formed and were both shown to adopt a core-shell morphology. Therefore, core-shell morphology is the main focus of the work carried out in this thesis.

Core-shell morphology

There have been many previous experimental studies of core-shell particles created with pure chemical compounds [45, 46, 47, 48, 49, 15, 44, 41, 50, 51, 52, 53, 54, 55, 56, 57, 58, 59, 60] which have shown thin films on aerosol particles to have a significant effect on the physical and chemical properties of aerosol. It is therefore essential to understand core-shell particles, in terms of their source, composition and how they form. Owing to the ability of organic aerosol to attach to almost any particle, thin films on atmospheric aerosol almost all have an organic composition. There are multiple sources of organic thin-film forming aerosol, including vegetation waxes and photo-oxidised emissions from the burning of fossil fuels.

The sea-surface layer is also an abundant source of organic aerosol, such as the fatty acids which reside at the surface of the ocean [61].

Different methods have been developed for the study of thin films of organic material. One of the earliest studies was carried out by Hansen and Shu [62] in 1975, where they used electron microscopy to measure the differences in how smog and haze particles scattered light. They detected that the smog aerosol was comprised of solid spheres and the particles of haze aerosol were hollow, and this caused them to scatter light in different ways, representative of their unique morphologies. This was taken as indirect evidence of thin films on atmospheric aerosol. The same technique was used by Posfai [63] to study organic coatings on ammonium sulphate aerosol collected from above the North Atlantic Ocean, whose results supported those of Hansen and Shu.

Further evidence for organic thin films on atmospheric aerosol was found by Capel *et al.* [64], when surface tension techniques were used to determine that the surface tension of fog aerosol collected from an urban area of Zurich was less than that of pure water. This implies that the air-water interface of the aerosol particles were covered with organic chemicals. The exact chemical composition of thin films is still somewhat unclear and is the focus of much current research in the field. For example, Takahama *et al.* [65] used scanning transmission x-ray microscopy along with near edge x-ray absorption fine structure spectroscopy to determine the chemical structure of 636 aerosol samples. A large variation in organic mass fraction of the particles was found, with over half being nearly spherical, and all films were found to be under $0.6\mu m$ in thickness and accounted for between 1% and 98% of the volume of the particle.

Davies *et al.* [57] carried out a study measuring the influence of organic films on the evaporation and condensation of water from aerosol particles. The presence of an organic thin film was found to significantly reduce the rate of evaporation of water from the surface of a particle. This study also found a surprising result, that the presence of a multi-component organic thin film prevented the condensation of water on the particle surface, and therefore allowed the particle to successfully act as cloud condensation nuclei. This is contrary to Raoult's law which states that an increase in organic substance on the particle surface will make the particle less able to act as cloud condensation nuclei. This is in line with work carried out by Cruz and Pandis [66] which found that the extent to which thin films alter the cloud condensation nuclei activation potential of the aerosol, is

dependent on the exact composition of the film. While Raoult's law holds for many particles, thin films do not necessarily hinder the cloud condensation nuclei activation potential of aerosol in all cases. For example $(NH_4)_2SO_4$ particles coated in a thick layer of dioctylphthalate did not experience any change in potential to act as cloud condensation nuclei [66].

A study carried out by Donaldson measuring the adsorption of atmospheric gases at the airwater interface of NH_3 showed that thin films inhibit the movement of chemicals from the gas to liquid phase of the aerosol [67]. Thin films have been found to reduce the scavenging of the aerosol by larger cloud droplet [59]. Thin films have also been shown to impact the optical properties of atmospheric aerosol. A study carried out by Jones *et al.* [68] used optical trapping to measure the Mie scattering of atmospheric core-shell particles. The addition of an organic thin film to silica particles was found to significantly change the Mie scattering of the aerosol.

In the fourth paper in this thesis the deposition of sulfuric acid onto both silica and polystyrene aerosol is studied, where silica acts as a proxy for mineral aerosol. A significant change in Mie scattering was shown as the shell was slowly built up over multiple collisions with a silica particle. This study also found that sulfuric acid deposited onto polystyrene particles did not form a core-shell and is suspected to have formed a partially-engulfed particle. All the previous studies mentioned used aerosol proxies to study core-shell particles. In paper 3 in this thesis core-shell particles made from silica and real atmospheric samples are studied, providing valuable confirmation of core-shell morphology of atmospherically realistic two-phase aerosol particles.

1.7 Effect of temperature on atmospheric aerosol

Temperature has been shown to affect the properties of atmospheric aerosol in a number of ways. Changes in chemical and physical properties in atmospheric aerosol will impact its refractive index, and hence its ability to scatter light. The temperature dependence of refractive index of atmospheric aerosol is therefore vital for correct modeling of the scattering of light by atmospheric aerosol under different temperature conditions.

There are many reactions that can take place in the atmosphere that may change the physical properties of the aerosol articles, creating secondary organic aerosol. This of course will have an impact in the refractive

index of the particles, and thus how they scatter light. Takekawa *et al.* [69] determined that temperature is one of the most important factors in secondary organic aerosol (SOA) formation. The SOA yield from the photooxidation of hydrocarbons in a temperature-controlled smog chamber was studied and it was found that a much higher SOA yield was obtained at lower temperatures. Under the condition of the same SOA concentration, the SOA yield at 283 K was approximately twice that at 303 K. Sheehan *et al.* [70] have also shown that the concentration of SOA present in the atmosphere is heavily influenced by temperature using an absorptive-partitioning model. The model simulations show that temperature is likely to have a significant influence on SOA partitioning, and therefore the resulting SOA concentration in the atmosphere, with a 10 °C decrease in temperature estimated to increase SOA yields by 20 – 150%, depending on the vaporization enthalpy. Studies by Yue *et al.* [9] and Russell *et al.* [71] have shown the properties of stratospheric aerosol, including refractive index, to change as a function of altitude, and therefore temperature.

It is clear that temperature has an impact on the properties of atmospheric aerosol particles, and thus how they scatter light. It would therefore be beneficial to be able to study individual particles for a more in depth look at the temperature dependence of different types of atmospheric aerosol. A method is described in paper 1 in this thesis which allows for the scattering of light by individual particles to be studied at varying temperature (20 – 240 °C). Polystyrene is used as a test aerosol for the system in the paper, however there is potential for the study of atmospheric particles produced at high temperatures to be studied. For example, aerosol produced by wildfires, and how the sudden increase in temperature produced by wildfires will affect other atmospheric aerosol in the region.

1.8 Oxidation of atmospheric aerosol

Oxidation can significantly alter the physical and chemical properties of atmospheric aerosol particles, forming secondary organic aerosol (SOA) [72]. Ozone (O_3), nitrates (NO_3) and OH radicals are the most highly studied atmospheric oxidants that affect the optical properties of atmospheric aerosol [72].

Oxidation has been shown to cause an increase in the refractive index of atmospheric aerosol particles. A study carried out by Flores *et al.* [73]

found the refractive index of a mixture of biogenic volatile organic compounds (α-pinene and limonene) to increase as it was oxidised with ozone. Another study by Kim *et al.* [74] also found the refractive index of atmospheric aerosol proxies to generally increase upon oxidation, from about 1.4 to 1.53 for α-pinene, 1.38 to 1.53 for β-pinene, and 1.4 to 1.6 for toluene, when oxidised with ozone. Kim *et al.* [74] also found the refractive index of SOA to be affected by a number of factors, including mass concentration, oxidation chemistry, temperature, and aerosol aging [74]. In contrast, a study by Lambe *et al.* on the oxidation of gas-phase precursors used as surrogates for anthropogenic (naphthalene, tricyclodecane), biomass burning (guaiacol), and biogenic (α-pinene) emissions aerosol, found the real refractive index to decrease and the imaginary refractive index to increase upon oxidation by OH radicals.

A study by Nakayama *et al.* [75] found SOA generated by the oxidation of isoprene by OH, O_3, and NO_3, to have a difference in the imaginary part of refractive index depending on if it was formed in the presence of SO_2. Oxidation was found to have a negligible effect on the refractive index of isoprene, unless reacting in the presence of SO_2, when a significant light absorption was observed during oxidation by OH radicals, and a much weaker absorption was observed during oxidation with O_3, and (NO_3). Varma *et al.* [76] determined the refractive index of secondary organic aerosols (SOA) formed by the NO_3 oxidation of β-pinene to be 1.61, which is significantly larger than the refractive index of SOA produced by similar methods. Varma *et al.* [76] suggest that this is potentially caused by a large proportion of organic nitrates in the particle phase.

There are clearly a number of factors which have been shown to affect the oxidation of atmospheric aerosol. It is therefore difficult to predict the impact of oxidation on the refractive index of atmospheric aerosol as there are countless potential reactions between different organic compositions of aerosol and oxidants with each having unique effects on the optical properties of the reacting aerosol. It is therefore important to study many different atmospheric oxidation reactions and formation of SOA to get a greater understanding of the properties and subsequently the environmental impact of highly oxidising aerosol [74, 77, 72].

All of the previous studies on the oxidation of atmospheric aerosol have used proxies in place of real atmospheric samples. Studies using real atmospheric samples are required for a true representation of the impact of oxidation on the optical properties of atmospheric aerosol. In the third

paper in this thesis the oxidation by O_3 of organic thin films on aerosol particles is studied. This study provides information on the oxidation of two specific aerosol systems, using real atmospheric samples.

Oxidation of core-shell particles

As discussed in Section 1.6, atmospheric aerosol can often adopt core-shell morphology. The reactivity of organic thin films can be quite different from that of bulk aerosol, owing to the fact that they are exposed to both chemical matter from within the aerosol as well as gas-phase radicals and solar radiation. The Köhler effects discussed in section 1.4 will also affect the reactivity of organic thin films. The vapour pressure of thin films on aerosol particles will potentially be higher than that of bulk aerosol, according to the Kelvin effect, as the organic material is on a curved surface. Changes in vapour pressure will cause changes in refractive index due to evaporation of different components from within the material.

It is therefore important to investigate the specific reaction of oxidants with thin films [58, 78, 79]. Nieto-Gligorovsk *et al.* [80] studied the reactions of organic films with ozone in the presence of simulated sunlight. They found the two different compositions of film studied to react differently to the same oxidation process, with 4-CB/catechol becoming more hydrophilic and 4-CB/4-phenoxyphenol becoming hydrophobic. This demonstrates the need for studies of many different compositions of core-shell particles to get a full understanding of their properties. Lim *et al.* [81] studied the oxidation of core-shell particles made of thin coatings of squalane on ammonium sulfate particles in a flow tube reactor and found the heterogeneous transformation of thin organic coatings on particles to be dramatically faster than that of pure organic particle. Gorkowski *et al.* [37] used optical trapping and Raman spectroscopy to study the morphology of phase-separated $\alpha-$pinene secondary organic aerosol at varying relative humidity. They used their results alongside literature values of oxidation of phase-separated secondary organic aerosol to suggest that as oxidation of phase-separated particles is increased the particles will have partially-engulfed, then core-shell, then homogeneous morphology. In the third paper in this thesis it is shown that organic material extracted from ambient aerosol forms core-shell aerosol when deposited on silica beads (used as a proxy for mineral aerosol). It was also shown that if a thick enough organic film is formed (> 10 nm) the particle can maintain a core-

shell structure during oxidation with gas-phase ozone.

1.9 Organization of this thesis

This thesis is comprised of an introduction chapter, a methodology chapter, four chapters written as papers with unpublished supplementary information included, and a conclusions chapter. The references for each of the paper chapters are included within that chapter. The references for the introduction, methodology and conclusions are included at the end in a thesis bibliography.

The first paper is a study of the temperature dependence of the real component of the refractive index of polystyrene beads. Polystyrene beads are commonly used for the calibration of aerosol monitoring equipment used in various climate and at various temperatures. This paper provides valuable information to ensure correct calibration of equipment when using polystyrene beads. This paper also describes a new technique for measuring the refractive index and size of aerosol particles as a function of temperature.

The second paper is a comparative study of different brands of commercially available silica beads, which are commonly used in many aerosol experiments, and are used in the third and fourth papers in this thesis as a mineral aerosol proxy. This paper offers detail on how reliable the different brands of beads are compared with their reported values of refractive index and size to offer users an accurate understanding of the properties of the beads they are using.

The third and fourth papers are studies of core-shell particles. The third studying real atmospheric samples on silica beads and the fourth paper studying sulfuric acid on silica and polystyrene beads. Both of these papers provide information on previously unstudied core-shell systems, and demonstrate a new method of determining the optical properties of core-shell particles.

1.10 Overall aims and objectives

The overall aim of the work carried out in this thesis is to provide new information which will reduce the uncertainty in the scattering of radiation

by atmospheric aerosol. The first way this will be achieved is through providing new experiential and computational methods which can be used to carry out complex analysis on atmospheric aerosol particles. The aim is to demonstrate techniques such that they can be used for future experiments to improve upon the accuracy of results, through improving instrument calibration, and by obtaining more accurate results through improved data analysis techniques. This will also be achieved through carrying out experiments on atmospheric aerosol using optical trapping, Mie spectroscopy and computational modelling of Mie scattering. Both the new methods are demonstrated and the experimental results can be used in different ways to help reduce the large uncertainty in climate modelling calculations caused by the scattering of radiation by atmospheric aerosol. This will be carried out by completing the following objectives:

1. Development and demonstration of a new technique for studying the size and wavelength dependent refractive index of airborne aerosol particles as a function of temperature.

2. Development and demonstration of a new program which can improve the analysis of Mie spectra, and allow for much more presice measurments of core-shell particles than was previously possible.

3. Determination of the wavelength and temperature dependant refractive index of polystyrene beads will allow for improvement in calibration of future experiments

4. An analysis of the refractive index and size dispersion of commerciality available silica beads will also allow for improvement in calibration of future experiments.

5. Two studies on two-phase atmospheric aerosol will also be carried out which will demonstrate the morphology adopted by two separate aerosol systems, including how organic matter acts upon oxidation, on the surface of solid mineral aerosol.

Chapter 2

Methodology

The study of single particles allows the properties and behaviours of atmospheric aerosol, such as size, composition, morphology and oxidation to be unambiguously determined [82]. In this thesis, optical trapping, Mie spectroscopy and computational modelling of Mie spectra have been used to determine the size and wavelength-dependent refractive index of individual aerosol particles of varying source, including organic and inorganic aerosol, and morphology, including homogeneous and core-shell particles.

2.1 Optical Trapping

Although the idea of light as photons acting as a particle and being able to exert pressure on matter was theorized many years earlier by Maxwell and Einstein [83], in 1900 Lebedev was the first to experimentally show that light is able to exert a "radiation pressure" on matter [84]. Ashkin was the first to demonstrate that this phenomena could be used to manipulate and trap particles. During experiments carried out between 1970 and 1975 [85, 86] Ashkin designed the first optical trap, where a particle is held in place by beams of light.

In the first experiments carried out, using the set up shown in Figure 2.1(a), Ashkin showed that beams of light were able to exert a large enough force on transparent latex spheres, suspended in water, to move them in the direction of the light beams. This was the expected result, due to the scattering force exerted on the particle, which acts in the direction of the beam and is proportional to the intensity of incident light. However, the experiment also revealed the unanticipated component of radiation pres-

sure, known as the gradient force, which acts perpendicular to the beam strongly pulling the particle into the high intensity region of the beam. The gradient force has an axial and transverse component, such that if the particle becomes either axially or radially displaced from the focus of the beam, the particle will focus or diverge the beam causing a restoring force to push the particle back into the focal point. From the discovery of the gradient force, Ashkin was then able to design a two-beam trap, shown in Figure 2.1(b), where small particles were held in the centre of the beams [85].

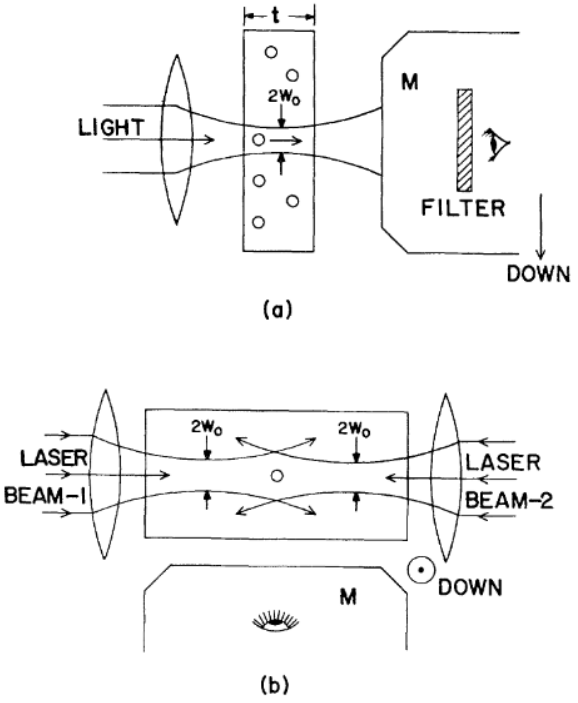

Figure 2.1: Experimental set up used by Ashkin to demonstrate movement (a) and optical trapping (b) of particles. The thickness of the glass cell, t = 120 µm, the microscope is marked M, and w_o is the radius of the laser beam (6.2 µm) [85]

In 1975 Ashkin and Dziedzic designed the levitation trap [86] which was able to levitate and trap large (up to 40 µm diameter) Mie and Rayleigh particles in air using a loosely focused beam. In levitation traps, particles are held in place balanced between the downwards force of gravity and the upwards scattering force from a single laser beam [87]. In a levitation trap the gradient force must exceed the scattering force to ensure the particle is not pushed out of the beam's focus. Thus, optical levitation traps can suffer from lack of stability and predictability of the particles position

[88]. Counter-propagating traps, first demonstrated in Ashkin's 1970 experiment, are a common alternative to levitation traps, where a particle is trapped between two counter-propagating beams focused just before they hit the particle, such that it is between the two foci. As the particle approaches either focus, it scatters more of the light from that beam and is pushed back towards the centre point. Thus, trapping is dictated by both the scattering and gradient forces in counter-propagating traps. This means they are able to hold more highly scattering particles stable, and thus particles of higher refractive index, than levitation traps [89, 90]. Figure 2.2 shows a depiction of the forces acing on particles in levitation and counter-propagating traps. A counter-propagating trap was used for all of the work presented in this thesis.

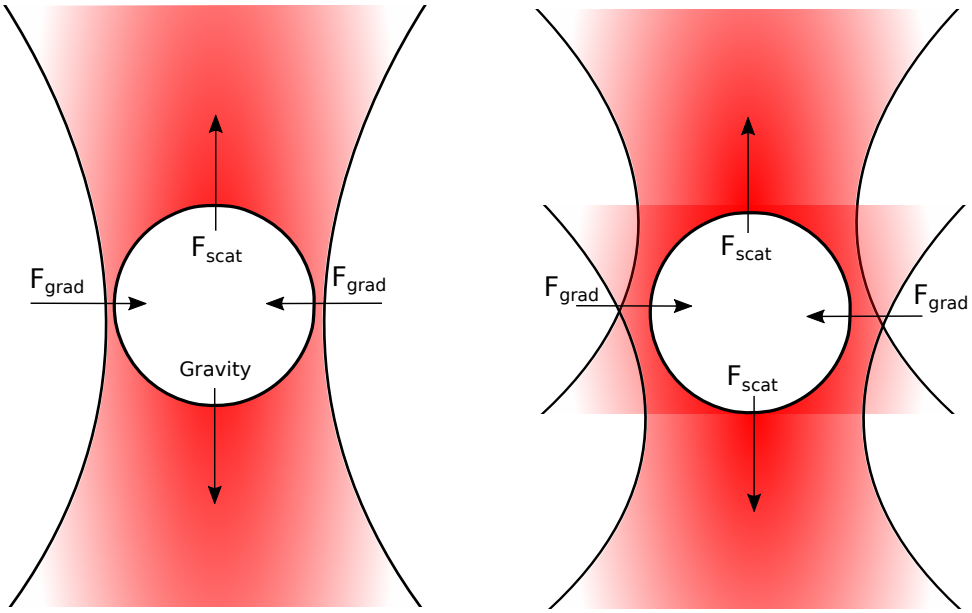

Figure 2.2: Forces acting on a particle in a Levitation trap (left) and counter-propagating trap (right) where F_{grad} is the gradient force and F_{scat} is the scattering force.

Optical trapping has many uses in biology and atomic physics, as well as atmospheric physics and chemistry. Ashkin was awarded the Nobel prize for physics in 2018 "for the optical tweezers and their application to biological systems" for his groundbreaking work carried out in 1987 where single-beam traps were used to study the tobacco mosaic virus [91]. The prize was won jointly with Gérard Mourou and Donna Strickland "for their method of generating high-intensity, ultra-short optical pulses."

Optical trapping has been used in this thesis to study atmospheric aerosol particles. The size, wavelength-dependant refractive index and morphology of various particles was determined using optical trapping and Mie spectroscopy. Optical trapping proved to be an incredibly useful method for this work as it allowed for particles to be held in place for examination without being directly touched or altered in any way. Hence, the morphology could be accurately determined without risk of it being affected by the experiment [90].

Alternative methods

Optical trapping has proven to be an incredibly useful method for understanding the chemistry and optical properties of atmospheric aerosol. However, methods other than optical trapping have also previously been used to measure the refractive index of atmospheric aerosol, each with their own unique benefits. Optical particle counters can be used to measure the size distribution and the refractive index, at a given wavelength, of atmospheric aerosol particles in situ [92]. This method of studying atmospheric aerosol benefits from not having to collect and then extract the aerosol for later experiment, as, unlike laser tweezers, the portable equipment can be used in the field.

He *et al.* have used imaging of particles suspended in oil to determine the refractive index of polystyrene beads as a function of temperature, in a similar experiment to the first paper presented in this thesis. This method allows for multiple particles to be studied at once. However using oil as a medium rather than air risks contamination of particles [93]. Cavity ring-down spectrometry is another common method of studying the refractive index of aerosol particles. Lambe *et al.* used this technique to successfully study the refractive index of brown carbon in the presence of atmospheric oxidants [94]. All three of these methods rely on calibration against another material, often polystyrene or silica beads, which as discussed in the first and second papers in this thesis are not always reliable. Optical trapping in air does not depend on calibration against any other material, thus removing a source of error. These methods can also only measure the refractive index at a single wavelength, but optical trapping and Mie spectroscopy allows for the determination of the wavelength-dependent refractive index, over a range of wavelengths [8, 95]. However, developments are constantly being made in all methods of aerosol study. For

example, in 2019 Li *et al.* developed a multi-wavelength cavity ring-down aerosol extinction spectrometer, that can measure the refractive index of particles at more than one wavelength [96].

Optical trapping experiments are often carried out in a liquid medium, as this helps to dampen any external perturbations on the particle, making it easier to hold a particle stable in the trap than it is in air [88]. Of course, trapping in a liquid medium can only be applied to solid particles, but solid and liquid aerosol particles can both be trapped in air which is essential for the study at atmospheric aerosol [90].

2.2 Optical set-up used

The experiments in this thesis where carried out using a counter-propagating optical trap comprised of a Laser Quantum 1064 nm Nd:YAG laser split using an Oz Optics beam-splitter coupling port into two single-mode fibre-optic cables to form two laser beams, pointing in opposite directions focused, using two Mitutoyo M Plan Apo x50 NA 0.42 objectives, as described by Fällman and Axner [97], into an aluminium trapping cell. The upper beam is fully steerable in the x, y, and z axes to a sub-micron accuracy using a Physik Instrumente 3-axis piezo-electric stage. The full set-up of the optical trap is shown in Figure 2.3 Aerosol was dispensed into the aluminium trapping cell, of length 7.8 cm and width 3.2 cm, via an inlet in the cell. The process of trapping involved several aerosol particles being delivered into the cell and the position of the cell was adjusted relative to the laser focus until a single bead was trapped at the point of focus.

Aerosol generation

Aerosol was released into the trapping cell either by nebulisation or atomisation, depending on the aerosol being studied.

A collision atomiser (Topas, ATM 220) was used for the generation of solid polystyrene and silica aerosol particles. Collision atomisers work by sending a stream of compressed air through an orifice to create a high velocity air jet, while also creating a low pressure zone which draws liquid containing the polystyrene or silica particles suspended in water up where the compressed air shears the jet to separate it into a spray of droplets. The atomiser used for many of the experiments in this thesis then had a

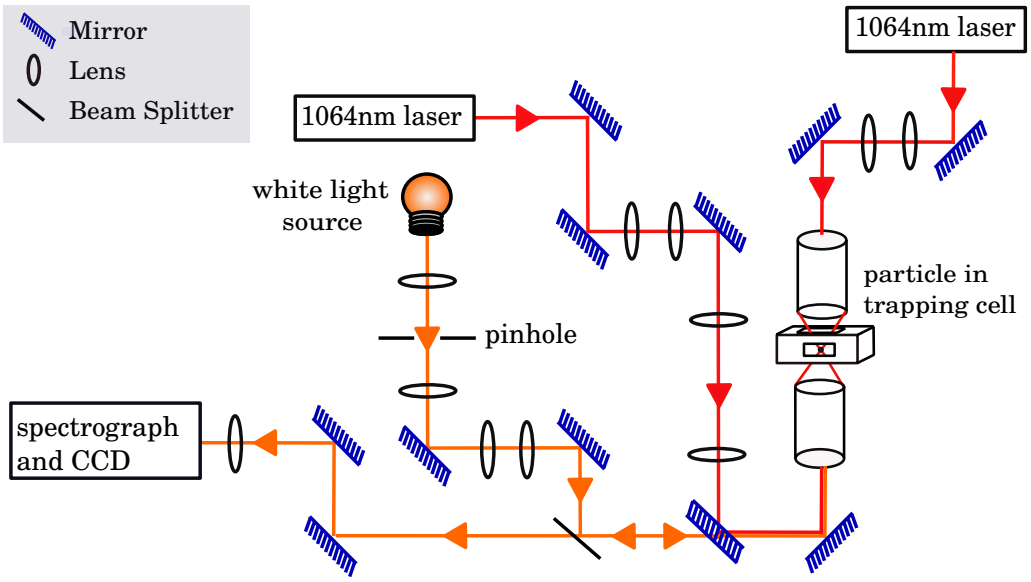

Figure 2.3: Diagram of the optical set-up used for all trapping experiments presented in this thesis.

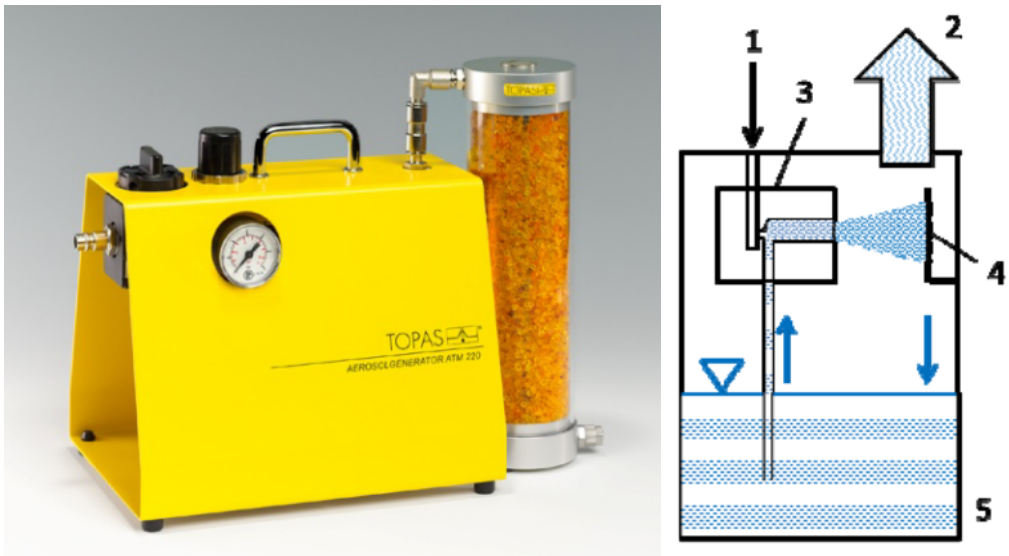

Figure 2.4: Image of the Topas ATM 220 atomiser, with diffusion dryer attached on the left and a diagram of the inside of the atomiser. The labels correspond to; 1. Dispersion gas volume flow, 2. Aerosol, 3. Two-substance nozzle, 4. Baffle, 5. Liquid reservoir. Both images ares taken from the Topas ATM 220 atomiser product specifications.

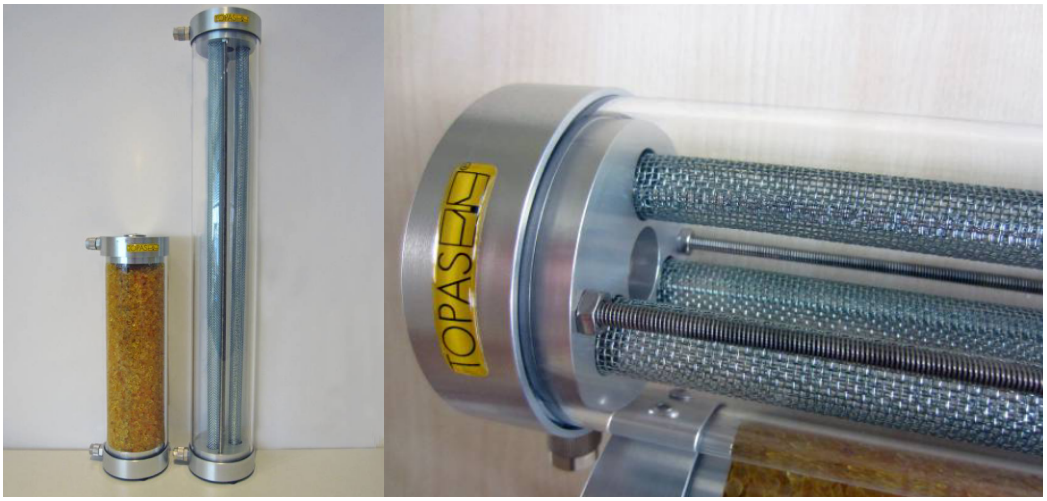

Figure 2.5: Image of the Topas diffusion dryer used to dry solid atomised particles of polystyrene and silica both filled with silica gel and empty on the left, and a closer view of the mesh pipes that the aerosol travels through inside the diffusion dryer on the right. Both images ares taken from the Topas DDU 570 diffusion dryer product specifications.

'baffle' to remove coarse spray droplets. An image of the outside and a diagram of the inside of the atomiser that was used for the work in this thesis is shown in Figure 2.4. The aerosol then travels through a diffusion dryer (Topas DDU 570) filled with a desiccant (silica gel) to remove any remaining water on the beads so they were dry when they are dispersed into the trapping cell. The aerosol travels through mesh pipes within the diffusion dryer, as shown in Figure 2.5, and does not come into contact with the desiccant.

An ultrasonic nebuliser ("Aerosonic Combineb 3019") was used to generate liquid droplets of sulfuric acid and organic aerosol for the experiments carried out in papers 3 and 4. Ultrasonic nebulisers use a piezoelectric crystal vibrating at high frequency to create sound waves which travel through the liquid creating standing waves. At the correct level of power the standing waves cause the liquid to dissipate into aerosol droplets [98]. A diagram of the nebuliser used for aerosol generation in papers 3 and 4 in this thesis is shown in Figure 2.6. The level of nebulisation can be controlled using the 'fan wheel' to control the level of air flow carrying to aerosol out of the nebuliser.

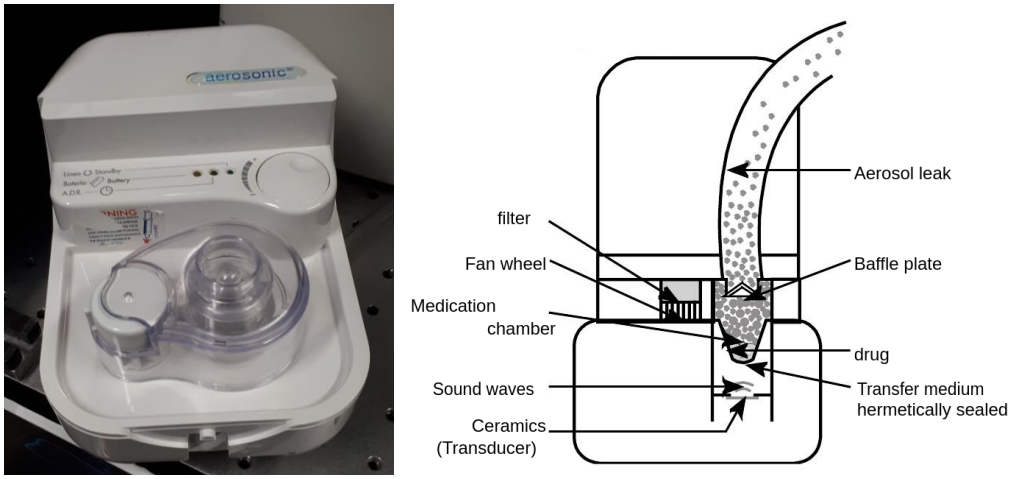

Figure 2.6: Image of the "Aerosonic Combineb 3019" nebuliser on the left. Diagram (taken from the user manual) of the nebuliser on the right. As the nebuliser is primarily sold as a device for delivering medication, the aerosol chamber is labelled here as the 'medication chamber' with 'drug' inside, where the organic aerosol in propan-1-ol is held.

2.3 Heating of aerosol particles

Temperature has a significant impact on the optical properties of atmospheric aerosol. In paper 1 in this thesis a new technique is demonstrated for measuring the wavelength and temperature dependent refractive index of airborne particles. This technique will allow for detailed studies on the optical properties of atmospheric aerosol produced at high temperatures, for example from wild fires or car exhaust fumes. The technique has been demonstrated in paper 1 by determining the size and wavelength-dependant refractive index of polystyrene beads as a function of temperature.

An aluminium trapping cell, with dimensions 7.8 cm by 3.2 cm, is used for typical optical trapping experiments. A unique trapping cell with the same dimensions was designed for this technique which allows for single particles to be heated while being held in an optical trap. A diagram of the heating cell design is shown in Figure 2 of paper 1. Insulation was a key consideration when designing this cell and spacers made from a low thermal conductivity composite, Macor, were used to insulate heat from the external components of the trapping cell. Using this design, a particle is held in the central orifice (of volume $\sim 0.5\,\mathrm{cm}^3$) of a ceramic toroidal-shaped heater (Thorlabs HT19R). The temperature is controlled externally

by varying the power supplied to the heater.

Before this technique was used to determine the wavelength and temperature dependant refractive index of polystyrene beads, a calibration was carried out to determine the temperature in the location where the particle would be held. For this, a K-type thermocouple was placed in the particles position in the central orifice of the heater, and the temperature was measured as a function of power supplied to the heater. The uncertainty in the temperature measurements is $\pm$ 1 °C due to the sensitivity of the Thorlabs HT19R heater used.

2.4 Mie scattering theory for homogeneous particles

In the mid-19th century, James Clerk Maxwell developed Maxwell's equations, a set of equations which describe how electromagnetic waves interact with matter [83]. In 1908 Gustav Mie used Maxwell's equations to formulate his theory of how light is scattered by a homogeneous sphere with a size similar to the wavelength of incident light [99].

As stated in section 1.5 atmospheric aerosol scatters visible light in the Mie regime. Therefore all of the experiments carried out in this thesis studied the Mie scattering of light by aerosol particles using Bohren and Huffman's [100] formalism of the theory of Mie scattering, which is detailed in this section.

To calculate the intensity of light scattered in the Mie regime, the "Stokes parameters" of the incident and scattered light must be determined. Stokes parameters are a set of values which describe the polarization of radiation [100]. Solar radiation can be assumed to be unpolarised, which means that Stokes parameters for both the parallel and perpendicular components of light scattering will need to be determined when calculating Mie scattering [100].

For unpolarised light, we can use Stokes parameters to calculate the intensity of scattered radiation, I_s, where,

$$I_s = S_{11} I_i, \tag{2.1}$$

where I_i is the intensity of incident radiation and S_{11} is an expression

of the amplitude of the scattered light [62],

$$S_{11} = \frac{1}{2}\left(|S_1|^2 + |S_2|^2\right), \tag{2.2}$$

where S_1 and S_2 are the parallel and perpendicular scattering amplitudes [62],

$$S_1 = \sum_n \frac{2n+1}{n(n+1)}(a_n\pi_n + b_n\tau_n), \tag{2.3}$$

and

$$S_2 = \sum_n \frac{2n+1}{n(n+1)}(a_n\tau_n + b_n\pi_n), \tag{2.4}$$

where π_n and τ_n are functions of the angle at which light is scattered, θ,

$$\pi_n(\theta) = \frac{P_n^{'}(\theta)}{\sin(\theta)}, \tag{2.5}$$

$$\tau_n(\theta) = \frac{\mathrm{d}P_n^{'}(\theta)}{\mathrm{d}\theta}, \tag{2.6}$$

and a_n and b_n are the partial wave amplitudes or scattering amplitude coefficients,

$$a_n(x,m) = \frac{m\psi_n(mx)\psi_n^{'}(x) - \psi_n(x)\psi_n^{'}(mx)}{m\psi_n(mx)\xi_n^{'}(x) - \psi_n(x)\xi_n^{'}(mx)} \tag{2.7}$$

and

$$b_n(x,m) = \frac{\psi_n(mx)\psi_n^{'}(x) - m\psi_n(x)\psi_n^{'}(mx)}{\psi_n(mx)\xi_n^{'}(x) - m\psi_n(x)\xi_n^{'}(mx)} \tag{2.8}$$

where m is the relative refractive index (refractive index of particle divided by refractive index of medium) of the homogeneous sphere, x is the size parameter and ψ_n and ξ_n are Riccati-Bessel functions,

$$\psi_n(x) = xj_n(x) \tag{2.9}$$

and

$$\xi_n(x) = xh_n(x), \tag{2.10}$$

where j_n and h_n are spherical Bessel, and spherical Hankel functions of the first kind of order n [101, 100].

Therefore, for the calculation of the intensity of light scattered by a Mie particle the required parameters are the radius of the particle and the wavelength of incident light for calculation of the size parameter, and the relative refractive index for calculation of the scattering amplitude coefficients.

Mie scattering theory for core-shell particles

The scattering of light by spherically symmetrical core-shell particles, first derived by Aden and Kerker in 1951 [102] is similar to that of homogeneous spheres, described in Section 2.4. The only difference is the scattering amplitude coefficients a_n and b_n, as they depend on the radial variation of the relative permittivity, ϵ, and relative permeability, μ, of the particle [100, 102]. For non-magnetic materials μ can be approximated to 1, and at optical frequencies the permittivity is the square of the refractive index. Therefore the scattering amplitude coefficients can be determined from the size parameters and the refractive indices of the core and shell only [100]. For a coated sphere the scattering amplitude coefficients become;

$$a_n = \frac{\psi_n(y)[\psi_n^{'}(m_2y) - A_n\chi_n^{'}(m_2y)] - m_2\psi_n^{'}(y)[\psi_n(m_2y) - A_n\chi_n(m_2y)]}{\xi_n(y)[\psi_n^{'}(m_2y) - A_n\chi_n^{'}(m_2y)] - m_2\xi_n^{'}(y)[\psi_n(m_2y) - A_n\chi_n(m_2y)]} \tag{2.11}$$

and

$$b_n = \frac{m_2\psi_n(y)[\psi_n^{'}(m_2y) - B_n\chi_n^{'}(m_2y)] - \psi_n^{'}(y)[\psi_n(m_2y) - B_n\chi_n(m_2y)]}{m_2\xi_n(y)[\psi_n^{'}(m_2y) - B_n\chi_n^{'}(m_2y)] - \xi_n^{'}(y)[\psi_n(m_2y) - B_n\chi_n(m_2y)]} \tag{2.12}$$

where

$$A_n = \frac{m_2\psi_n(m_2x)\psi_n^{'}(m_1x) - m_1\psi_n^{'}(m_2x)\psi_n(m_1x)}{m_2\chi_n(m_2x)\psi_n^{'}(m_1x) - m_1\chi_n^{'}(m_2x)\psi_n(m_1x)} \tag{2.13}$$

and

$$B_n = \frac{m_2\psi_n(m_1x)\psi_n^{'}(m_2x) - m_1\psi_n(m_2x)\psi_n^{'}(m_1x)}{m_2\chi_n^{'}(m_2x)\psi_n(m_1x) - m_1\psi_n^{'}(m_1x)\chi_n(m_2x)} \tag{2.14}$$

where m_1 and m_2 are the refractive indices, and x and y are the size parameters of the core and shell respectively.

2.5 Collection of Mie spectra

The intensity of scattered light as a function of wavelength is known as a 'Mie spectrum'. Figure 2.7 shows an example of the Mie spectra collected

in the work carried out in this thesis. The trapped particles were illuminated with white LED light (Comar 0.1 LD 555, 6 V) and the elastically back-scattered light was collected using a Princeton Instruments spectrograph (Acton SP-2500i) and charge-coupled device detector.

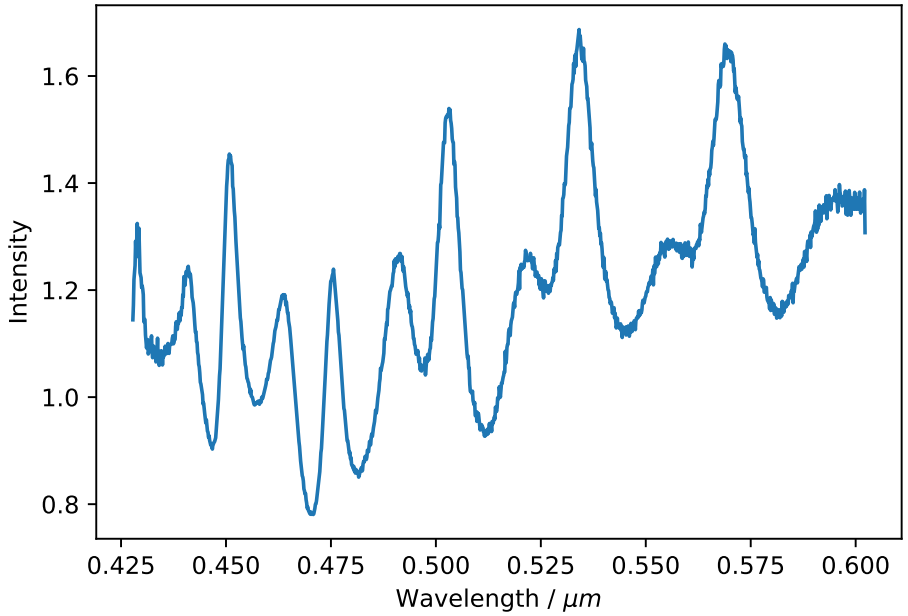

Figure 2.7: Example experimental Mie spectrum, captured of a Whitehouse silica bead for paper 2 in this thesis

Spectrograph

A schematic of the inside of the spectrograph, redrawn based on a diagram from the user manual, is shown in Figure 2.8. The back-scattered light enters the spectrograph via the entrance slit and hits a collimating mirror which reflects the light as a collimated beam (where all light rays in the beam are parallel). This collimated beam of light is then reflected off a diffraction grating which disperses the white light into its constituent wavelengths. A diagram of light reflecting off a diffraction grating is shown in Figure 2.9. Dispersion occurs because each groove on the grating acts as a point source from which light is reflected. Interference between the reflected light waves will create areas of maximum intensity, caused by constructive interference. As the angular locations of maximum intensity are dependent on the wavelength of incident light, the diffracted light will

be reflected at different angles depending on the wavelength, dispersing the white light into its constituent wavelengths.

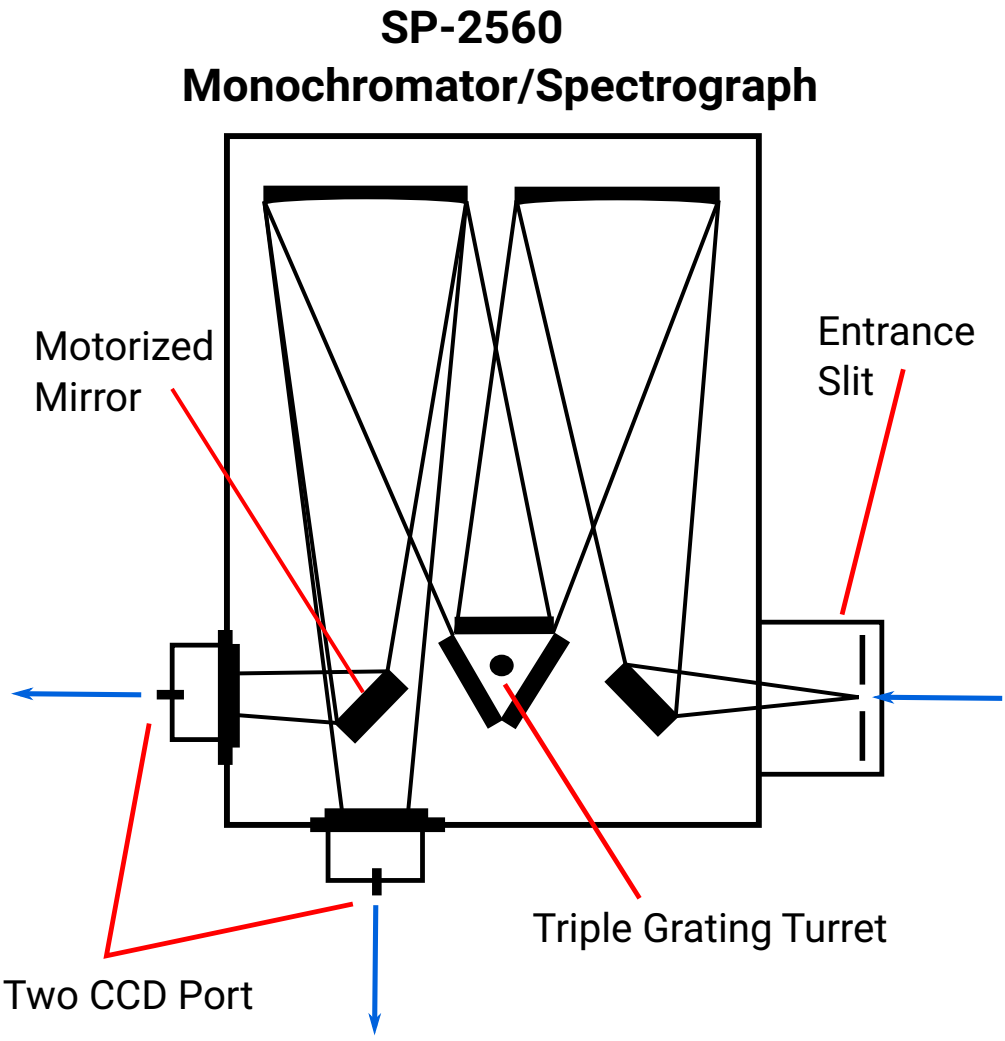

Figure 2.8: Diagram of the inside of the spectrograph (Acton SP-2500i) used, redrawn based on a diagram from the user manual.

The relationship determining the angular locations of the principal intensity maxima when light of a given wavelength is diffracted from a grating of groove spacing d is described by the grating equation,

$$m\lambda = d(sin\alpha + sin\beta), \tag{2.15}$$

where m is an integer value, known as the diffraction order, and α and β are the angles of incidence and diffraction, as demonstrated in Figure 2.9.

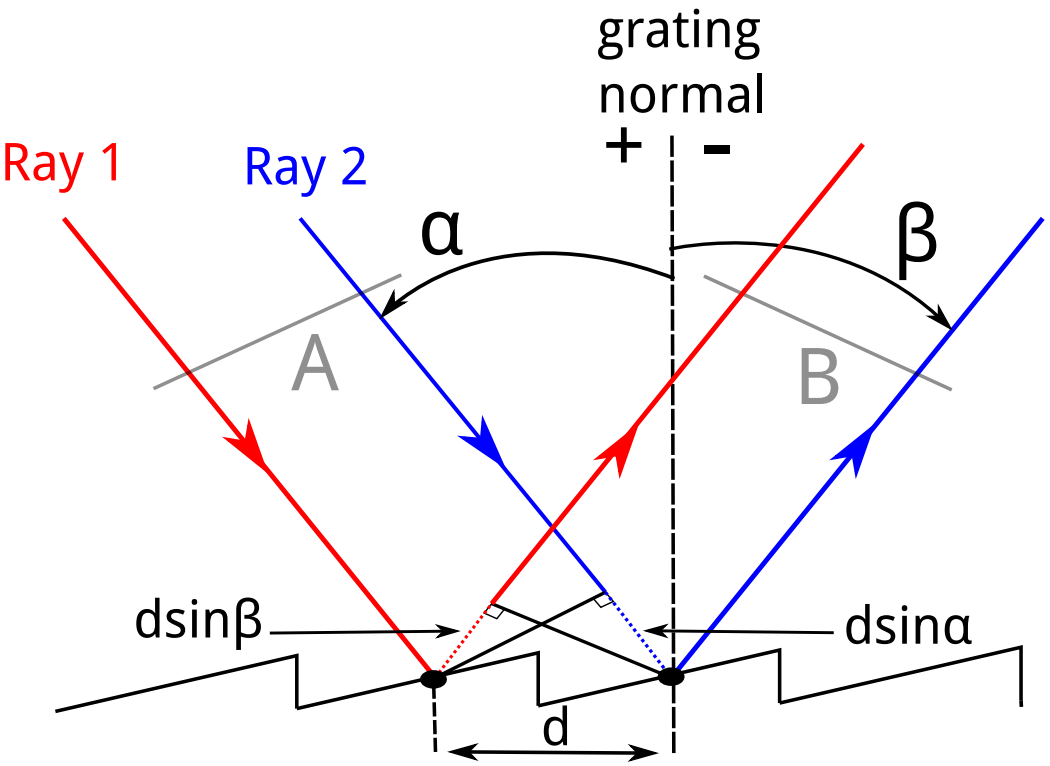

Figure 2.9: Two in phase light rays from incident wavefront A are diffracted off the grating. The diffracted rays in wavefront B will be in phase when the difference in the path lengths $d \sin \alpha$ and $d \sin \beta$ is an integral number of the wavelength of incident light, according to the grating equation. Recreated from the'Diffraction grating handbook' [103]

When setting up the spectrograph for experiment, the wavelength range, wavelength resolution and signal to noise ratio must all be considered. These factors can be altered by varying the groove spacing on the diffraction grating, and the exit slit width, where the dispersed light is sent from the spectrometer to the CCD. The spectrograph used in the work in this thesis has three optional diffraction gratings (300, 600, or 1200 grooves/mm). As the number of pixels in the CCD is constant, if a grating with a higher grooves/mm is used, the wavelength range covered will have to be decreased. Therefore, a balance has to be struck between wavelength resolution and range, when choosing a grating [103].

It is possible to perform a 'step and glue' operation, where multiple spectra can be collected over different wavelength ranges and combined to generate a Mie spectrum with a longer wavelength range. However, it takes a certain length of time to collect spectra (in this thesis spectra were

typically collected over 3 seconds). Therefore taking multiple spectra for a step and glue operation will take over double the length of time, as the spectrograph needs time to move position as well as the length of time required to collect the spectra.

For the work carried out in this thesis it was generally not practical to use the step and glue function as many of the particle systems studied were subject to change over time. It was therefore essential to capture spectra in the quickest time possible to accurately record changes in the Mie spectra, and hence the optical properties of the particles. It was not necessary to carry out a step and glue function on the work in this thesis as adequate wavelength range and resolution were able to be obtained using the 300 grooves/mm grating. For systems with either important spectral behaviour over a wider wavelength range, or with very broad Mie resonances, the increase in wavelength range or resolution provided by the step and glue function could be vital for obtaining spectra that can be effectively analysed.

Charge-coupled device detector

The wavelength dispersed light is then analysed by a charge-coupled device (CCD) detector. CCDs are sensitive photon detectors, comprised of thousands of pixels. Each pixel has a thin layer of silicon and a capacitor. When a photon with sufficient energy hits the silicon layer it can cause an electron to be released from the outer shell of a silicon atom. The energy of the photon is determined by the photoelectric effect,

$$E = \frac{hc}{\lambda}. \tag{2.16}$$

where E is the energy of the photon, h is Planck's constant, c is the speed of light and λ is the wavelength of the photon.

The attached capacitor collects the electrons that are released from the silicon layer. The 'quantum efficiency' is the percentage of photons hitting the CCD that cause electrons to be detected. The quantum efficiency of the CCD used in this project is $92 - 95\%$.

Mie resonances

When light is scattered by an aerosol particle, some rays of light will experience total internal reflection and become temporarily trapped within the cavity-like structure of the particle. Standing waves will then form at resonant frequencies, where the so-called 'natural frequencies' of the particle are matched by certain wavelengths of light, causing an increase in the intensity of scattered light at certain wavelengths [100].

These areas of increased intensity are known as 'morphology dependent resonances' and are vector spherical harmonics, or 'electromagnetic normal modes'. Transverse magnetic (TM) modes have no radial magnetic component and are weighted by the scattering coefficient a_n, and transverse electric (TE) modes, have no radial electric component, and are weighted by the scattering coefficient b_n.

The wavelengths of these resonances depend on the refractive index and the size of the particle, and are visible in the Mie spectrum as peaks in intensity, as demonstrated in Figure 2.7. The resonances are therefore the defining characteristic of the Mie spectrum and can be used to determine the optical properties of the particle.

2.6 Determining optical properties of aerosol from Mie spectra

There are multiple methods of determining the optical properties of aerosol particle from their Mie spectrum. It is possible to determine the size and wavelength-dependent refractive index of a particle using the wavelength positions of the Mie resonances only [104, 68, 105, 106] or by using the whole profile and shape of the Mie spectrum in combination with peak positions [107, 108].

Lew *et al.* [105] published a comparison of the various fitting methods available, and reported that analysis of the full spectrum is a more complicated process which will therefore be more computationally demanding than only using the Mie resonance positions. Analysing the whole spectrum would require consideration of additional parameters that are not required when analysing the spectrum based purely on the Mie resonance positions. The intensity profile of the broadband light source [108], and

the acceptance angle and positioning of the objective used to collect the scattered light are necessary to correctly reproduce measured spectra, introducing potential additional sources of error.

There are circumstances where analysis of the whole spectrum would be a very useful and perhaps necessary technique. For example, when studying spectra of particles with no sharp peaks, due to high absorption or a low size parameter. However, for all of the work carried out in this thesis, Mie spectra with many sharp peaks were produced. Therefore, it was decided that fitting should be carried out using the Mie resonance positions only. To carry out the fitting process of determining the optical properties of the aerosol from its Mie spectrum, a program was written in Python. This program was written to improve upon the speed and efficiency, and decrease the amount of manual effort required than the previous method used, which involved manual iteration of the parameters A, B, C and radius, to determine which parameters produced a spectrum for which the refractive index as a function of wavelength best fit to the Cauchy equation using a Levenberg-Marquardt algorithm [8]. The operation of the program is split into two sections, the 'grid-scan' step and the 'Cauchy fitting' step, described in the following sections.

Peak finding

The first step in fitting an experimental Mie spectrum is to find the wavelength positions of the peaks. For this program the function `find_peaks` from the Python SciPy [109] package signal was used. The function works by searching through an array of intensity values provided and, using a simple comparison of neighbouring values, returns all points in the array where the two intensity values on either side have a smaller value. The required difference in potential peak position to neighboring values, for a peak to be detected, can be set using the prominence input parameter. Other input parameters such as the necessary distance between two peaks detected and necessary height of peaks detected can also be used to filter out any noise in the signal wrongfully detected as a peak. Once the peaks have been detected using `find_peaks`, to ensure the centre of the peak is used for fitting rather than the point of highest amplitude which may not be in the centre owing to the precision of the spectrometer, a Gaussian curve is fitted to each peak and the centre of the Gaussian curve is then taken as the wavelength peak position.

Adaptive baseline

The LED light source used for light scattering experiments will introduce some variation in the intensity of the spectrum, due to its own intensity profile across the wavelength range. The spectrum of the Comar 555 white LED light source used is shown in Figure 2.10. Other factors such as sources of light within the lab can also introduce small amounts of noise into the spectrum. This can cause problems when trying to find the correct peak positions for fitting. To compensate for this, we use an "adaptive baseline" algorithm to remove some of the background, flattening the spectrum and making it easier to locate the peaks.

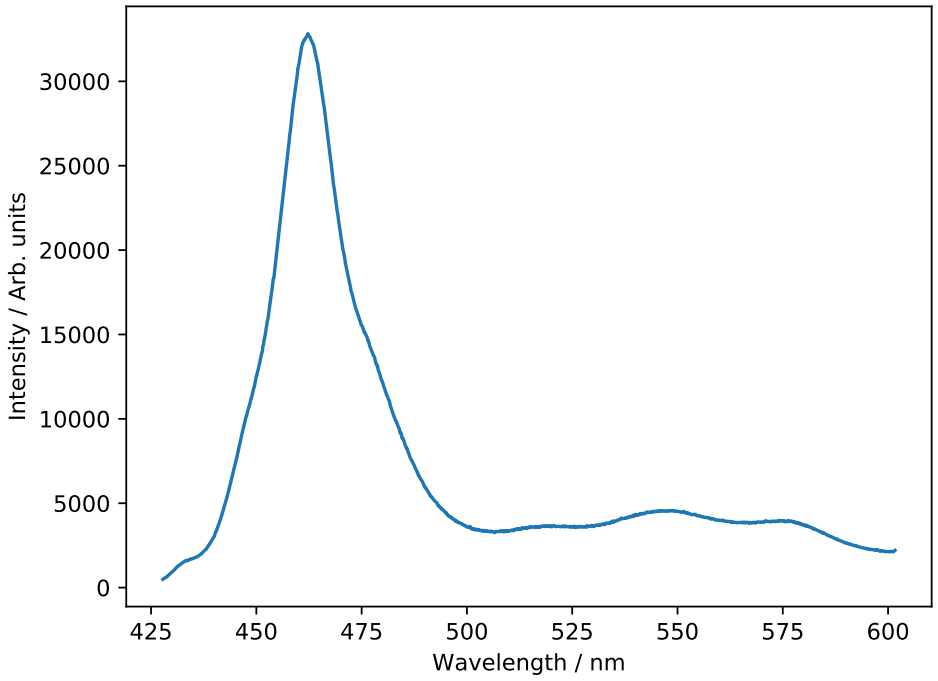

Figure 2.10: Spectrum of the Comar 555 white LED light source used in all Mie scattering experiments in this thesis.

The simple algorithm used to apply an adaptive baseline was suggested by Friedrich Menges, the author of 'Spectragryph' ([110]) spectrum analysis software. This algorithm was implemented in Python alongside the rest of the fitting procedure for this project. The baseline is calculated by first applying a 0^{th} percentile filter over a window of values surrounding each point on the spectrum, to find the lowest value in that window.

The effect of applying the 0^{th} percentile filter is demonstrated by the orange line in the top panel of Figure 2.11. The size of the window considered at each point is determined by the "coarseness" parameter. A moving average is then calculated for the 0^{th} percentile spectrum using the same size window, to smooth the baseline, as demonstrated by the green line in the top panel of Figure 2.11. Finally, the experimental spectrum is then divided by the calculated baseline. The bottom panel in Figure 2.11 shows an example experimental spectrum before and after an adaptive baseline has been applied.

Using the same method and coarseness, a baseline is applied to all the of theoretical spectra calculated in the "grid-scan" step to ensure a consistent comparison.

Grid-scan

The grid-scan step of the program, works by comparing the experimental Mie spectrum to a large range of theoretical spectra generated for a given range of refractive index and radius values. As the refractive index of aerosol particles is dependent on wavelength, following Equation 1.7, there are three parameters; the constants A, B and C, that are needed to determine the wavelength dependent refractive index of the particle. The refractive index constants along with the radius of the particle create a four-dimensional 'grid' of potential solutions. For each set of potential solutions a theoretical spectrum is generated using Bohren and Huffman's [100] formalism of Mie theory for homogeneous spheres. Each of the theoretical spectra is then compared with the experimental spectrum. An average peak difference is calculated for each theoretical spectrum by averaging the difference in wavelength position between each of the theory and experimental peaks. It is important that the theoretical spectra are generated with at least the same, if not greater, precision in wavelength as the experimental spectra, which for all the work in this thesis was 0.13 nm, for optimal comparison.

The range and precision for the values A, B, C and radius that make up the 4-dimensional grid need to be decided on a case-by-case basis. Considerations such as available computing power, previous knowledge of the physical properties of the particle, and required precision of result, should all be considered when setting these parameters. As an example, for a polystyrene bead the refractive index is approximately known from liter-

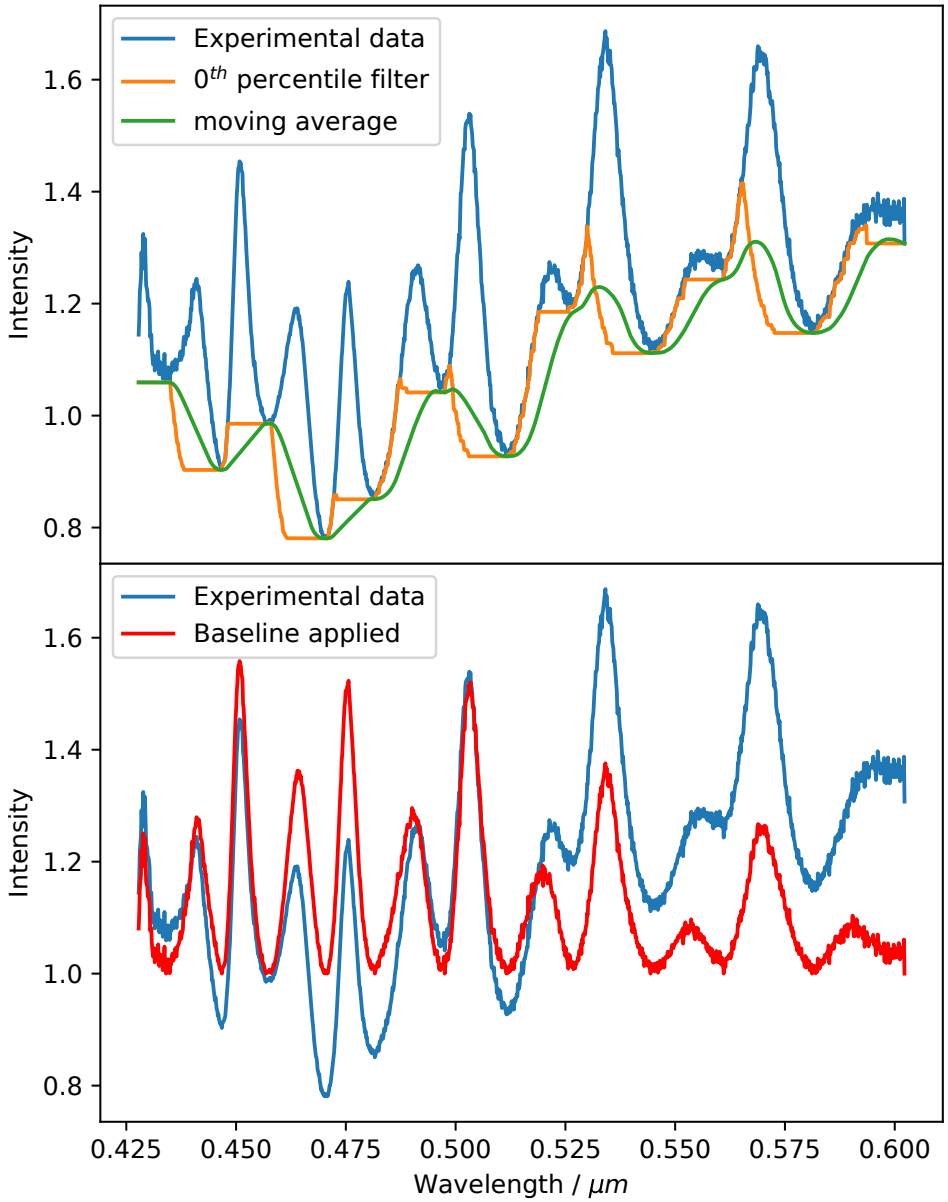

Figure 2.11: Effect of both steps in the baselining process are demonstrated in the top panel. Experimental Mie spectrum of example Whitehouse silica bead with and without adaptive baseline applied shown in the bottom panel.

ature as $\sim$ 1.6 [111], therefore as A has the biggest impact on the refractive index it can be assumed that A will be within the range $1.55 - 1.65$. As B and C have a much smaller impact on the overall refractive index it is usually best to allow the full range of physically possible values of B ($0-0.02\,\mu m^2$) and C ($0 - 1 \times 10^{-4}$ μm^4) to be searched. In the case of

polystyrene beads, the radius is provided by the manufacturer. If the value quoted is 1 µm then a range of $0.98 - 1.02$ will typically be sufficient to find the correct value of radius. The precision of each of these parameters can be decided based on the needs of the user. Typical precision used in this thesis were A; 0.001, B: 0.001 µm^2, C: 1×10^{-5} µm^4 and radius: 0.001 µm. The parameters B and C can be determined to a lower precision than A and radius as they have a much smaller impact on the spectrum, and they will both be determined to a higher precision in the following "Cauchy fitting" step.

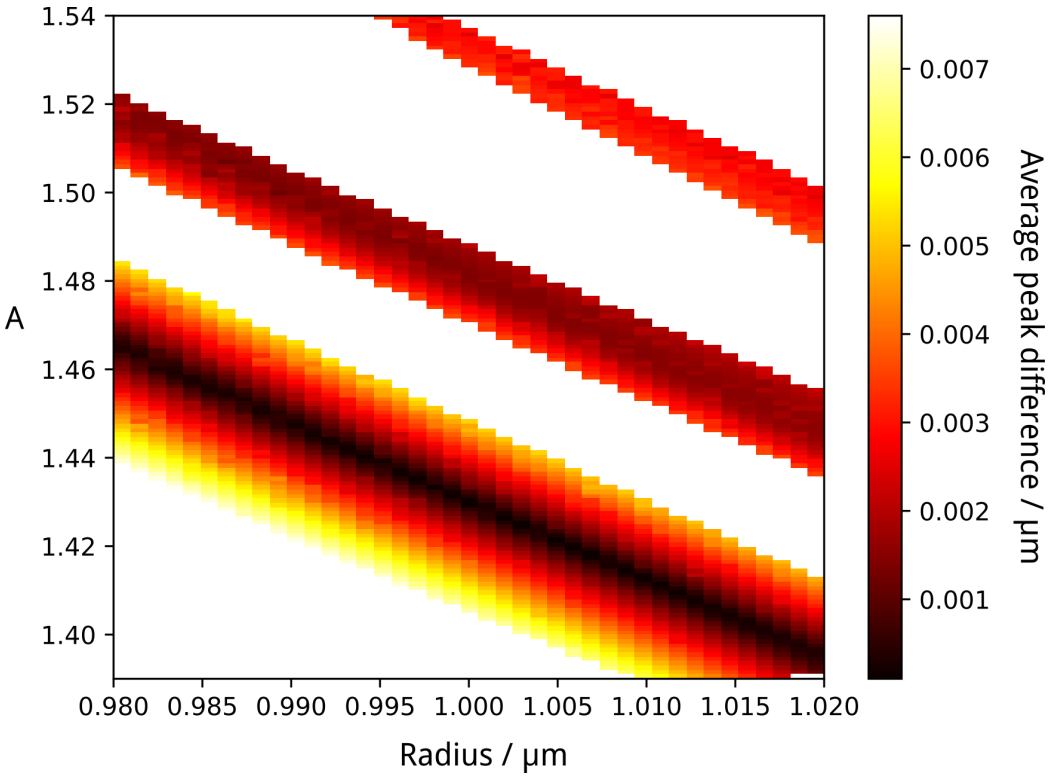

Figure 2.12: Two-dimensional cross section of the four-dimensional parameter space searched by the grid-scan fitting method. Darker colour denotes a lower 'average peak difference' and thus a better fit. There are several potential 'good fits'. However, only one will be the global minimum.

Figure 2.12 shows a two-dimensional slice through the four-dimensional grid of results, where A and radius were varied and B and C were static. As shown there are multiple areas of local minima which could be mistaken for correct solutions. This program allows for the identification of local minima and therefore allows the user to ensure the global minimum is found as the correct solution. As shown in Figure 2.12 there are many po-

tentially correct solutions surrounding the global minimum. It was found that for many cases there were a range of theoretical spectra with equally good (within the precision of the spectrograph - 0.13 nm) results, based purely on the average peak difference. In order to further differentiate between these minima to improve the precision of the results the "Cauchy fitting" step, described in the following section, was added. The parameters of the theoretical spectrum with the lowest average peak difference, are taken to be an approximate result for the wavelength-dependent refractive index and radius of the particle. The grid-scan method has proven to be a very efficient method of determining the approximate values of refractive index and radius. Figure 2.13 shows an example of an experimental spectrum with theoretical spectrum found as its closest match. The results from this step will be the basis of the Cauchy fitting step, used to increase accuracy and precision of the result.

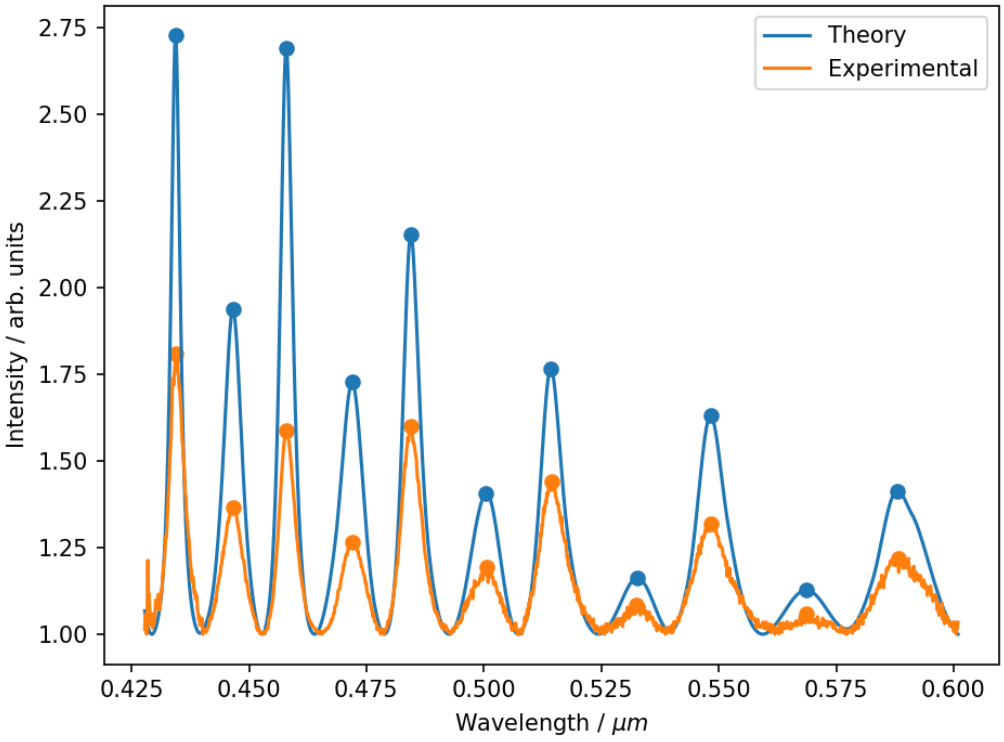

Figure 2.13: Experimental Mie spectrum of an example Corpuscular silica bead, compared with the theoretical 'best fit' spectrum determined from the grid-scan fitting step. The dots on the peaks denote the peak positions used for the calculation.

Cauchy Fitting

The Cauchy fitting step of the program works on the assumption that the refractive index of the particle as a function of wavelength must fit to the Cauchy equation. Starting with the radius result from the grid-scan step, the refractive index is determined at each peak in the experimental spectrum and plotted as a function of wavelength, as shown in Figure 2.15. The refractive index at each peak is determined using the grid-scan method on each peak. Figure 2.14 demonstrates how, at each peak, spectra were generated for multiple refractive index values, and compared to the experimental peak position to find the refractive index at that wavelength.

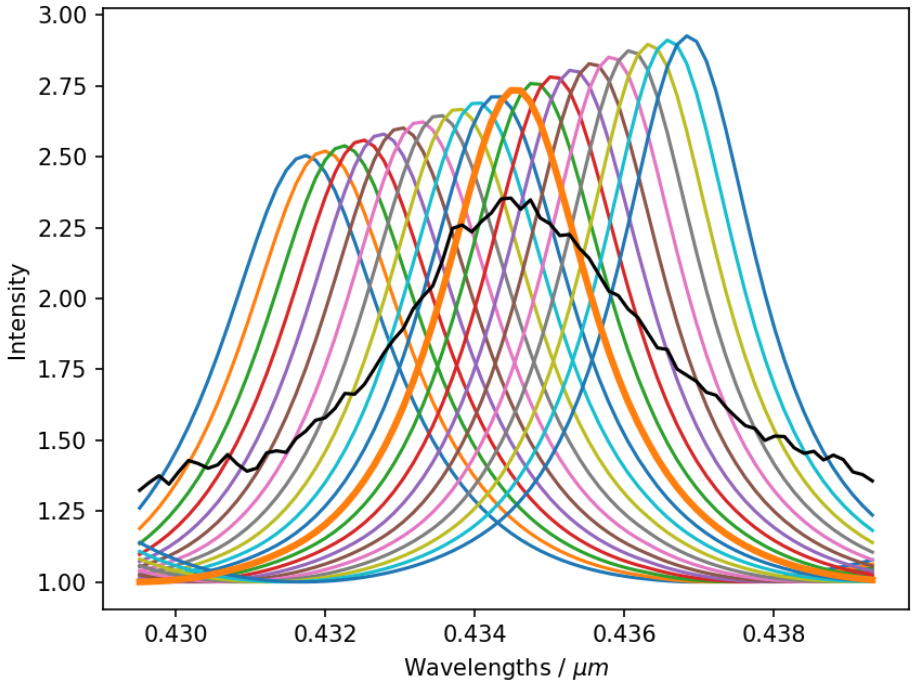

Figure 2.14: Example of the method used to find the refractive index at a single peak. The black line is the experimental spectra, and the others are all of the theoretical generated spectra of different refractive indices, which are compared with the experimental. The thicker orange line is the theoretical spectrum found to be the best fit in this case.

A Cauchy curve is then fitted to the data using a Levenberg-Marquardt algorithm. This is then repeated for a range of radii values ($\sim \pm 10$ nm of the radius result from the grid-scan step), as shown in Figure 2.15. Each

of the curves plotted in Figure 2.15 corresponds to a different value of radius. Although at first glance it may appear that there is a good fit to the Cauchy equation at all radii, the Levenberg-Marquardt algorithm returns a residual for the Cauchy fit at each radius, which is sensitive enough to always determine a clear best fit. The radius and resulting A, B and C from the Cauchy fit with the lowest residual value are taken as the final result of refractive index and radius of the aerosol particle.

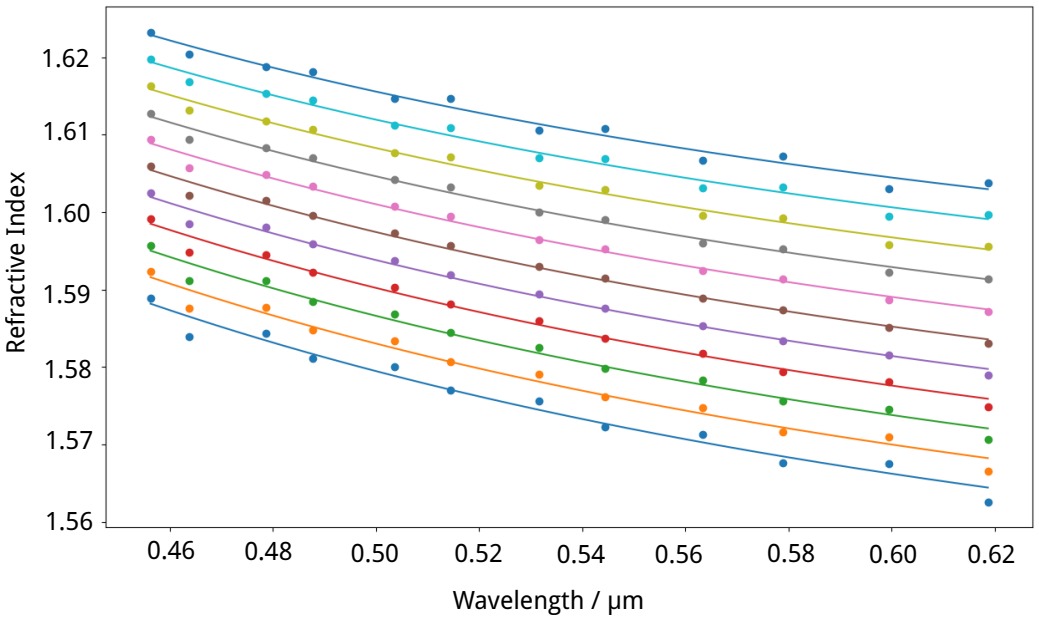

Figure 2.15: Cauchy curves fitted to refractive indices determined at each peak in a given spectrum as a function of wavelength. The radius was set at a different value for the calculation of each of the curves. The curve with the lowest residual as determined by the Levenberg-Marquardt algorithm is the best fit.

Testing and Errors

The program was tested by generating spectra of known refractive index and radius in Philips Laven's MiePlot [112] and fitting them using this program to ensure the correct solution was found. For every test case for a radius between $0.5-3\,\mu m$, and refractive index range $1.3-1.7$, the exact correct parameters were determined as the best fit. Although exact matches were found for generated 'perfect' spectra, in practise, other factors such as noise in the experimental data, and the precision of the spectrograph, will increase the uncertainty in results.

Adaption of fitting program for core-shell particles

In this project, experiments were carried out on both homogeneous and core-shell particles. An altered version of the fitting program written for homogeneous spheres was used for analysis on the core-shell particles. The same grid-scan method was used, but the generation of the theoretical spectra was changed from homogeneous to core-sphere theory. The program 'pymiecoated' [113] written by J. Leinonen, based on Aden and Kerker's [102] theory of Mie scattering from core-shell particles was used for the generation of the theory spectra.

Core-shell particles have eight parameters: A, B and C of the refractive index of both the core and shell, the radius of the core, and the thickness of the shell. The optimal way to determine all eight parameters is to obtain spectra of the core and shell material separately, and to first use the homogeneous fitting program to determine the parameters of the core, and the wavelength-dependent refractive index of the shell. If the refractive index and radius of the core and the refractive index of the shell material are known, the only parameter to determine with the core-shell program is the thickness of the shell. This is optimal as it decreases the number to theoretical spectra to be generated, and therefore the computational time and power required. In the case where the refractive index of the shell is known, such as in paper 4 in this thesis where sulfuric acid was deposited onto silica particles, the calculation of the shell thickness can be carried out to a precision of 0.001 µm, with consideration of shell thickness's over a 1 µm range within a matter of minutes on an 18 core PC, meaning 1000 theoretical core-shell Mie spectra can be generated and compared with an experimental spectrum in under 20 minutes (of course this is dependent on computing power available).

However it may not be possible, as indeed was the case for one of the experiments in this project, to get a spectrum of the organic shell material on its own. Therefore the program had to be used to determine the refractive index and thickness of the shell simultaneously. Due to the optimisation and parallelisation of the code this was achievable within a reasonable time. As the time taken for calculation can vary hugely depending on range and precision of parameters and computer power it is impossible to state a time for calculation. However the following example gives an approximate idea of the time required. With the parameters set to the following ranges and precisions; A: $1.4 - 1.6$ at a precision of 0.001, B: $0 - 0.02\,\mu m^2$ at a precision of 0.001, C: $0 - 1 \times 10^{-4}$ μm^4 at a precision of

1×10^{-5} µm^4, and shell thickness: $0 - 0.05$ at a precision of 0.001 µm, this calculation would take approximately $6-12$ h to complete.

The Cauchy fitting step cannot be carried out on the core-shell spectra as a change in the refractive index of the shell on a core-shell particle will have a significantly smaller effect on the spectrum than a change in the refractive index of a homogeneous particle. Therefore it is not possible to determine the refractive index to the required accuracy that is needed for this step.

Testing and Errors

Comparison with spectra generated in MiePlot [112] was also used for the testing of the core-shell program. However, unlike the homogeneous program which was able to find perfect matches for a large range of sizes and refractive indices, the results of testing were more complex. It was found that the error in the determined refractive index was much higher for thinner shells. Spectra with a core of radius 1 µm and refractive index 1.45, and a shell of refractive index 1.52 and shells of 1 nm, 10 nm, 20 nm, and 50 nm were generated using Mieplot. Figure 2.16 demonstrates that the refractive index of the shell becomes easier to accurately determine as the shell becomes thicker. It is also shown in the bottom panel of 2.16 that the shell thickness can be determined with equal accuracy for any shell thickness, from 1 nm.

A second test was carried out to check if spectra of core-shell particles with thin films were equally insensitive to refractive index at a higher value of refractive index. A plot of average peak difference against refractive index is shown in Figure 2.17 for spectra of core-shell particles with a 1 nm shell and refractive index of 1.52 and 1.6. It was found that the same behaviour is exhibited for both values of refractive index.

2.7 Methodology summary

Optical trapping and Mie spectroscopy have been used to study the optical properties of various aerosol particles. Optical trapping provides a non-invasive method of studying aerosol, which was leveraged in this thesis by studying the properties of heated polystyrene without risk of contamination of the particles, and by studying the morphology of two-phase par-

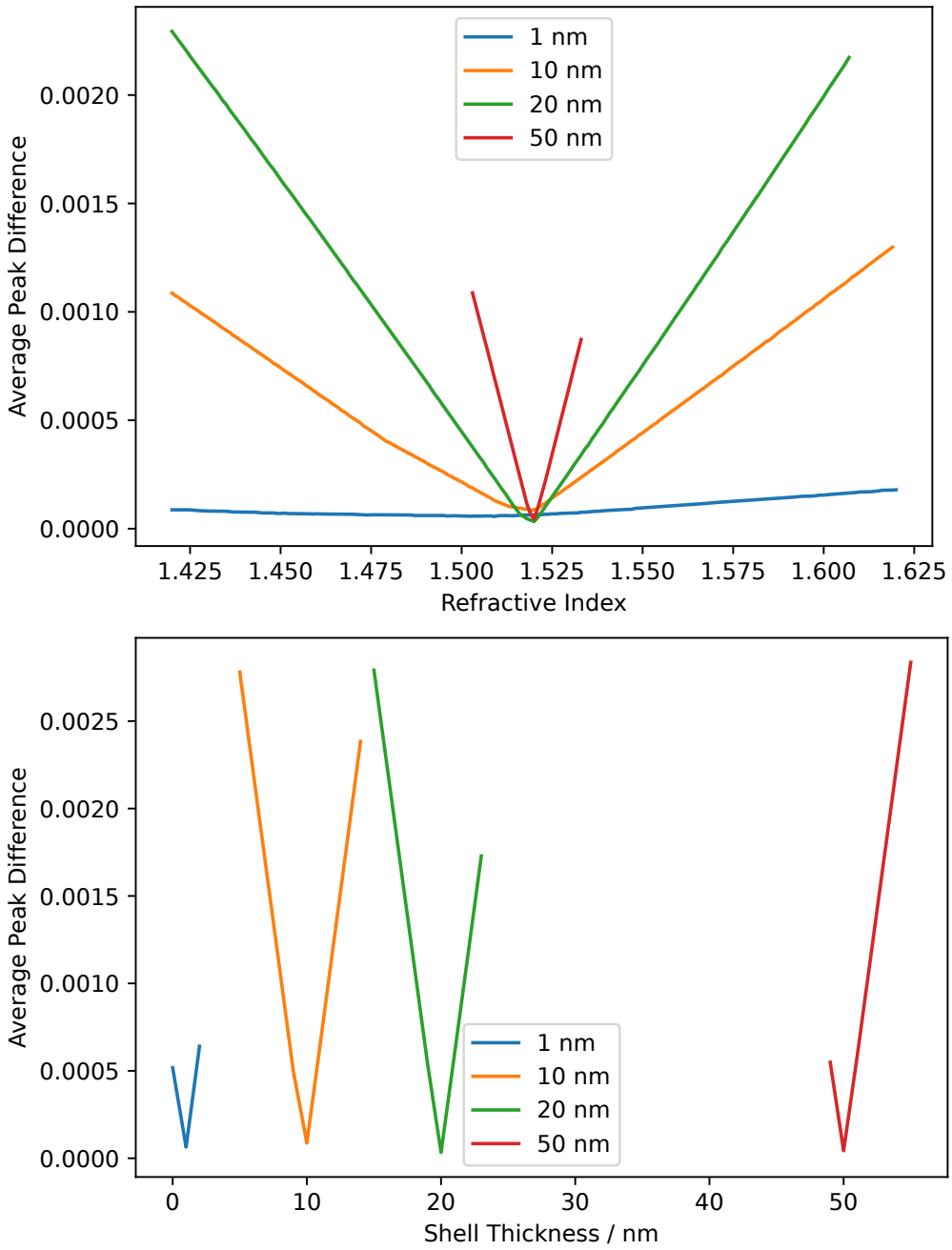

Figure 2.16: The top panel shows how the refractive index of a shell material is harder to determine for a core-shell particle with a thinner shell. For a 1 nm shell the refractive index cannot be definitively determined within a refractive index of 0.2. However the refractive index of a shell $>$20 nm can be determined. The bottom panel demonstrates that the shell thickness can be determined to an equal precision for a shell of 1$-$50 nm and a shell of 50 nm.

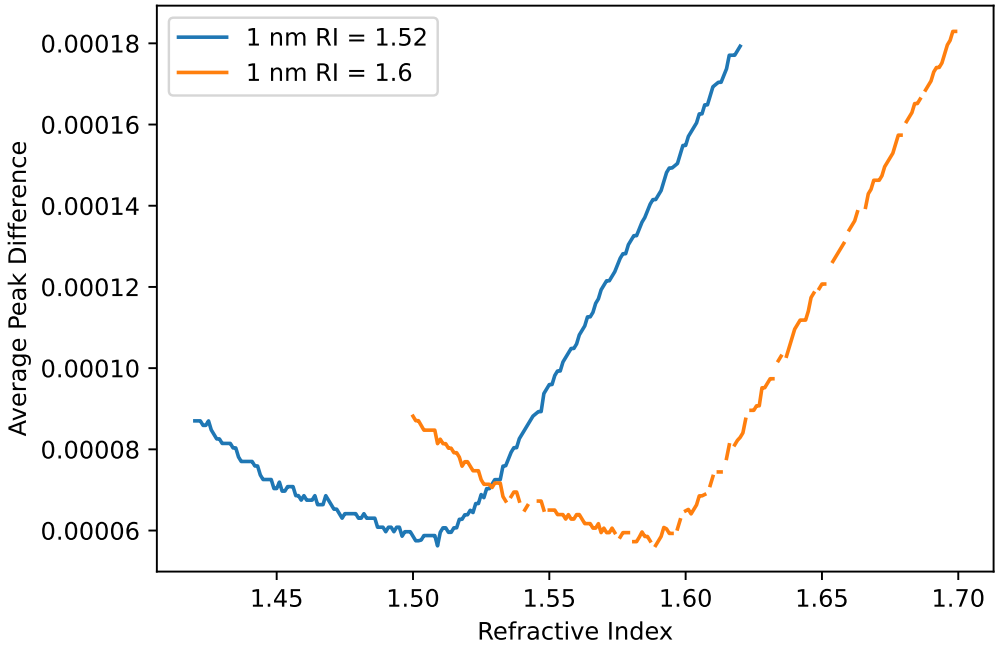

Figure 2.17: Plot of average peak difference against refractive index for core-shell particles with a 1 nm shell of refractive indices of 1.52 and 1.6.

ticles without risk of the experiment disturbing the particles morphology. Mie spectroscopy collects the back-scattered light from aerosol particles, and provides a spectrum of the intensity as a function of wavelength. This allows for the wavelength-dependent refractive index to be determined for all aerosol studied.

To determine the optical properties of aerosol from their Mie spectrum, computational analysis is required. For this thesis, a new program has been written to provide a method of determining the size and wavelength-dependent refractive index of both homogeneous and core-shell aerosol particles in a much faster way the previous method used, requiring significantly less manual effort. This increase in speed and efficiency has allowed for analysis of core-shell Mie spectra which was previously unfeasible. The thickness and wavelength-dependent refractive index of the shell on core-shell particles have been determined simultaneously for many core-shell spectra, where in previous methods the refractive index would have had to be already known, and only the thickness could be determined.

Chapter 3

Using Mie scattering to measure the wavelength dependant refractive index of polystyrene beads with changing temperature

Megan R. McGrory, Martin D. King and Andrew D. Ward

Publication status: Published in the Journal of Physical Chemistry (November 2020)

I declare I have made the following contributions to the piece of co-authored work:

- Conducted the experiments, and analysed all data collected
- Contributed to the conclusions drawn from the experiments conducted
- Wrote the first draft and, upon feedback from co-authors, completed all revisions of the paper

THE JOURNAL OF PHYSICAL CHEMISTRY A

pubs.acs.org/JPCA Article

Using Mie Scattering to Determine the Wavelength-Dependent Refractive Index of Polystyrene Beads with Changing Temperature

Megan R. McGrory, Martin D. King, and Andrew D. Ward*

Cite This: J. Phys. Chem. A 2020, 124, 9617−9625 Read Online

ACCESS | Metrics & More | Article Recommendations | Supporting Information

ABSTRACT: Polystyrene beads are often used as test particles in aerosol science. Here, a contact-less technique is reported for determining the refractive index of a solid aerosol particle as a function of wavelength and temperature (20−234 °C) simultaneously. Polystyrene beads with a diameter of 2 μm were optically trapped in air in the central orifice of a ceramic heating element, and Mie spectroscopy was used to determine the radius and refractive index (to precisions of 0.8 nm and 0.0014) of eight beads as a function of heating and cooling. Refractive index, n, as a function of wavelength, λ (0.480−0.650 μm), and temperature, T, in centigrade, was found to be $n = 1.5753 - (1.7336 \times 10^{-4})T + (9.733 \times 10^{-3})\lambda^{-2}$ in the temperature range $20 < T < 100$ °C and $n = 1.5877 - (2.9739 \times 10^{-4})T + (9.733 \times 10^{-3})\lambda^{-2}$ in the temperature range $100 < T < 234$ °C. The technique represents a step change in measuring the refractive index of materials across an extended range of temperature and wavelength in an absolute manner and with high precision.

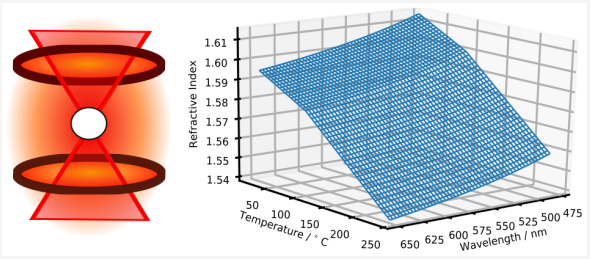

INTRODUCTION

The real component of the refractive index of a material is important for modelling the light scattering of aerosol.[1] In the atmosphere, it is especially critical in the evaluation of radiative forcing for modern climate change.[2] As a material is heated, its volume will change due to thermal expansion and any phase changes, causing a change in the refractive index of that material. There is a need to measure the refractive index of aerosol in the visible spectrum at elevated temperatures for the calculation of light scattering from aerosol produced by processes such as wildfires[3,4] and biogenic and anthropogenic combustion.[5−8] The intensity of light scattered back to space from aerosol in the Earth's atmosphere is a strong function of the aerosol particle's size and refractive index.[1]

An emerging issue in atmospheric science is the transportation and deposition of microplastics as they may pose serious risks to both human health and the environment.[9−15] It is therefore useful to study the refractive index of one such plastic, polystyrene.

Polystyrene beads are frequently used in atmospheric and aerosol science as test aerosol particles and for the calibration of instruments such as nephelometers[16−19] and cavity ring-down aerosol spectrometers.[20−22] Precise measurement of the temperature dependence of the refractive index of polystyrene beads is required for an accurate calibration of such instruments. Miles *et al.*[23] reported that uncertainties in the size and real refractive index of the polystyrene beads, used for the calibration of aerosol cavity ring-down spectroscopy, lead to errors of up to 2.9% in the measurements of refractive index, demonstrating the need for accurate determinations of the refractive index of polystyrene beads. The uncertainty highlighted in the work by Miles *et al.*[23] would obviously be larger at elevated temperatures because the temperature dependence of the refractive index of the polystyrene beads used for calibration was unknown.

More traditional methods of measuring the refractive index of a material, such as ellipsometry[24] and refractometry,[25] have previously been used to determine the refractive index of macroscopic thin films of polystyrene as a function of temperature.[26−28] Ellipsometry uses the difference in polarization between the incident and refracted light from a thin film on a surface. Beaucage *et al.*[26] and Efremov *et al.*[28] used ellipsometry to calculate the refractive index of thin films of polystyrene as a function of temperature. Krause and Lu[27] used a Bausch and Lomb precision refractometer, which measures the angle at which light is refracted when passed through a thin film of material, to determine the refractive index. These methods are normally used on macroscopic thin films and for a single wavelength.

In an alternative method, He *et al.*[29] used microsphere imaging to calculate the refractive index of several polymer beads as a function of temperature. Illuminating the micro-

Received: July 4, 2020
Revised: October 21, 2020
Published: November 9, 2020

https://dx.doi.org/10.1021/acs.jpca.0c06121
J. Phys. Chem. A 2020, 124, 9617−9625

spheres while they are submerged in oil gives rise to a dark ring in their image. The refractive index can then be determined from the ratio of the size of the dark ring to the size of the microsphere. The microsphere imaging described by He *et al.*[29] only determines the refractive index at one wavelength of light, and measurements are dependent on the values and uncertainties of the refractive index of the oil used. The temperature dependences of the refractive index of polystyrene reported by Beaucage *et al.*,[26] Efremov *et al.*,[28] He *et al.*,[29] and Krause and Lu[27] do not agree and are limited to single wavelengths. Thus, there is a need for a technique that can report the wavelength-dependent refractive index of polystyrene as a function of temperature. It would be advantageous if the method avoided potential contamination by oils and did not rely on the value and uncertainty of a reference refractive index.

Described here, optical trapping was used along with a ceramic toroidal-shaped heater to record the Mie spectra (intensity of back-scattered white light as a function of visible wavelength) produced by polystyrene beads of approximately 2 μm diameter, trapped in air, as the temperature was varied between 20 °C and a maximum of 234 °C through a range of heating and cooling cycles. Measurements were taken across the glass transition temperature, T_g, and up to the melting point of polystyrene. The glass transition temperature, T_g, is the temperature at which a polymer transitions from an equilibrium, liquid-like or rubbery state, into a nonequilibrium glassy state as a result of the restriction of molecular mobility.[30] The glass transition causes significant additional change in the refractive index of polystyrene. The method described here was used to determine the glass transition temperature of airborne polystyrene particles.

Optical trapping is a powerful technique for studying the Mie scattering of airborne particles.[31−39] Precise measurements of both the radius and wavelength-resolved refractive index have been obtained to a precision of ±0.8 nm and ±0.0014, respectively, by reproducing experimental Mie spectra of trapped particles with calculated Mie spectra using known values of radius and wavelength-resolved refractive index. Polystyrene was an exemplary material for this study as it has two well-known phase transitions, its glass transition temperature, which has been reported as values between 96.9 and 107 °C[40−44] and its melting point 240 °C.[40] The phase transition temperatures have been used to validate the experimental variation of refractive index with temperature measurement.

METHOD

The strategy for performing the experiment was to levitate an airborne, solid, spherical, polystyrene bead in air using an optical trap.[32] Throughout this paper, the back-scattered white light from the trapped particle is referred to as a Mie spectrum. The temperature in the trapping cell was changed in steps, allowing the temperature to equilibrate between the apparatus and the bead at each step. The Mie spectra of back-scattered light was continuously recorded using a spectrometer with a 3 s integration. These experimental Mie spectra were then compared to calculated theoretical spectra from a known refractive index as a function of wavelength, described by a Cauchy equation,[45] and a known radius to determine the refractive index of the bead as a function of both wavelength and temperature.

Optical Trapping of Airborne Particles. The optical setup of the laser trap is shown in Figure 1 and has been described in detail previously.[32] A 1064 nm Nd:YAG laser (Laser Quantum) was coupled to two single-mode fiber-optic cables *via* a beam-splitter coupling port (Oz Optics) to deliver laser beams of power 10 and 15 mW (measured at the point of focus) pointing upward and downward, respectively. The beams were focused using two Mitutoyo M Plan Apo ×50 NA 0.42 objectives into an aluminum trapping cell and aligned to submicron accuracy using a 3-axis piezo-electric stage (Physik Instrumente). Polystyrene beads (Invitrogen batch S37500) of reported diameter 2 ± 0.1 μm suspended in water were aerosolized using an atomizer (Topas, ATM 220) and delivered as dry beads into the aluminum trapping cell *via* a diffusion dryer filled with silica gel. The process of trapping involved several beads being delivered into the cell, and the position of the cell containing the aerosol was adjusted relative to the laser focus until a single bead was trapped at the point of focus. The remaining beads were removed by collisions with the cell walls over a period of approximately 2 min.

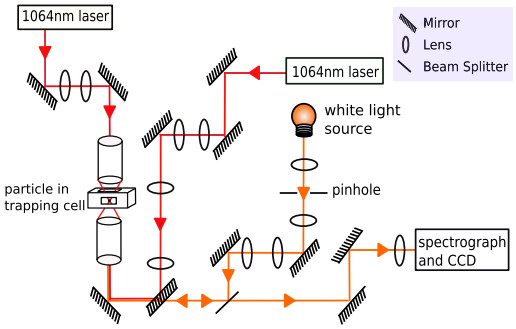

Figure 1. Optical set up of laser trap.

Heating Apparatus. The toroidal-shaped ceramic heater (Thorlabs HT19R) was placed inside the aluminum trapping cell, such that the focus of the counter-propagating laser beams is delivered through the 4 mm aperture in the heater; see Figure 2. The heated volume inside the torus and thus adjacent to where a polystyrene bead was to be held in the optical trap was ~0.5 cm^3.

The ceramic heater was used to control the temperature of the polystyrene bead and surrounding air. A detailed diagram of the heating cell is shown in Figure 2. The top and bottom

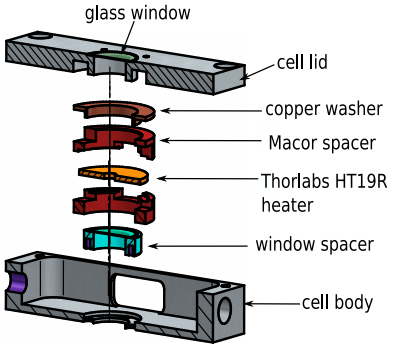

Figure 2. Schematic of the cross-section of the aluminum trapping cell demonstrating the positioning of the heater. The long axis of the cell is 7.8 cm and the width is 3.2 cm. The two circular holes on the right hand side of the diagram are for addition and exhaust of aerosol. The counter propagating beams enter from above and below the cell in this orientation.

https://dx.doi.org/10.1021/acs.jpca.0c06121
J. Phys. Chem. A 2020, 124, 9617−9625

heater clamps were constructed from Macor. Macor is a low thermal conductivity composite and thus insulates the heating element from the external components of the cell. The temperature of the polystyrene particle was set by the current flowing through the heater. The temperature was calibrated by placing a K-type thermocouple in the center of the heater instead of the trapped particle. During the experiments with a trapped polystyrene bead, the temperature of the heater was monitored by a K-type thermocouple in contact with the heater. The uncertainty in the temperature of the particle in the trap was estimated to be ±1 °C based on the calibration technique.

Mie Spectroscopy for Trapped Particles. As depicted in Figure 1, an LED white light source (Comar 01 LP 555, 6 V) with a typical white LED spectrum (*e.g.*, similar to Thorlabs MCWHL6) illuminated the trapped bead from below. Visible light back-scattered from the polystyrene bead was collected over the wavelength range of 480−660 nm at a resolution of 0.13 nm and focused into a spectrograph (Acton SP2500i, 300 groove mm^{-1} grating). The collected Mie spectrum was then imaged onto a charge-coupled device detector (Princeton Instrument Spec 10:400 BR). The wavelength of the spectrograph was calibrated using the gas discharge spectral lines produced by a Hg−Ne PenRay lamp.

Mie spectra were accumulated over 3 s intervals continuously for each of the polystyrene beads as the temperature was changed. Descriptions of the experiments performed on each bead are summarized in Table 1. The typical rate of heating/cooling of the beads was ∼1.8 °C min^{-1} for all experiments. For comparison, He *et al.*[29] cooled polystyrene beads at a rate of 10 °C min^{-1}; Krause and Lu[27] cooled polystyrene thin films at a rate of 0.33 °C min^{-1} until 10 °C before T_g, then at 0.167 °C min^{-1} until just before T_g, and then at 0.0017 °C min^{-1} in the vicinity of T_g.

Table 1. Summary of Heating/Cooling Cycles

bead	maximum temperature/°C	heating/cooling cycles
PB1	163	heated, cooled
PB2	234	heated up to melting point
PB3	147	heated, cooled
PB4	151	heated, cooled, reheated
PB5	180	heated, cooled (quickly 3 times)
PB6	180	heated, cooled (quickly 3 times)
PB7	180	heated, cooled (quickly once)
PB8	175	heated, cooled

Data Analysis. It is possible to determine the size and wavelength-dependent refractive index of a particle using the Mie spectral peak positions only[32,46−48] or the profile of the Mie spectrum in combination with peak positions.[49,50] Before describing the results, it is useful to explain how the experimental Mie spectra will be modelled to determine the radius and the wavelength-dependent refractive index. For the work described here, only the peak positions of the Mie spectra were used for determining the refractive index and diameter of the particle.

Generating Theoretical Mie Spectra. The technique described here determines the refractive index, n, as a function of wavelength, λ, using the Cauchy equation[45]

$$n = A + \frac{B}{\lambda^2} + \frac{C}{\lambda^4} \quad (1)$$

where A, B, and C are material-dependent, empirical constants needed to determine the refractive index as a function of wavelength, λ, of the polystyrene beads. The fitting process is carried out in two steps, named either the "grid-scan" or the "Cauchy fitting."

First, a large parameter space (typically $\sim 10^6$ calculations) for potential values of A, B, C, and the radius was searched using a "grid-scan" method. A second step then refined the best-fit values of A, B, C, and the radius produced by the grid-scan. The best-fit values of A, B, C, and radius were found as those that minimized the difference between the experimental and calculated peak wavelength positions in the Mie spectra. The fitting process *a priori* assumes that the wavelength dispersion of the refractive index was described by a Cauchy equation and that the particle was a sphere.

Step 1: Grid-Scan Search. In order to determine the radius and values for the constants A, B, and C from eq 1 and to reproduce the experimentally measured Mie spectra, theoretical Mie spectra were calculated using the method described by Bohren and Huffman[51] in their Fortran BHMie code. A program was written in Python3 based on the BHMie method that was modified for calculating the scattering over the numerical aperture of the objective lens at 0.5° intervals to match our experimental data. The program was used to generate a four-dimensional space of theoretical spectra for a given range of each of the parameters A, B, C, and radius, r. A grid search of such a large parameter space allowed for the identification and disregard of false minima.[49] The figure-of-merit for assessing a goodness-of-fit between the calculated and experimental Mie spectra was the average difference between the experimental and calculated peak positions in the wavelength range 480−650 nm. The values of the parameters, A, B, C, and r, that describe the theoretical spectrum with the smallest average peak position difference relative to the experimental Mie spectrum were taken as the starting point for the secondary step in the fitting process, "Cauchy fitting." The resolution of the four-dimensional grid-scan search is as follows: A at a precision of 1×10^{-4}, B at a precision of 5×10^{-5} μm^2, C at a precision of 1×10^{-6} μm^4, radius at a precision of 2 nm, and wavelength at a precision of 0.05 nm. The "Cauchy fitting" step was at higher precision, so finer resolution at this stage was unwarranted.

Step 2: Cauchy Fitting. For a range of radii (10 nm above and below the "best radius" found from the grid-scan step at a precision of 1 nm), each peak in the experimental Mie spectrum was fitted using a peak comparison to the equivalent peak in the theoretical spectrum. ±10 nm was found to be a reasonable range that resulted in finding a clear best-fit and therefore the most probable radius.[52] For each value of radius, the refractive index at each wavelength that corresponded to a peak position was then plotted as a function of wavelength. A Cauchy curve was then fit to the refractive indices against the wavelength plot using a Levenberg−Marquardt algorithm. A figure of merit, ϕ, was found for each Cauchy curve by combining the errors of each of the Cauchy parameters, A, B, and C, using the equation

$$\phi = \sqrt{\sum_{i=1}^{N} \Delta A^2 + \frac{\Delta B^2}{\lambda_i^2} + \frac{\Delta C^2}{\lambda_i^4}} \quad (2)$$

where λ_i is the wavelength of the ith peak and N is the number of peaks in the Mie spectrum. The minimum in the resulting plot of ϕ versus radius along with the determined values of A,

https://dx.doi.org/10.1021/acs.jpca.0c06121
J. Phys. Chem. A 2020, 124, 9617−9625

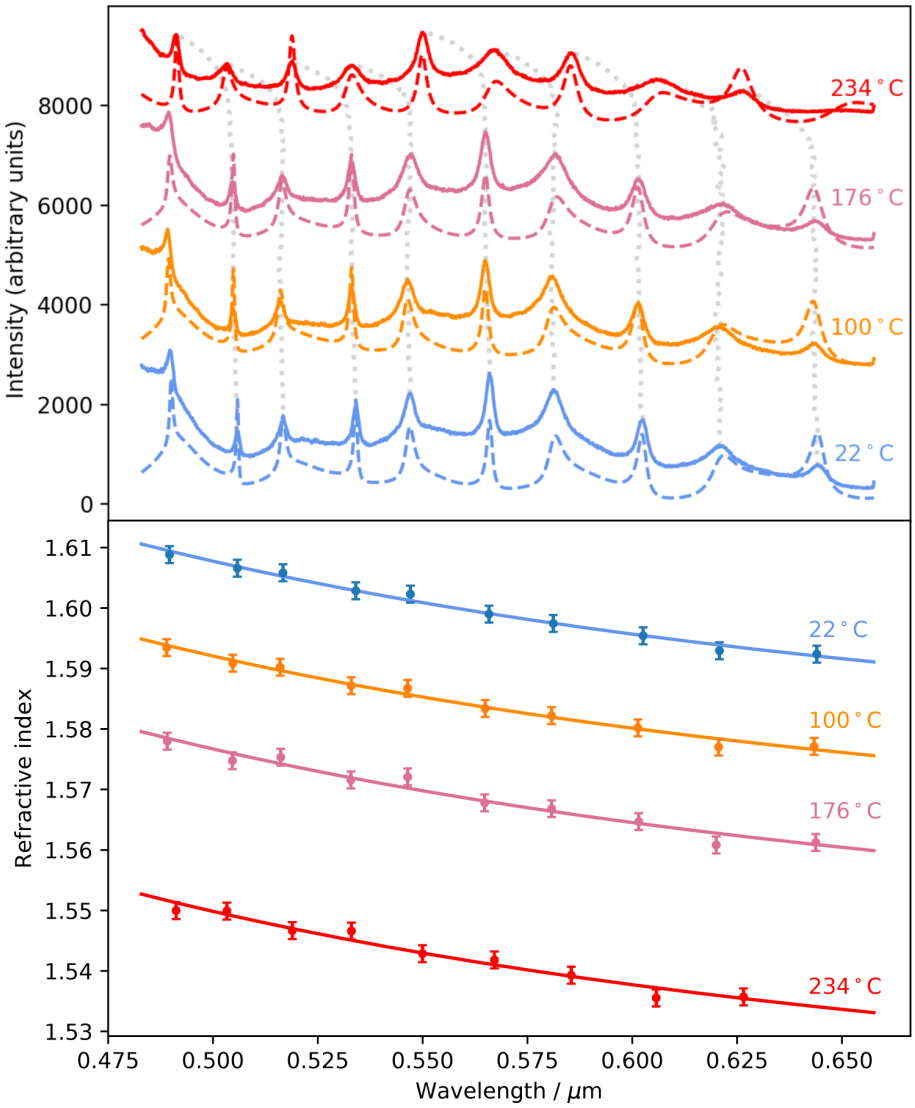

Figure 3. Top panel shows the experimental Mie spectra (solid lines) of polystyrene bead (PB2) in air at 22, 100, 176, and 234 °C. Each experimental Mie spectrum is compared with their matching calculated spectra (dashed lines) from Mie theory. The shift in peak positions between 22 and 234 °C is also shown as vertical dotted lines. Note that the spectra are shifted vertically for each temperature for clarity. The bottom panel shows the refractive index of a polystyrene bead as a function of wavelength for polystyrene bead PB2 at four separate temperatures. The points are plotted at the positions of peaks in the Mie spectrum. Uncertainty in refractive index is ±0.0014.

B, and *C* from the fit were taken to be the most probable parameters of the polystyrene bead.

The overall uncertainty for both steps of this fitting process was estimated by carrying out the two-step process on an indicative number (10) of spectra fitted per typical experiment. Ten different spectra of the same particle were taken 3 s apart and the standard deviation of the radii was determined for the 10 spectra. The standard deviation of the radii was found to be ±0.8 nm, which leads to an average uncertainty in the refractive index of ±0.0014.

Thermal Expansion Coefficient. The aim of this work was to produce a precise determination of the refractive index of polystyrene spheres as a function of temperature. However, the change in radius of the particle was also measured to a precision of ±0.8 nm, thus enabling a calculation of volume changes of the polystyrene bead with heating. The volumetric thermal expansion coefficient of a solid

$$\alpha_V = \frac{1}{V}\frac{\delta V}{\delta T} \tag{3}$$

where V is the volume of the solid and T is the temperature (δV is the fractional amount by which the volume will expand when heated by δT). Comparison of the volume change as a function of temperature with the literature values for polystyrene[40] will validate the calibration of the heating cell.

RESULTS

The results focus on the comparison of the experimental Mie spectra with the calculated Mie spectra. Comparison of the Mie spectra has enabled the determination of refractive index as a function of wavelength and size. The variation in these parameters with temperature was then reported to demonstrate the thermal expansion and phase change of spherical polystyrene beads.

https://dx.doi.org/10.1021/acs.jpca.0c06121
J. Phys. Chem. A 2020, 124, 9617−9625

Mie Spectra Fitting. Figure 3 shows the change in Mie spectra as a typical bead (PB2) was heated from room temperature, 22 to 234 °C. The melting point of polystyrene is 240 °C. The experimental data in Figure 3 are shown by the solid lines, and the calculated Mie spectra are shown by the dashed lines. Figure 3 demonstrates the excellent reproduction of the experimental data. The Mie spectra are vertically offset for clarity. The vertical dotted lines track the progression of the Mie spectra peak positions as the temperature rises.

Refractive Index Variation as a Function of Temperature. A total of eight different polystyrene beads were studied, as summarized in Table 1. The refractive index (at a wavelength of 589 nm) for all polystyrene beads studied as a function of temperature is shown in Figure 4. The real

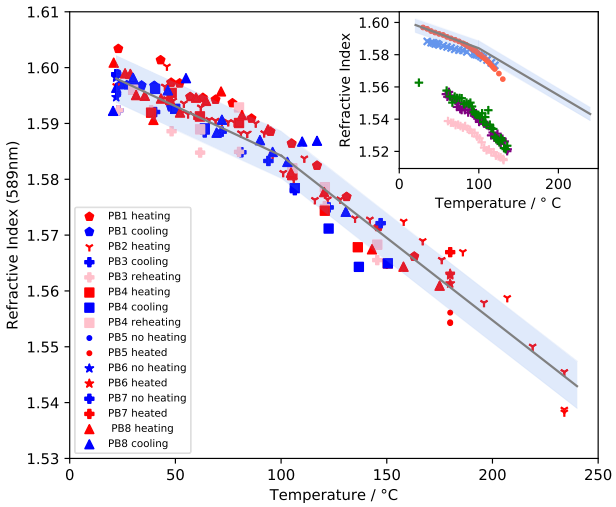

Figure 4. Refractive index at 589 nm for all polystyrene beads as a function of temperature. The gray line is a linear fit, to guide the eye, of the refractive index before and after T_g, determined from bead PB2 (T = 100.2, n = 1.5842). The shaded area represents 3 standard deviations in the refractive index. The inset replots the data, compared with results from He *et al.* (red dots: refractive index reported at 532 nm),[29] Beaucage *et al.* (green, purple, and pink "+" symbols: refractive index reported at 633 nm),[26] and Krause and Lu (blue "×" symbols: refractive index reported at 589 nm).[27]

component of the refractive index decreased with an increase in temperature. The rate of change in refractive index with temperature is different before and after the glass transition temperature (T_g). The rate of change of refractive index with temperature was found to be independent of the wavelength. A demonstration of the rate of change of refractive index being independent of wavelength is included in the Supporting Information. It is noted that beads from the same sample were polydisperse in both size and refractive index.[32] The range of measured refractive indices for the polystyrene bead sample was broad from 1.5923 to 1.6009 at room temperature. Thus, the phase change at T_g was calculated from a single bead (PB2) by extrapolation of linear fits between the refractive index and temperature between 20 and 90 and 110 and 150 °C. The intersection of these linear fits was at a temperature of 100.2 °C which falls into the range of literature values 96.9−107 °C.[40−44] There was no observation of hysteresis in either radius or refractive index over a cycle of heating and cooling.

The change in the refractive index as a function of temperature at a wavelength 589 nm for all beads is compared with the experiments by Krause and Lu[27] Beaucage *et al.*,[26] and He *et al.*[29] in Figure 4 (inset). It should be noted that the experiments by Beaucage *et al.*[26] and He *et al.*[29] were carried out at wavelengths of 633 and 532 nm, respectively, while the data plotted in Figure 4 and Krause and Lu[27] are reported at 589 nm. Figure 3 shows the refractive index of a bead (PB2) as a function of wavelength for a range of temperatures (22−234 °C), which demonstrates that the refractive index can be defined by a Cauchy eq 1 across the temperature range studied.

The wavelength-dependent variation of the refractive index is defined here by the parameters A, B, and C of the Cauchy eq 1. Figure 5 shows the values of A, B, and C as a function of

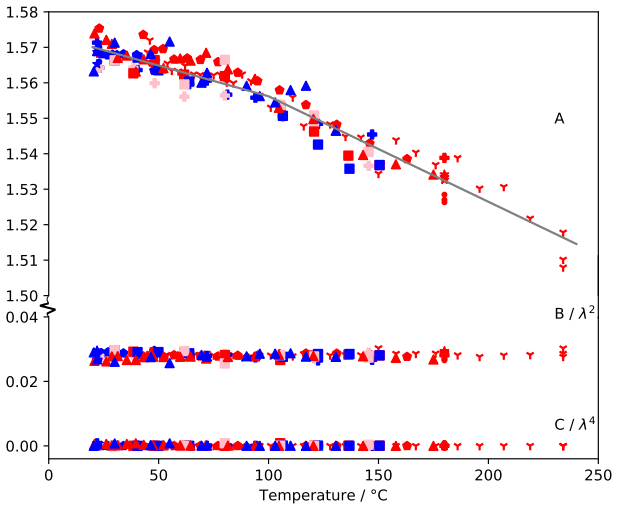

Figure 5. Cauchy eq 1 parameters A, B/λ^2, and C/λ^4 as a function of temperature. The plot demonstrates the contribution of each of the terms in eq 1 to the change in refractive index as a function of temperature. The legend is the same as the legend from Figure 4.

temperature. The variation in A was found to have statistically significant linear correlation with temperature below and above T_g, described by eqs 4 and 5

$$A = (1.5753 \pm 0.0072) - ((1.7336 \pm 0.0522) \times 10^{-4})T; \quad 22\ ^\circ\mathrm{C} < T < 100\ ^\circ\mathrm{C} \tag{4}$$

$$A = (1.5877 \pm 0.0140) - ((2.9739 \pm 0.1345) \times 10^{-4})T; \quad 100\ ^\circ\mathrm{C} < T < 234\ ^\circ\mathrm{C} \tag{5}$$

below and above T_g, respectively. Parameters B and C had no statistically significant correlation with temperature. The value of B is the average value 9.73 ± 0.3 × 10^{-3} μm^2 and C is effectively 0 μm^4. Thus, the change in refractive index with wavelength is summarized by the equations

$$n = (1.5753 \pm 0.0072) - ((1.7336 \pm 0.0522) \times 10^{-4})T + \frac{(9.7333 \pm 0.3001) \times 10^{-3}}{\lambda^2} \tag{6}$$

and

$$n = (1.5877 \pm 0.0140) - ((2.9739 \pm 0.1345) \times 10^{-4})T + \frac{(9.7333 \pm 0.3001) \times 10^{-3}}{\lambda^2} \tag{7}$$

https://dx.doi.org/10.1021/acs.jpca.0c06121
J. Phys. Chem. A 2020, 124, 9617−9625

in the temperature ranges 20 °C < T < 100 °C and 100 °C < T < 234 °C, respectively.

Thermal Expansion of Polystyrene Beads. The change in bead radius as a function of temperature was determined for all beads. Figure 6 shows the change in radius for bead PB2. All

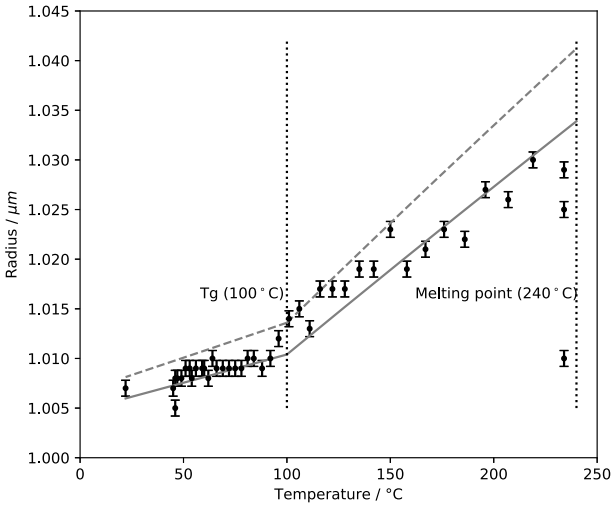

Figure 6. Radius as a function of temperature for polystyrene bead PB2 compared with minimum (solid line) and maximum (dashed line) radii based on literature values for the volumetric thermal expansion coefficient.[40]

other beads studied exhibited similar behavior, but because the bead size at room temperature for the other polystyrene beads varied between 0.986 and 1.007 μm, they are not shown for clarity.

Figure 6 shows the maximum and minimum theoretical radii calculated from the thermal expansion literature values of α_V, both below and above T_g.[40] Below the glass transition temperature, T_g, the expansion of the bead agrees with literature within literature uncertainty. Above T_g, the expansion of the polystyrene bead agrees with literature within literature uncertainty until 150 °C, after which there is slight deviation. Approaching 240 °C, the polystyrene bead starts to melt causing the volume to decrease rapidly.

DISCUSSION

Radius and Refractive Index as a Function of Temperature. The refractive index of polystyrene is dependent on its chemical and physical properties, following the Lorentz−Lorenz equation[53]

$$\frac{n^2 - 1}{n^2 + 2} = \frac{N\alpha\rho_m}{3M} \tag{8}$$

where n is the refractive index, ρ_m is the mass density, N is the Avogadro constant, α is the mean polarizability, and M is the molecular weight of polystyrene. As N and M are constant and α is found to be effectively constant with changing temperature,[54] the density is the significant factor determining the change in refractive index as a function of temperature.[55−57]

As the polystyrene beads are heated, thermal expansion causes the mass density ρ_m to decrease, causing a decrease in the refractive index. This is consistent with the results found in this study, where an increase in radius and a decrease in refractive index were found as the temperature increased, with the rate of change of the refractive index with temperature increasing at the glass transition temperature because of physical changes occurring more rapidly at this point.

Measurements were carried out from room temperature to 234 °C, just below the melting point of polystyrene (240 °C) without disturbing the optical trapping stability. The particle was stable in the trap throughout the changes. Even approaching the melting temperature, the bead was retained for sufficient time to enable spectral acquisitions, indicating a rapid loss of material, possibly due to evaporation of the shorter chain length polystyrene molecules. The wavelength-dependent refractive index determined at room temperature compares well within uncertainty with previous work.[32]

Figure 4 shows a comparison between the determined refractive index of all results obtained and the results from He *et al.*,[29] Beaucage *et al.*,[26] and Krause and Lu,[27] which were all monochromatic studies. The inset in Figure 4 compares the refractive index data recorded by others[26,27,29] at similar, but different, wavelengths. There is good agreement between this study and He *et al.*,[29] before the glass transition temperature (T_g), whereas Krause and Lu[27] found the refractive index to be slightly lower and Beaucage *et al.*[26] found the refractive index to be substantially lower. The offset observed between this study and those of Krause and Lu and Beaucage *et al.* is likely to be due to differences in the properties of the polystyrene studied. The glass transition temperatures for all four studies were 100.2 °C for this study, 98.3 °C for He *et al.*, 100 °C for Krause and Lu, and 86.4, 91.6, and 111.5 °C for Beaucage *et al.* at different film thicknesses.

The polystyrene beads used by He *et al.* were immersed in oil and were approximately 60 μm in diameter, whereas here they were only approximately 2 μm in diameter. Both Krause and Lu and Beaucage *et al.* studied thin films of polystyrene. The heating rate was also different in each of the experiments. In this study, the beads were heated and cooled at ∼1.8 °C min^{-1}, He *et al.*[29] cooled polystyrene beads at a rate of 10 °C min^{-1}, Krause and Lu[27] cooled polystyrene thin films at a rate of between 0.33 and 0.0017 °C min^{-1}, and Beaucage *et al.* heated and cooled polystyrene films at a rate of 2 °C min^{-1}.

The recorded thermal expansion of a single polystyrene bead is in agreement with literature values of the thermal expansion of bulk polystyrene at temperatures below 150 °C, as shown in Figure 6. The difference above this temperature, namely, a lower expansion than expected, may be due to the loss of lower molecular weight material from the bead as it approaches the melting point. He *et al.*, Krause and Lu, and Beaucage *et al.* all do not exceed 140 °C in their reported measurements.

A limitation of this technique is that only one particle can be studied at a time. However, the technique can be used to determine the refractive index over a range of wavelengths between 480 and 650 nm, rather than for a single wavelength, and the size of the particle at the same time. It would also be possible to determine the change in density with temperature, provided the density at room temperature is known. The technique gives an absolute measurement and therefore is not measured relative to the refractive index of another material. As the particles are airborne rather than submerged in oil, it is a contact-less method and the medium (air) will not affect the light scattered by the particle or have the potential for particle contamination. Air is an excellent choice of bath gas because its refractive index variation with temperature is well documented and is almost unity, within the precision of our experiment. The refractive index of air does change slightly with

https://dx.doi.org/10.1021/acs.jpca.0c06121
J. Phys. Chem. A 2020, 124, 9617−9625

temperature; it is 1.00027 at room temperature and 1.00021 at 100 °C,[58] and it was found that this change in refractive index of the medium led to no significant change in the determined refractive index or size of the particle within uncertainty and therefore does not need to be considered.

Polystyrene as a Test Aerosol. Polystyrene has two distinct phase changes in the temperature range studied. These may be used as reference points to accurately calibrate recorded temperatures, and polystyrene is an excellent test aerosol for this system. Figure 6 shows that the glass transition temperature was seen to occur at the expected temperature of 100 °C,[40] and there was evidence for a phase transition approaching the melting temperature of 240 °C,[40] which gives confidence in this method.

CONCLUSIONS

A technique has been developed with clear applications in combustion aerosol science, heterogeneous catalysis, and climate science for precisely determining the wavelength dispersion of refractive index, as a function of temperature, for trapped airborne particles. By determining the refractive index of polystyrene beads, as a function of wavelength and temperature simultaneously, and the size as a function of temperature, it has been demonstrated that the technique is robust due to polystyrene's known phase changes. A contactless method has been demonstrated for measuring the refractive index associated with the phase changes of polystyrene. Presence of a contact surface may compromise such measurements. The technique has the potential to be applied to other airborne particles for measuring the refractive index dispersion during liquid-to-solid or solid-to-liquid phase changes. The glass transition temperature of polystyrene has been reported as 100 °C, and the temperature range of the recorded behavior of polystyrene as a function of temperature has been extended by ∼100 °C using a polychromatic method.

There is potential for an increase in the temperature range that can be studied using this technique. Higher temperatures could be reached through better insulation and improved cell design. Temperatures below room temperature could be reached by cooling the aluminum cell.

The work presented here represents a step change in measuring the refractive index of airborne particles in an absolute manner, with high precision, as a function of both temperature and wavelength. The work also demonstrates a new development in the measurement of the refractive index of airborne particles, as a function of wavelength and temperature, for measuring in situ phase changes.

ASSOCIATED CONTENT

Supporting Information

The Supporting Information is available free of charge at https://pubs.acs.org/doi/10.1021/acs.jpca.0c06121.

Raw data and full results (ZIP)

Laser power measurement and uncertainty in temperature (PDF)

AUTHOR INFORMATION

Corresponding Author

Andrew D. Ward − *STFC, Central Laser Facility, Research Complex at Harwell, Rutherford Appleton Laboratory, Didcot, Oxfordshire OX11 0FA, U.K.;* orcid.org/0000-0001-6946-2391; Email: andy.ward@stfc.ac.uk

Authors

Megan R. McGrory − *STFC, Central Laser Facility, Research Complex at Harwell, Rutherford Appleton Laboratory, Didcot, Oxfordshire OX11 0FA, U.K.; Department of Earth Sciences, Royal Holloway University of London, Egham, Surrey TW20 0EX, U.K.;* orcid.org/0000-0003-1016-5573

Martin D. King − *Department of Earth Sciences, Royal Holloway University of London, Egham, Surrey TW20 0EX, U.K.;* orcid.org/0000-0002-0089-7693

Complete contact information is available at: https://pubs.acs.org/10.1021/acs.jpca.0c06121

Notes

The authors declare no competing financial interest.

Raw data and full set of results are available at DOI: 10.5281/zenodo.3885730.

ACKNOWLEDGMENTS

The authors thank NERC for funding of grant NE/R012148/1. We are also grateful to STFC for support under grant 18130025 and for access to the laboratories of the Central Laser Facility at the Research Complex at Harwell. We thank Brian Landowski (CLF) for advice in the sample cell construction. We also thank Olivia Ward for assistance in collecting data for bead PB8 during her placement at the Central Laser Facility.

REFERENCES

(1) Haywood, J. M.; Ramaswamy, V.; Soden, B. J. Tropospheric Aerosol Climate Forcing in Clear-Sky Satellite Observations over the Oceans. *Science* **1999**, *283*, 1299−1303.

(2) IPCC. *Climate Change 2013: The Physical Science Basis. Contribution of Working Group I to the Fifth Assessment Report of the Intergovernmental Panel on Climate Change*, 2013.

(3) Gyawali, M.; Arnott, W. P.; Lewis, K.; Moosmüller, H. In situ aerosol optics in Reno, NV, USA during and after the summer 2008 California wildfires and the influence of absorbing and non-absorbing organic coatings on spectral light absorption. *Atmos. Chem. Phys.* **2009**, *9*, 8007−8015.

(4) Niemi, J. V.; Tervahattu, H.; Vehkamäki, H.; Martikainen, J.; Laakso, L.; Kulmala, M.; Aarnio, P.; Koskentalo, T.; Sillanpää, M.; Makkonen, U. Characterization of aerosol particle episodes in Finland caused by wildfires in Eastern Europe. *Atmos. Chem. Phys. Discuss.* **2005**, *5*, 2469−2501.

(5) Guazzotti, S. A.; Suess, D. T.; Coffee, K. R.; Quinn, P. K.; Bates, T. S.; Wisthaler, A.; Hansel, A.; Ball, W. P.; Dickerson, R. R.; Neusüß, C.; et al. Characterization of carbonaceous aerosols outflow from India and Arabia: Biomass/biofuel burning and fossil fuel combustion. *J. Geophys. Res.: Atmos.* **2003**, *108*, 4485.

(6) Gustafsson, O.; Krusa, M.; Zencak, Z.; Sheesley, R. J.; Granat, L.; Engstrom, E.; Praveen, P. S.; Rao, P. S. P.; Leck, C.; Rodhe, H. Brown Clouds over South Asia: Biomass or Fossil Fuel Combustion? *Science* **2009**, *323*, 495−498.

(7) Yan, C.; Zheng, M.; Shen, G.; Cheng, Y.; Ma, S.; Sun, J.; Cui, M.; Zhang, F.; Han, Y.; Chen, Y. Characterization of carbon fractions in carbonaceous aerosols from typical fossil fuel combustion sources. *Fuel* **2019**, *254*, 115620.

(8) Roberts, D. L.; Jones, A. Climate sensitivity to black carbon aerosol from fossil fuel combustion. *J. Geophys. Res.: Atmos.* **2004**, *109*, D16202.

(9) Chen, G.; Feng, Q.; Wang, J. Mini-review of microplastics in the atmosphere and their risks to humans. *Sci. Total Environ.* **2020**, *703*, 135504.

(10) Zhang, Y.; Gao, T.; Kang, S.; Sillanpää, M. Importance of atmospheric transport for microplastics deposited in remote areas. *Environ. Pollut.* **2019**, *254*, 112953.
(11) Dris, R.; Gasperi, J.; Saad, M.; Mirande, C.; Tassin, B. Synthetic fibers in atmospheric fallout: A source of microplastics in the environment? *Mar. Pollut. Bull.* **2016**, *104*, 290−293.
(12) Zhang, Y.; Kang, S.; Allen, S.; Allen, D.; Gao, T.; Sillanpää, M. Atmospheric microplastics: A review on current status and perspectives. *Earth-Sci. Rev.* **2020**, *203*, 103118.
(13) Obbard, R. W. Microplastics in Polar Regions: The role of long range transport. *Curr. Opin. Environ. Sci. Health* **2018**, *1*, 24−29.
(14) Bergmann, M.; Mützel, S.; Primpke, S.; Tekman, M. B.; Trachsel, J.; Gerdts, G. White and wonderful? Microplastics prevail in snow from the Alps to the Arctic. *Sci. Adv.* **2019**, *5*, No. eaax1157.
(15) Allen, S.; Allen, D.; Phoenix, V. R.; Le Roux, G.; Durántez Jiménez, P.; Simonneau, A.; Binet, S.; Galop, D. Atmospheric transport and deposition of microplastics in a remote mountain catchment. *Nat. Geosci.* **2019**, *12*, 339−344.
(16) Sloane, C. S.; Rood, M. J.; Rogers, C. F. Measurements of Aerosol Particle Size: Improved Precision by Simultaneous Use of Optical Particle Counter and Nephelometer. *Aerosol Sci. Technol.* **1991**, *14*, 289−301.
(17) Leong, K. H.; Jones, M. R.; Holdridge, D. J.; Ivey, M. Design and Test of a Polar Nephelometer. *Aerosol Sci. Technol.* **1995**, *23*, 341−356.
(18) Dolgos, G.; Martins, J. V. Polarized Imaging Nephelometer for in situ airborne measurements of aerosol light scattering. *Opt. Express* **2014**, *22*, 21972−21990.
(19) Manfred, K. M.; Washenfelder, R. A.; Wagner, N. L.; Adler, G.; Erdesz, F.; Womack, C. C.; Lamb, K. D.; Schwarz, J. P.; Franchin, A.; Selimovic, V.; et al. Investigating biomass burning aerosol morphology using a laser imaging nephelometer. *Atmos. Chem. Phys.* **2018**, *18*, 1879−1894.
(20) Abo Riziq, A.; Erlick, C.; Dinar, E.; Rudich, Y. Optical properties of absorbing and non-absorbing aerosols retrieved by cavity ring down (CRD) spectroscopy. *Atmos. Chem. Phys.* **2007**, *7*, 1523−1536.
(21) Toole, J. R.; Renbaum-Wolff, L.; Smith, G. D. A Calibration Technique for Improving Refractive Index Retrieval from Aerosol Cavity Ring-Down Spectroscopy. *Aerosol Sci. Technol.* **2013**, *47*, 955−965.
(22) Nakayama, T.; Hagino, R.; Matsumi, Y.; Sakamoto, Y.; Kawasaki, M.; Yamazaki, A.; Uchiyama, A.; Kudo, R.; Moteki, N.; Kondo, Y.; et al. Measurements of aerosol optical properties in central Tokyo during summertime using cavity ring-down spectroscopy: Comparison with conventional techniques. *Atmos. Environ.* **2010**, *44*, 3034−3042.
(23) Miles, R. E. H.; Rudić, S.; Orr-Ewing, A. J.; Reid, J. P. Influence of Uncertainties in the Diameter and Refractive Index of Calibration Polystyrene Beads on the Retrieval of Aerosol Optical Properties Using Cavity Ring Down Spectroscopy. *J. Phys. Chem. A* **2010**, *114*, 7077−7084.
(24) Ogieglo, W.; Wormeester, H.; Eichhorn, K.-J.; Wessling, M.; Benes, N. E. In situ ellipsometry studies on swelling of thin polymer films: A review. *Prog. Polym. Sci.* **2015**, *42*, 42−78.
(25) Wu, C.; Xia, K.-Q. Incorporation of a differential refractometer into a laser light-scattering spectrometer. *Rev. Sci. Instrum.* **1994**, *65*, 587.
(26) Beaucage, G.; Composto, R.; Stein, R. S. Ellipsometric study of the glass transition and thermal expansion coefficients of thin polymer films. *J. Polym. Sci., Part B: Polym. Phys.* **1993**, *31*, 319−326.
(27) Krause, S.; Lu, Z.-H. Refractive index-temperature measurements on anionically polymerized polystyrene. *J. Polym. Sci., Polym. Phys. Ed.* **1981**, *19*, 1925−1928.
(28) Efremov, M. Y.; Soofi, S. S.; Kiyanova, A. V.; Munoz, C. J.; Burgardt, P.; Cerrina, F.; Nealey, P. F. Vacuum ellipsometry as a method for probing glass transition in thin polymer films. *Rev. Sci. Instrum.* **2008**, *79*, 043903.
(29) He, J.; Liu, W.; Huang, Y.-X. Simultaneous Determination of Glass Transition Temperatures of Several Polymers. *PLoS One* **2016**, *11*, No. e0151454.
(30) Hutchinson, J. M. Determination of the glass transition temperature. *J. Therm. Anal. Calorim.* **2009**, *98*, 579.
(31) Ashkin, A.; Dziedzic, J. M.; Yamane, T. Optical trapping and manipulation of single cells using infrared laser beams. *Nature* **1987**, *330*, 769.
(32) Jones, S. H.; King, M. D.; Ward, A. D. Determining the unique refractive index properties of solid polystyrene aerosol using broadband Mie scattering from optically trapped beads. *Phys. Chem. Chem. Phys.* **2013**, *15*, 20735−20741.
(33) Wills, J. B.; Knox, K. J.; Reid, J. P. Optical control and characterisation of aerosol. *Chem. Phys. Lett.* **2009**, *481*, 153−165.
(34) Ashkin, A. Optical trapping and manipulation of neutral particles using lasers. *Proc. Natl. Acad. Sci. U.S.A.* **1997**, *94*, 4853−4860.
(35) Ashkin, A.; Dziedzic, J. M.; Bjorkholm, J. E.; Chu, S. Observation of a single-beam gradient force optical trap for dielectric particles. *Opt. Lett.* **1986**, *11*, 288−290.
(36) Preston, T. C.; Mason, B. J.; Reid, J. P.; Luckhaus, D.; Signorell, R. Size-dependent position of a single aerosol droplet in a Bessel beam trap. *J. Opt.* **2014**, *16*, 025702.
(37) Thanopulos, I.; Luckhaus, D.; Preston, T. C.; Signorell, R. Dynamics of submicron aerosol droplets in a robust optical trap formed by multiple Bessel beams. *J. Appl. Phys.* **2014**, *115*, 154304.
(38) David, G.; Esat, K.; Hartweg, S.; Cremer, J.; Chasovskikh, E.; Signorell, R. Stability of aerosol droplets in Bessel beam optical traps under constant and pulsed external forces. *J. Chem. Phys.* **2015**, *142*, 154506.
(39) Li, T. *Fundamental Tests of Physics with Optically Trapped Microspheres*; Springer Science & Business Media, 2012.
(40) *Polymer Handbook*, 4th ed.; Brandrup, J., Immergut, E. H., Grulke, E. A., Eds.; Wiley: New York, 1999.
(41) Rieger, J. The glass transition temperature of polystyrene. *J. Therm. Anal.* **1996**, *46*, 965−972.
(42) Richardson, M. J.; Savill, N. G. Derivation of accurate glass transition temperatures by differential scanning calorimetry. *Polymer* **1975**, *16*, 753−757.
(43) Aras, L.; Richardson, M. J. The glass transition behaviour and thermodynamic properties of amorphous polystyrene. *Polymer* **1989**, *30*, 2246−2252.
(44) Wunderlich, B.; Bodily, D. M.; Kaplan, M. H. Theory and Measurements of the Glass-Transformation Interval of Polystyrene. *J. Appl. Phys.* **1964**, *35*, 95−102.
(45) Jenkins, F. A.; White, H. E. *Fundamentals of Optics*; Mc Graw-Hill Primis Custom Publ.: New York, 2010.
(46) Jones, S. H.; King, M. D.; Ward, A. D. Atmospherically relevant core-shell aerosol studied using optical trapping and Mie scattering. *Chem. Commun.* **2015**, *51*, 4914−4917.
(47) Lew, L. J. N.; Ting, M. V.; Preston, T. C. Determining the size and refractive index of homogeneous spherical aerosol particles using Mie resonance spectroscopy. *Appl. Opt.* **2018**, *57*, 4601−4609.
(48) Conwell, P. R.; Rushforth, C. K.; Benner, R. E.; Hill, S. C. Efficient automated algorithm for the sizing of dielectric microspheres using the resonance spectrum. *J. Opt. Soc. Am. A* **1984**, *1*, 1181−1187.
(49) David, G.; Esat, K.; Ritsch, I.; Signorell, R. Ultraviolet broadband light scattering for optically-trapped submicron-sized aerosol particles. *Phys. Chem. Chem. Phys.* **2016**, *18*, 5477−5485.
(50) Schmitz, M.; Rothe, T.; Kienle, A. Evaluation of a spectrally resolved scattering microscope. *Biomed. Opt. Express* **2011**, *2*, 2665−2678.
(51) Bohren, C. F.; Huffman, D. R. *Absorption and Scattering of Light by Small Particles*; John Wiley & Sons, Ltd, 2007; pp 82−129.
(52) Huckaby, J. L.; Ray, A. K.; Das, B. Determination of size, refractive index, and dispersion of single droplets from wavelength-dependent scattering spectra. *Appl. Opt.* **1994**, *33*, 7112−7125.
(53) Lorentz, H. A. *The theory of electrons*; B. G. Teubner: New York, Leipzig, 1916.

https://dx.doi.org/10.1021/acs.jpca.0c06121
J. Phys. Chem. A 2020, 124, 9617−9625

(54) Fiaz, M.; Beevers, M. S. Temperature dependence of static dielectric permittivity and dipole moments of poly(N-vinylcarbazole). *Polymer* **1996**, *37*, 755−760.
(55) Priyadarshi, A.; Shimin, L.; Mhaisalkar, S. G.; Rajoo, R.; Wong, E. H.; Kripesh, V.; Namdas, E. B. Characterization of optical properties of acrylate based adhesives exposed to different temperature conditions. *J. Appl. Polym. Sci.* **2005**, *98*, 950−956.
(56) Liu, Y.; Daum, P. H. Relationship of refractive index to mass density and self-consistency of mixing rules for multicomponent mixtures like ambient aerosols. *J. Aerosol Sci.* **2008**, *39*, 974−986.
(57) Tan, C.-Y.; Huang, Y.-X. Dependence of Refractive Index on Concentration and Temperature in Electrolyte Solution, Polar Solution, Nonpolar Solution, and Protein Solution. *J. Chem. Eng. Data* **2015**, *60*, 2827−2833.
(58) Ciddor, P. E. Refractive index of air: new equations for the visible and near infrared. *Appl. Opt.* **1996**, *35*, 1566−1573.

https://dx.doi.org/10.1021/acs.jpca.0c06121
J. Phys. Chem. A 2020, 124, 9617−9625

SUPPORTING INFORMATION

Using Mie Scattering to Determine the Wavelength-Dependent Refractive Index of Polystyrene Beads with Changing Temperature

Megan R. McGrory,[†,‡] Martin D. King,[‡] and Andrew D. Ward[*,†]

†*STFC, Central Laser Facility, Research Complex at Harwell, Rutherford Appleton Laboratory, Harwell Oxford, Didcot, Oxfordshire, OX11 0FA, UK*

‡*Department of Earth Sciences, Royal Holloway University of London, Egham, Surrey, TW20 0EX, UK*

E-mail: andy.ward@stfc.ac.uk

The following 5 page supporting information document contains 2 paragraphs of information and 2 Figures.

Contents

List of Figures

1 Laser power measurement

Laser power was measured using a Thorlabs PM100A power meter with the sensor placed at the point of each focus. Beams were 4mm diameter at the entrance to the objective lenses. This diameter just overfills the back aperture of the objective lenses.

2 Uncertainty in temperature

The uncertainty in recorded temperature is ± 1°C, due to the sensitivity of the temperature sensor. A 1°C change in temperature will cause a change of 0.0002 and 0.0003 in refractive index before and after T_g respectively. As our reported uncertainty in refractive index is 0.0014, the sensitivity of the heater does not have a significant impact on the refractive index reported.

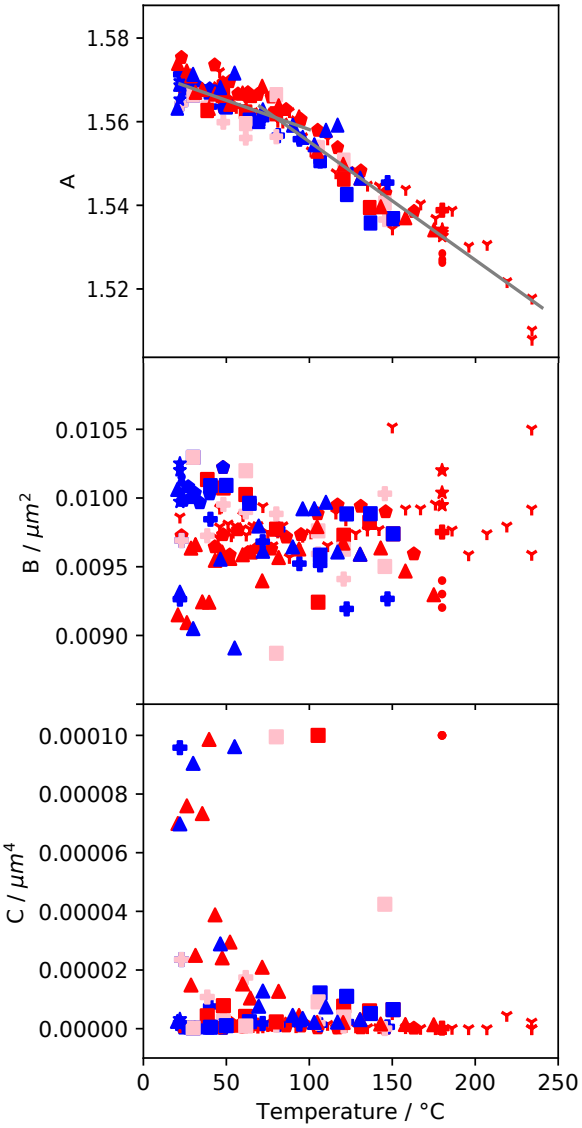

Figure S1: Variation in Cauchy parameters, A, B and C with temperature. B and C were not found to vary significantly with temperature, and were therefore taken as single values, for determining refractive index as a function of temperature and wavelength.

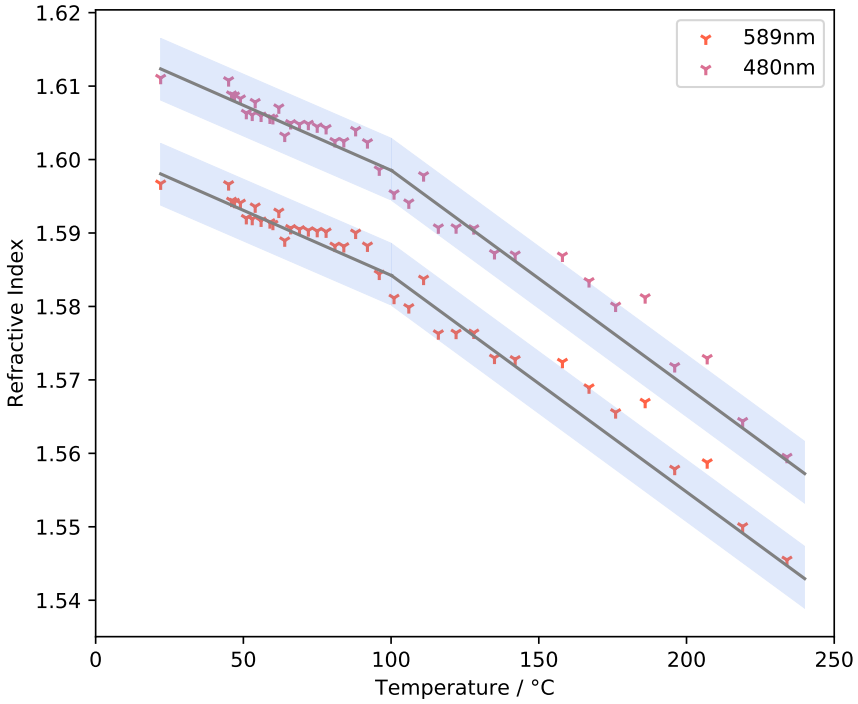

Figure S2: Temperature dependence of refractive index at different wavelengths. The behaviour of refractive index was found to be the same for all wavelengths within the range that was studied.

Chapter 4

Comparative study of silica beads, and measurement of the wavelength-dependant refractive index of silica beads

Megan R. McGrory, Martin D. King and Andrew D. Ward

Publication status: To be submitted for publication in the Journal of Aerosol Science

I declare I have made the following contributions to the piece of co-authored work:

- Conducted the experiments, and analysed all data collected
- Contributed to the conclusions drawn from the experiments conducted
- Wrote the first draft and, upon feedback from co-authors, completed all revisions of the paper

Are silica beads a poor standard: Variation in the size and refractive index of silica and glass beads

Megan R. McGrory[a,b], Martin D. King[a], Andrew D. Ward[b]

[a] *Department of Earth Sciences Royal Holloway University of London, Egham, TW20 0EX, Surrey, UK*
[b] *STFC Central Laser Facility Research Complex at Harwell, Rutherford Appleton Laboratory, Harwell, OX11 0FA, Oxfordshire, UK*

Abstract

Silica beads are often used for calibration of instruments and as a mineral aerosol proxy in atmospheric experiments, where having the correct size and refractive index of the beads is essential. Suppliers of silica beads may use slightly different variations of the Stöber process for production, producing beads of varying refractive index, and with varying distributions of size and refractive index. The accuracy and reliability of the given values of size and refractive index of samples of silica beads from three different suppliers; Whitehouse Scientific Ltd., Bangs Laboratories Inc., and Microspheres-Nanospheres Corpuscular Inc., were found to have refractive indices ranging from 1.3500 to 1.4442 at 589 nm, showing that the refractive index of bulk silica (~ 1.45) can not be assumed for all silica particles. One sample of borosilicate glass from Thermo Scientific Duke Standards has also been studied and was found to have a refractive index of 1.5197 at 589 nm.

If the assumed refractive index is different to the measured refractive index this could lead to an error in radius calculation. Based on the backscattering efficiency, of 0.006 µm (6%) for a particle of radius 0.1 µm, an error in radius of 0.14 µm (14%) for a particle of radius 1 µm, an error in radius of 2 µm (20%) for a particle of radius 10 µm.

Keywords: keyword one, keyword two
PACS: 0000, 1111
2000 MSC: 0000, 1111

1. Introduction

As silica is found abundantly in the atmosphere, silica beads are often used to test atmospheric measurement systems (Alois et al., 2017; Bohannon et al., 2017; Greswell et al., 2010), and have been used as an atmospheric aerosol proxy to study atmospheric core-shell systems (Jones et al., 2015). For atmospheric studies it is not only important that the size and refractive index of the silica beads are accurate, but that the refractive index is as close as possible to that of naturally occurring silica mineral aerosol particles. Silica (SiO_2) beads are also commonly used for many biological purposes, including biomolecular detection (Demir and Serpengüzel, 2005), drug delivery systems (Panagiotaki et al., 2020) and separating proteins (Unger et al., 1986). Silica beads are also used for the calibration of instruments such as electron microscopes (SEMs and TEMs) (Chen et al., 2011) and flow cytometers used to measure forward scattering of light from bacteria (Parida et al., 2015; Foladori et al., 2008). The correct size and refractive index of the silica bead is vital for correct calibration of these instruments.

Mono-disperse silica beads in aqueous solution are typically produced by the hydrolysis of a silica precursor (typically tetraethyl orthosilicate) in the presence of ethanol and ammonia, using the Stöber process (Stöber et al., 1968). The process used by manufacturers of silica beads is likely to be based on this process but may have variations. It has been shown that the Stöber process can produce silica beads of varying refractive indices based on the porosity of the beads produced. Silica beads of higher porosity will have a higher density and lower refractive index (Thomas, 1992; Tamar et al., 2014; Beganskiene et al., 2004). A study by Malitson (Malitson, 1965) determined the refractive index of fused bulk silica over a wavelength range of 0.21-3.7 µm, and determined a value of 1.4584 at 589 nm. A European report by the scientific committee on consumer safety (Scientific Committee on Consumer Safety, 2015) reported the refractive index of silica nanoparticles as 1.45 at unspecified wavelength and a study by Khlebtsov *et al.* (Khlebtsov et al., 2008) found the average refractive index of silica nanoparticles to be 1.475 ± 0.005 over the wavelength range 200-400 nm.

There are multiple manufacturers of silica beads. Each manufacturer provides a value of size, polydispersity, and typically a value of refractive index based on bulk silica. The aim of this study is to demonstrate the variation in refractive index in a single batch and also between silica beads produced by different manufacturers. In this study, samples from three sup-

pliers of silica beads: Whitehouse Scientific Ltd. (Catalogue No: MSS002), Bangs Laboratories Inc. (Catalogue No: SS04N, Manufacturer Lot number: 7920, Inventory number: L061215B), and Microspheres-Nanospheres Corpuscular Inc. (Catalogue No: 140212-10), and one supplier of borosilicate glass beads: Thermo Scientific Duke Standards (Catalogue No: 9002, Batch number: 9002-003), were tested and compared. The size and refractive index of approximately ten silica beads from each supplier were obtained using optical trapping combined with Mie spectroscopy (Jones et al., 2013; Preston et al., 2014; Thanopulos et al., 2014; David et al., 2015; McGrory et al., 2020; Jones et al., 2015; Shepherd et al., 2017). Optical trapping in air provides good contrast between the refractive index of the medium and the refractive index of the silica particles being studied. If the manufactures of the silica beads provide a refractive index for the beads, it will generally only be provided for a given wavelength (typically 589 nm). Mie spectroscopy allows for the determination of the wavelength-dependent real refractive indices, over the range 425−600 nm, for the four different suppliers of beads studied.

2. Method

The method used to study the silica and glass beads has been explained in detail elsewhere (McGrory et al., 2020; Jones et al., 2013). Briefly, the silica beads were held in air using optical trapping with a 1064 nm counter-propagating trap, and illuminated with white light. Mie spectra (the back-scattered light from particles with a size similar to the wavelength of the scattered light) over a wavelength range of 425−600 nm were collected over 3 second intervals using a spectrometer, with a resolution in wavelength of 0.131 nm. The set-up of the optical trap is the same as was used in previous work (McGrory et al., 2020; Jones et al., 2015). Silica beads of each sample were aerosolized from aqueous suspension using an atomizer (Topas, ATM 220) and released into the trapping cell via a diffusion dryer until a single bead was trapped. This process was repeated to trap 10 beads from each sample, all at room temperature and pressure.

The wavelength-dependent refractive index can be expressed using the Cauchy equation (Jenkins and White, 2010),

$$n = A + \frac{B}{\lambda^2} + \frac{C}{\lambda^4}, \tag{1}$$

where A, B, and C are material specific constants. Initial values of A, B, and C and radius of the silica beads were determined from their Mie spectra by

comparing the experimental Mie spectra to a range of calculated Mie spectra of known radius and refractive index, produced using Bohren and Huffman's formalism of Mie theory (Bohren and Huffman, 2008).

To improve the precision of the results obtained, the wavelength, λ, variation of refractive index, n, was constrained by a Levenberg-Marquardt algorithm, to reduce the parameters A, B, and C, to optimize the best fit to the Cauchy equation. The radius and wavelength-dependent refractive indices of the beads were determined to a precision of 1.2 nm and 0.0022 respectively. Further information on the method used for analysis of Mie spectra can be found in McGrory *et al.* (McGrory et al., 2020).

3. Results

A summary of the average determined values of refractive index at 589 nm and radius compared with the values quoted by the manufacturers are shown in Table 1. Table 2 shows the average Cauchy parameters, A, B and C, which describe the wavelength dependant refractive index, determined for each of the bead samples. The uncertainties of the determined values in both tables are the standard deviation of values found for each parameter.

	RI (at 589nm)		Radius / μm	
Supplier	Reported	Determined	Reported	Determined
Microspheres-Nanospheres Corpuscular Inc.	-	1.4328±0.0069	1.0±0.02	1.003±0.003
Whitehouse Scientific Ltd.	-	1.4175±0.0124	1.015±0.1575	1.016±0.052
Bangs Laboratories Inc.	1.43-1.46	1.3773±0.01030	1.035±0.1015	0.958±0.013
Thermo Scientific Duke Standards Inc. (borosilicate)	1.56	1.5197±0.0242	0.95±0.25	0.866±0.107

Table 1: Table comparing the average refractive index and radius of silica beads reported by the manufacturer, with the average values determined from the samples in this study. The uncertainties on the values determined in this study are the standard deviation of all values for each sample.

Supplier	A	B / μm^{-2}	C / μm^{-4}
Microspheres-Nanospheres Corpuscular Inc.	1.4234 ± 0.0062	0.0030 ± 0.0006	$6.93 \pm 4.14 \times 10^{-5}$
Whitehouse Scientific Ltd.	1.4093 ± 0.0127	0.0027 ± 0.0003	$4.27 \pm 4.93 \times 10^{-5}$
Bangs Laboratories Inc.	1.3713 ± 0.0103	0.0018 ± 0.0015	$1.20 \pm 1.24 \times 10^{-4}$
Thermo Scientific Duke Standards Inc. (borosilicate)	1.5035 ± 0.0247	0.0056 ± 0.0011	$2.52 \pm 7.48 \times 10^{-5}$

Table 2: Average Cauchy coefficients which describe the wavelength-dependent refractive index of each bead sample, with uncertainties showing the range of values found for each sample (valid for the wavelength range 425−600 nm)

Example experimental Mie spectra from each sample are shown in Figure 1 along with corresponding calculated spectra of their determined size and

refractive index. Figure 2 shows the wavelength dispersion of refractive index as a fitted Cauchy curve for each of the beads studied. The dispersion relation for the refractive index of bulk silica reported by Malitson et al (Malitson, 1965) is plotted as a dashed line in Figure 2 for comparison with the results determined in this study.

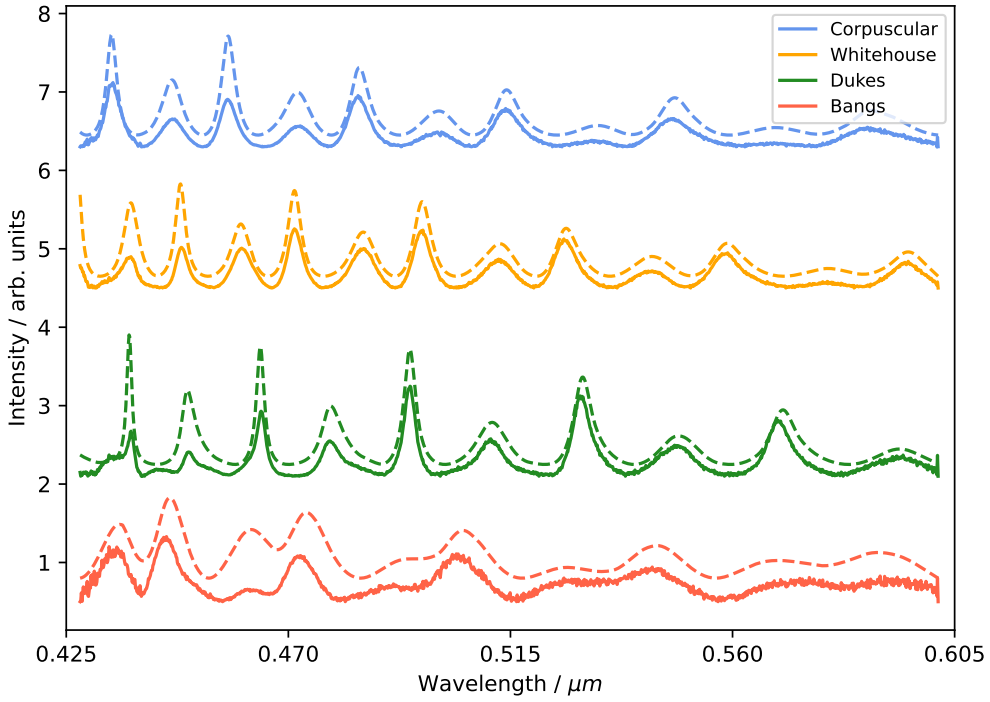

Figure 1: Example experimental spectrum from each of the bead samples compared with its corresponding theoretically generated spectrum (dashed) of known size and refractive index values. The intensity of each spectrum is a fair representation of the data.

The refractive index for the Corpuscular and Whitehouse samples were not stated. However, the beads from the Corpuscular and Whitehouse samples were found to have the closest values of refractive index to that of bulk silica ($\sim$ 1.45). The Corpuscular sample was found to have the smallest spread of values across the sample. It was noted that beads from the Bangs sample were found to have significantly lower values of refractive index than bulk silica, and lower than the quoted values from the manufacturer. The average refractive index of the borosilicate Dukes beads was slightly lower

than the quoted value from the manufacturer (1.56) and was much closer to the literature value of borosilicate glass ($\sim$ 1.52 (Serway et al., 2011)). The Dukes sample had a wider range of refractive index values than the other samples.

Figure 3 shows the histogram distribution of radii found for each of the bead samples studied. The distribution of radius across all of the samples was largest for the Dukes sample, followed by the Bangs sample, then the Whitehouse sample, and the Corpuscular sample was found to have the smallest distribution of radius values across the sample. The trend in distribution between the samples correspond to the manufacturers quoted values, and the determined values in this study. The determined radius of all beads studied were found to be within the manufacturers quoted values and uncertainties.

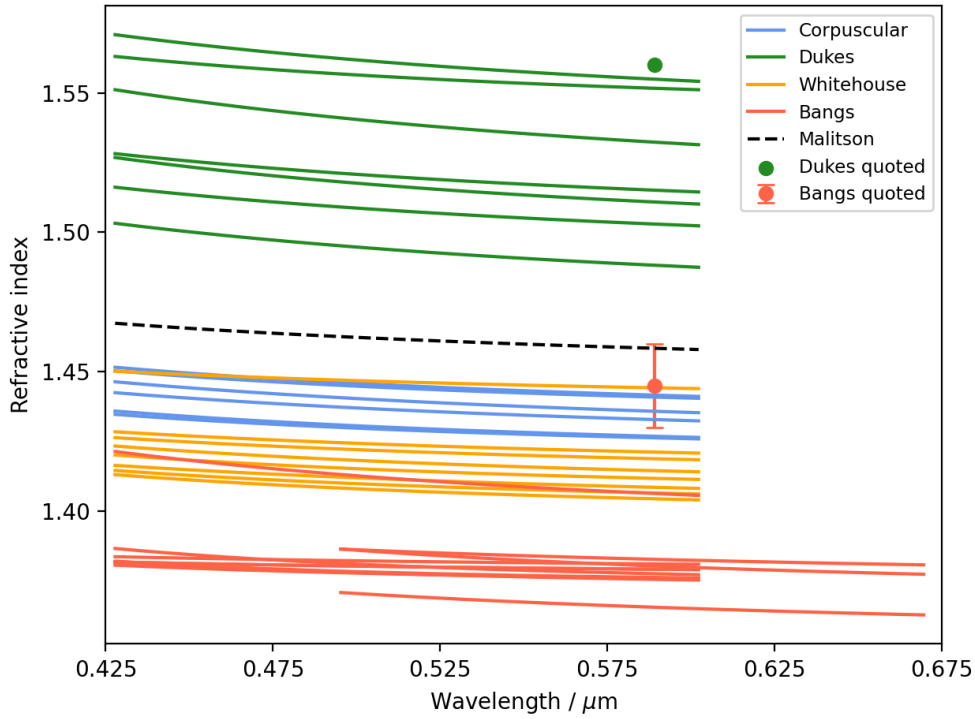

Figure 2: Cauchy curves showing the wavelength-dependent refractive index of all beads studied, compared with results from Malitsons study on bulk silica (dashed).

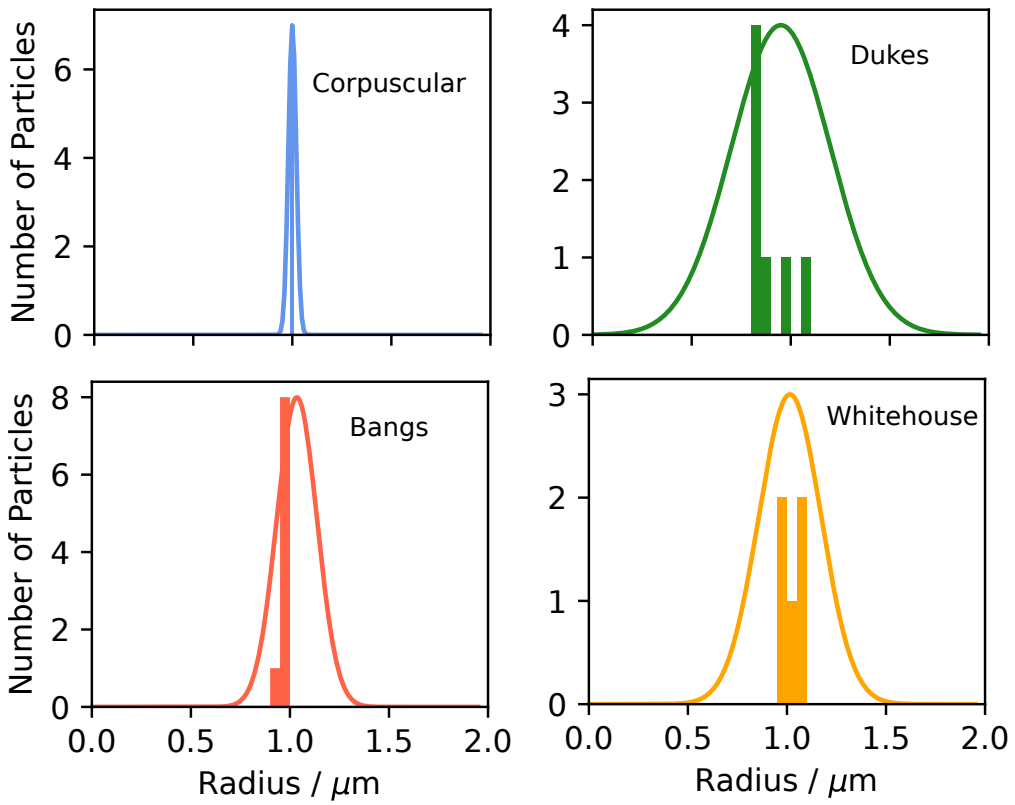

Figure 3: Determined radius distribution of all beads studied plotted as bar graphs. The bin widths for the Dukes, Bangs and Whitehouse samples are 50 nm, and the bin width for the Corpuscular sample is 20 nm. The manufacturers values of radius with associated uncertainties are plotted as Gaussian curves for comparison.

4. Discussion

The radius of the beads in the all samples were found to be within the quoted radius range given by the manufacturers, with Dukes having the largest and Corpuscular having the narrowest distribution of size, both in the quoted values and in the values determined from the samples in this study.

The average refractive index of the Dukes and Bangs samples were both slightly lower than their quoted values of refractive index (by 0.041 and 0.068 respectively). The Dukes and Bangs samples were also found to have a larger distribution of refractive indices across the sample than the Corpuscular and

Whitehouse samples. Although this study was not exhaustive as only a small number of beads from each sample were tested, the variance in values of refractive index determined for all beads show that the value of refractive index for bulk silica can not be correctly assumed for all silica beads produced by the Stöber process or iterations thereof. Silica beads should therefore be used with caution in situations where the an accurate refractive index is required, for example, in atmospheric experiments. If it is necessary to determine the refractive index of the specific silica bead being used in each atmospheric experiment, as it has been demonstrated here that the refractive index can vary significantly, even within the same sample.

The reliability of the refractive index and radius values of four suppliers of silica beads have been tested. Based on this study, Corpuscular beads have the smallest variance in values of both size and refractive index. The Corpuscular sample beads were also found to have the closest refractive index to that of bulk silica (~ 1.45), therefore being the ideal choice for atmospheric aerosol experiments, from the samples considered.

4.1. Atmospheric implication

Nephelometers are often used in atmospheric science to study the number density and other properties of atmospheric aerosol, such as radius, using their light scattering. They are calibrated with a test aerosol of known optical properties, such as polystyrene Manfred et al. (2018) or silica particles (Greswell et al., 2010). The maximum refractive index reported for the silica particles studied was 1.46 and the minimum determined refractive index of the beads was 1.35, a difference of 0.11. To calculate the impact an error of 0.11 in refractive index would produce on the size determined by a nephelometer the particle radii were log-normally distributed with a geometric mean standard deviation of 1.25, around a median radii of 0.1, 1 and 10 µm, and the back-scattering efficiency Bohren and Huffman (2008) of these distributions was calculated as a function of wavelength $425-600\,\mathrm{nm}$ with a reflective index of 1.46 using Philip Lavens Mieplot Philip Laven (2021). The calculated back-scattering coefficient variation with wavelength was then fitted with another Mie calculation assuming a refractive index of 1.35 and varying the median radii. It was found that an error in refractive index of 0.11 could lead to an error in radius of $0.006\,\mu\mathrm{m}$ (6%) for a particle distribution with a median radius of $0.1\,\mu\mathrm{m}$, $0.14\,\mu\mathrm{m}$ (14%) for a distribution with a median radius $1\,\mu\mathrm{m}$, and $2\,\mu\mathrm{m}$ (20%) for a distribution with a median radius $10\,\mu\mathrm{m}$.

5. Conclusion

The technique used in this work is shown to be an excellent method of determining the size and wavelength dependent refractive index of airborne particles at a high precision.

It has been shown that silica beads from different suppliers, and even beads within the same sample can have a large variance in refractive index, indicating that silica beads produced by the Stöber process do not all have the same refractive index as that of bulk silica, and great care should be taken before assuming the refractive index of silica beads, for calibration or experimental purposes.

It is also been shown that many available silica beads are not necessarily appropriate for atmospheric work. Based on the limited samples studied here, Corpuscular beads are recommended for atmospheric studies, as they have the closest refractive index to that of atmospheric silica particles.

Acknowledgements

We wish to acknowledge the support of NERC for funding of grants NE/R012148/1 and NE/T00732X/1. We are also grateful to STFC for support under grant 18130025, and for for access to the laboratories of the Central Laser Facility at the Research Complex at Harwell.

Supplementary data

All experimental data from this article can be found online at DOI 10.5281/zenodo.4893321.

Appendix A. Sample Appendix Section

References

Alois, S., Merrison, J., Iversen, J.J., Sesterhenn, J., 2017. Contact electrification in aerosolized monodispersed silica microspheres quantified using laser based velocimetry. Journal of Aerosol Science 106, 1–10.

Beganskiene, A., Sirutkaitis, V., Kurtinaitiene, M., Juskenas, R., Kareiva, A., 2004. FTIR, TEM and NMR Iinvestigations of Stöber Silica Nanoparticles. Materials science 10, 1392–1320.

Bohannon, K.P., Holz, R.W., Axelrod, D., 2017. Refractive Index Imaging of Cells with Variable-Angle Near-Total Internal Reflection (TIR) Microscopy. Microscopy and Microanalysis 23, 978–988.

Bohren, C.F., Huffman, D.R., 2008. Absorption and Scattering of Light by Small Particles. Wiley Science Paperback Series. new edition ed., Wiley-VCH.

Chen, S.L., Yuan, G., Hu, C.T., 2011. Preparation and size determination of monodisperse silica microspheres for particle size certified reference materials. Powder technology .

David, G., Esat, K., Hartweg, S., Cremer, J., Chasovskikh, E., Signorell, R., 2015. Stability of aerosol droplets in Bessel beam optical traps under constant and pulsed external forces. The Journal of Chemical Physics 142, 154506.

Demir, A., Serpengüzel, A., 2005. Silica microspheres for biomolecular detection applications. IEE Proceedings - Nanobiotechnology 152, 105–108.

Foladori, P., Quaranta, A., Ziglio, G., 2008. Use of silica microspheres having refractive index similar to bacteria for conversion of flow cytometric forward light scatter into biovolume. Water Research 42, 3757–3766.

Greswell, R.B., Rahman, S.H., Cuthbert, M.O., Tellam, J.H., 2010. An inexpensive flow-through laser nephelometer for the detection of natural colloids and manufactured nanoparticles. Journal of Hydrology 388, 112–120.

Jenkins, F.A., White, H.E., 2010. Fundamentals of optics. Mc Graw-Hill Primis Custom Publ., New York.

Jones, S.H., King, M.D., Ward, A.D., 2013. Determining the unique refractive index properties of solid polystyrene aerosol using broadband Mie scattering from optically trapped beads. Physical Chemistry Chemical Physics 15, 20735–20741.

Jones, S.H., King, M.D., Ward, A.D., 2015. Atmospherically relevant core-shell aerosol studied using optical trapping and Mie scattering. Chem. Commun. 51, 4914–4917. Publisher: The Royal Society of Chemistry.

Khlebtsov, B.N., Khanadeev, V.A., Khlebtsov, N.G., 2008. Determination of the Size, Concentration, and Refractive Index of Silica Nanoparticles from Turbidity Spectra. Langmuir 24, 8964–8970. doi:10.1021/la8010053. publisher: American Chemical Society.

Malitson, I.H., 1965. Interspecimen Comparison of the Refractive Index of Fused Silica*,†. JOSA 55, 1205–1209. Publisher: Optical Society of America.

Manfred, K.M., Washenfelder, R.A., Wagner, N.L., Adler, G., Erdesz, F., Womack, C.C., Lamb, K.D., Schwarz, J.P., Franchin, A., Selimovic, V., al, e., 2018. Investigating biomass burning aerosol morphology using a laser imaging nephelometer. Atmospheric Chemistry and Physics 18, 1879–1894.

McGrory, M.R., King, M.D., Ward, A.D., 2020. Using Mie Scattering to Determine the Wavelength-Dependent Refractive Index of Polystyrene Beads with Changing Temperature. The Journal of Physical Chemistry A 124, 9617–9625. Publisher: American Chemical Society.

Panagiotaki, K.N., Spyrou, K., Zachariadis, M., Pratsinis, H., Kouloumpis, A., Boutsika, L.G., Enotiadis, A., Gournis, D., Giannelis, E.P., Sideratou, Z., 2020. Non-porous phosphonated ionic silica nanospheres as nanocarriers for efficient intracellular delivery of doxorubicin. Materials Today Communications 23, 100787.

Parida, B.K., Garrastazu, H., Aden, J.K., Cap, A.P., McFaul, S.J., 2015. Silica microspheres are superior to polystyrene for microvesicle analysis by flow cytometry. Thrombosis Research 135, 1000–1006.

Philip Laven, 2021. MiePlot.

Preston, T.C., Mason, B.J., Reid, J.P., Luckhaus, D., Signorell, R., 2014. Size-dependent position of a single aerosol droplet in a Bessel beam trap. Journal of Optics 16, 025702.

Scientific Committee on Consumer Safety, 2015. Silica, Hydrated Silica, and Silica Surface Modified with Alkyl Silylates (nano form). doi:10.2772/52532.

Serway, R.A., Faughn, J.S., Vuille, C., 2011. College Physics, 9th Edition. 9 ed., Charles Hartford.

Shepherd, R.H., King, M.D., Marks, A., Brough, N., Ward, A.D., 2017. Determination of the refractive index of insoluble organic extracts from atmospheric aerosol over the visible wavelength range using optical tweezers. Atmospheric Chemistry and Physics Discussions 2017, 1–25.

Stöber, W., Fink, A., Bohn, E., 1968. Controlled growth of monodisperse silica spheres in the micron size range. Journal of Colloid and Interface Science 26, 62–69.

Tamar, Y., Tzabari, M., Haspel, C., Sasson, Y., 2014. Estimation of the porosity and refractive index of sol–gel silica films using high resolution electron microscopy. Solar Energy Materials and Solar Cells 130, 246–256.

Thanopulos, I., Luckhaus, D., Preston, T.C., Signorell, R., 2014. Dynamics of submicron aerosol droplets in a robust optical trap formed by multiple Bessel beams. Journal of Applied Physics 115, 154304.

Thomas, I.M., 1992. Method for the preparation of porous silica antireflection coatings varying in refractive index from 1.22 to 1.44. Applied Optics 31, 6145–6149. Publisher: Optical Society of America.

Unger, K.K., Jilge, O., Kinkel, J.N., Hearn, M.T.W., 1986. Evaluation of advanced silica packings for the separation of biopolymers by high-performance liquid chromatography II. Performance of non-porous monodisperse 1.5-microm Silica beads in the separation of proteins by reversed-phase gradient elution high-performance liquid chromatography. Journal of Chromatography A 359, 61–72.

Chapter 5

Atmospheric photo-oxidation of core-shell particles

Megan R. McGrory, Martin D. King and Andrew D. Ward

Publication status: To be submitted for publication in the Journal of the American Chemical Society

I declare I have made the following contributions to the piece of co-authored work:

- Conducted the experiments, and analysed all data collected
- Contributed to the conclusions drawn from the experiments conducted
- Wrote the first draft and, upon feedback from co-authors, completed all revisions of the paper

Atmospheric organic matter forms core-shell aerosol particles on mineral surfaces

Megan R. McGrory,[†,‡] Andrew D. Ward,[†] and Martin D. King[*,‡]

†*STFC, Central Laser Facility, Research Complex at Harwell, Rutherford Appleton Laboratory, Harwell Oxford, Didcot, Oxfordshire, OX11 0FA, UK*

‡*Department of Earth Sciences, Royal Holloway University of London, Egham, Surrey, TW20 0EX, UK*

E-mail: m.king@rhul.ac.uk

Abstract

Two-phase particles have been created by depositing thin films ($\sim 10-40$ nm) of aged urban and domestic wood-burning aerosol samples onto optically trapped mineral silica particles (diameter $\sim$2 µm). They were shown to have core-shell morphology where the Mie scattering of light from the optically trapped particles was consistent with the scattering of light by core-shell aerosol, and not with the scattering of homogeneous or partially-engulfed aerosol. The work is a first demonstration of organic materials extracted from the atmosphere favouring a core-shell morphology on solid particles. The particles were also shown to maintain a core-shell morphology during oxidation with gas-phase ozone, an atmospheric oxidant.

The refractive indices and film thicknesses were calculated by reproducing Mie scattered light as a function of wavelength. The refractive index of $\sim$40 nm thick shells were determined to a precision of $\sim$0.01 and $\sim$0.006, and the thickness of the shell was determined to a precision of 0.2 nm and 0.1 nm for the aged urban and wood-smoke samples respectively, throughout the oxidation process. Wood-smoke and aged urban

aerosol deposited onto solid aerosol can be assumed to form a core-shell morphology, significantly reducing the complexity of atmospheric modelling of the radiative properties of these aerosol.

Atmospheric aerosol significantly impacts the Earth's climate both indirectly and directly through forming cloud condensation nuclei, and scattering light entering the Earth's atmosphere, respectively [eg. 1]. However, the impact of atmospheric aerosol remains the least well quantified factor affecting the Earth's climate[2]. The refractive index, size, and morphology of aerosol particles are key factors for determining the interactions of atmospheric aerosol with light [eg. 3]. There are many different compositions and proposed morphologies of aerosol particles produced by both natural and anthropogenic sources, as well as secondary organic aerosol produced by reactions in the atmosphere [eg. 4].

Most calculations of atmospheric light scattering in atmospheric and climate modelling assume spherical homogeneous particles [eg. 5]. However, recent work has suggested that many particles have at least two immiscible phases which can adopt several potential morphologies with very different light scattering properties, and thus radiative forcings[6–10]. Two of the most common morphologies for two-phase particles are partially-engulfed[9,11–15] and core-shell[10,16–25]. Mie scattering modelling studies on core-shell[16,17], and thermodynamic modelling of partially-engulfed[11] particles predict how the scattering of light by core-shell particles differs from that of homogeneous spheres. There have been a number of experimental studies with chemically pure compounds which have shown the formation of both core-shell[10,18–25] and partially-engulfed[9,11–15] morphologies. Studies using pure chemical components or oxidation of a pure compound have also shown organic-inorganic two phase particles to form both core-shell and partially-engulfed morphologies depending on the organic-to-inorganic mixing ratios[26,27] and relative humidity[7].

To the authors knowledge the typical morphology adopted by material found in atmospheric aerosol, which is a complex mixture and not well represented by a simple pure chemical, hasn't been shown. In this work it is demonstrated for the first time that or-

ganic material extracted from ambient atmospheric aerosol forms core-shell morphology on spherical (core) silica airborne particles. Micron-sized silica beads are used as a proxy for mineral aerosol readily present in the atmosphere[2,28]. It is also shown that if a thick enough shell is formed (> 10 nm) the particle will maintain a core-shell structure during subsequent oxidation with gas-phase ozone, a common atmospheric oxidant. The core-shell morphology (even during oxidation) allows atmospheric modellers a significant reduction in the complexity of their models. To our knowledge this is the first demonstration of the morphology of two-phase aerosol with atmospheric matter, as opposed to experiments with pure chemicals.

Atmospheric aerosol was collected on quartz fibre filters (Whatman QM-A) from ambient urban air in greater London as described by Jones *et al.*[29], and from domestic wood burning of air-dried wild cherry tree in a domestic metal burner, using the same method[29,30]. The organic components on the filters were extracted into chloroform and transferred to propan-1-ol for delivery to the experiment. Propan-1-ol was chosen as the carrier solvent because it dissolves the material of interest easily, nebulises to produce a short-lived mist, and evaporates readily, as shown previously[30].

The samples were deposited onto optically trapped *eg.* [31–39] spherical silica beads, which were delivered into the trapping cell using a Topas ATM 220 atomizer. As optical trapping is a contact-less method, it allows the particle to be studied without disturbing the particle morphology in any way. The optical set-up used for this study has been described in detail previously[32,40].

Organic material extracted from wood-smoke was introduced to the silica bead using a different method to the aged urban sample. Using two different methods of thin layer formation shows a robustness to the technique used and gives confidence in the results obtained. The aged urban aerosol was deposited onto the trapped silica bead using a nebuliser (the wood-smoke sample was too viscous to nebulised). Extracted wood-smoke particles were produced by blowing dry N_2 gas over the sample at 150 °C and through a cooled metal tube (15 °C) to form aerosol which subsequently collided with the silica bead. This is similar

to the method used previously for producing core-shell oleic acid on silica particles[41]. Mild temperatures of 150 °C were deemed not to damage samples produced in hotter environments (fire), where as the same method may degrade the aged urban sample. Collisions between the silica bead and the organic samples were monitored by continuously recording the intensity of back-scatted light as a function of wavelength between 425−600 nm (henceforth called Mie spectra) over 3 second intervals, using Mie spectroscopy. The organic sample was continually added for typically 2-3 collisions, and was held stable in the trap.

Once the two-phase particle was formed the opportunity for further exploration was taken and the two-phase particle was reacted with gas-phase ozone (18.3 or 8.5 ppm in oxygen) to simulate atmospheric oxidation, but with shorter reaction times[42]. Oxygen (O_2) was bubbled through water (H_2O), at ambient temperature, into a UV ozonizer, to produce ozone (O_3) at a relatively large mixing ratio of 18.3 ppm and 8.5 ppm for the wood-smoke and aged urban aerosol samples respectively. A large mixing ratio of ozone was used to ensure a reasonably rapid reaction as the oxidation experiments were initially exploratory and the main aim was to demonstrate core-shell morphology. Throughout the experiment the particles were illuminated by a 6 V Comar 555 LED white light source. The output of the LED light is shown in Figure S6 in the supplementary information. For all particles studied, no reaction was observed until the ozone was introduced, meaning it is unlikely any significant photochemical oxidation took place within the trapping cell.

Mie resonances (peaks in the Mie spectrum) will be much sharper and more prominent if a particle is spherically symmetrical[43]. If a particle looses spherical symmetry Mie resonances will become significantly weaker and almost or completely disappear[43,44]. For both samples studied, when the sample was deposited onto the silica core the Mie resonances did not become weaker or broader, demonstrating that the particle maintained spherical symmetry. If a partially-engulfed particle was formed it would no longer be spherically symmetrical and the peaks would have become significantly weaker and broader[43,44]. Thus, from initial inspection of the Mie spectra the two-phase particles were consistent with a core-shell mor-

phology. To further confirm the core-shell morphology the experimental Mie spectra were reproduced with calculated Mie spectra from core-shell theory[45] and were found not to be consistent with homogeneous[46] Mie theory.

The real component of the refractive index and the thickness of the shell were both determined throughout the oxidation process. Three core-shell particles were created and studied from each atmospheric sample. It was possible to determine the wavelength-dependent refractive index and the thickness of the shell simultaneously from the core-shell spectra by matching the Mie resonances in the experimental Mie spectra produced by the scattering of visible light from the aerosol particle, to the Mie resonances in the theoretical calculated spectra of known refractive index and size. The theoretical spectra were generated using a model[46,47] based on Aden and Kerker's formalism of scattering by core-shell particles[45].

The refractive index and radius of the core silica particle were readily determined from a Mie spectrum of the silica core, using the method described previously[40] for homogeneous spheres, before the addition of organic material. The parameters of the silica core where then fixed in the generation of the calculated core-shell spectra, and the refractive index and thickness of the shell were varied to find the best fit for these parameters. All Mie spectra collected are available online at DOI: 10.5281/zenodo.5082022.

It was found that fitting of core-shell Mie spectra were much more sensitive to shell thickness than refractive index, particularly for thinner films. The film thickness was able to be determined to within 1 nm for any film thickness. However, for refractive index much greater variation was found (~ 0.2) for thin films approaching 1 nm. Therefore the refractive index determined for thick films ($\sim$40 nm) of the same sample were assumed when fitting the thinner films of thickness $<$10 nm. This behaviour is demonstrated in Figure S5 in the supplementary information.

As shown in Figure 1, the Mie scattering of both propan-1-ol/wood smoke on silica, and propan-1-ol/aged urban aerosol on silica particles is consistent with core-shell aerosol scattering. The authors may be bold enough to suggest that as a first approximation both

wood-smoke and aged urban aerosol deposited on mineral aerosol may be modelled as a core-shell with some confidence as shown by this study.

The aged urban aerosol shell was found to react when exposed to ozone which may be in contrast to a previous study[29] where similar aerosol samples from the same location were found to be unreactive to ozone when placed at the air-water interface. There are two possible explanations fro this discrepancy. The samples were collected at a different time to the previous study and are chemically different[30], or this may suggest of the unsaturated organic not being stable at the air-water interface, a very different interface to the air-mineral interface studied here.

Aged urban aerosol core-shell particles with thick films ($\sim$ 30–40 nm) were able to maintain core-shell morphology during oxidation. In the case where a thin film of 10 nm was formed, upon oxidation the shell was completely removed, within the precision of this experiment (<1 nm), leaving the silica core only as shown in Figure 2. The complete removal of the film and the Mie spectrum returning to that of the silica bead provides conformation that the silica core remains after deposition and removal of a film, countering one possible scenario that the silica bead was ejected by a similar sized organic droplet. Further confirmation was that fitting these spectra with the homogeneous model gave an approximately four times statistically worse fit than when using the core-shell model.

Thicker films were not completely removed from the two-phase urban aerosol particles, as demonstrated in Figures S2 and S3 in the supplementary information. Oxidation of aged urban aerosol films did not appear to markedly change the refractive index of the shell but thin films are removed and thick films loose substantial amount of material but were not removed completely. Figure 3 shows how the shell thickness and refractive index changed with oxidation for three aged urban aerosol, silica core-shell particle. As the films are a complex mixture of compounds, when oxidised the gas-phase ozone will preferentially react with and remove species with carbon-carbon double bonds and not react with saturated organic species. In the thin film; after reaction of all carbon-carbon double bonds with

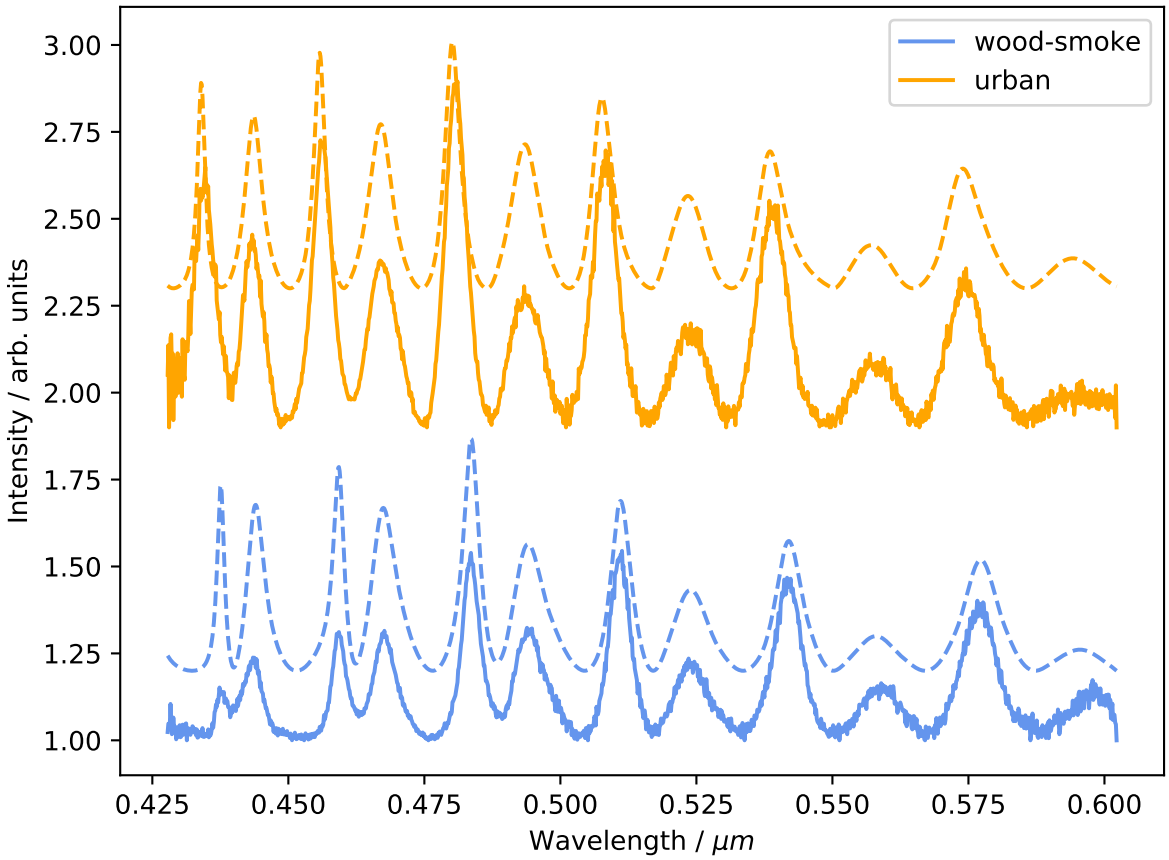

Figure 1: Typical experimental Mie spectra for two-phase particles created using the aged urban and wood-smoke aerosol samples. The dashed spectra show the corresponding theoretical fit for both spectra generated using core-shell theory[45,47]. The top two spectra are urban aerosol on a silica core (of radius 0.999 µm and refractive index parameters; A = 1.4402, B = 0.00363 and C = 1.875e-7). The core-shell experimental spectrum (solid) is compared with its corresponding calculated spectrum (dashed). The shell thickness was calculated as 40 nm and the refractive index parameters of the shell were calculated as A = 1.417, B = 0.017 and C = 0. The bottom two spectra are wood-smoke aerosol on a silica core (of radius 1.0 µm and refractive index parameters; A = 1.4234, B = 0.00365 and C = 6.46e-5). The core-shell experimental spectrum (solid) is compared with its corresponding calculated spectrum (dashed). The shell thickness was calculated as 41 nm and the refractive index parameters of the shell were calculated as A = 1.420, B = 0.015 and C = 0.

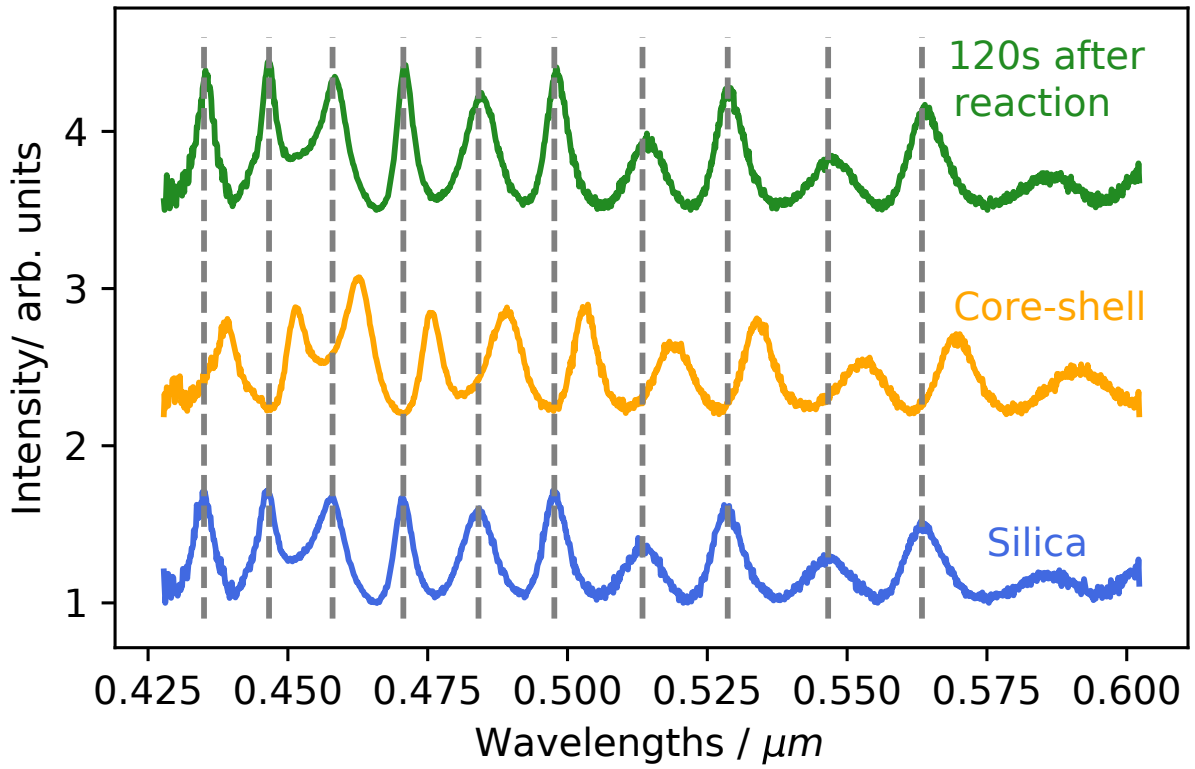

Figure 2: Mie spectra of silica core (blue), silica/urban aerosol core-shell particle 1 before reaction (gold) and 120s after reaction (green), demonstrating that a thin film of 10 nm was formed and removed, leaving the silica core only. The grey dashed vertical lines are to demonstrate the bare silica and the oxidised core-shell particle have the same Mie resonances.

ozone any remaining film of saturated organic compounds may be below the detection limit (>1 nm) However, a product film remaining detectable after oxidation of the thick films suggests the reduction of unsaturated material with remaining saturated material remaining observable.

Multiple collisions of wood smoke aerosol were needed to generate a core-shell particle. After each collision there is a sudden increase in radius followed by a slower decay owing, presumably, to the loss of volatile components from the organic mixture. After each collision the decrease in the rate of loss of radius slows relative to the previous collision. A simple explanation of this may be that as the mixture is forming the film becomes more concentrated in heavier molecular weight components as the lighter ones may evaporate more readily. The loss of propan-1-ol was assumed to be rapid compared with loss of smoke components[30]. After

4-5 collisions a thicker film (∼40 nm) was formed, and was consequently richer in less volatile components. Figure S1 in the supplementary information demonstrates this behaviour.

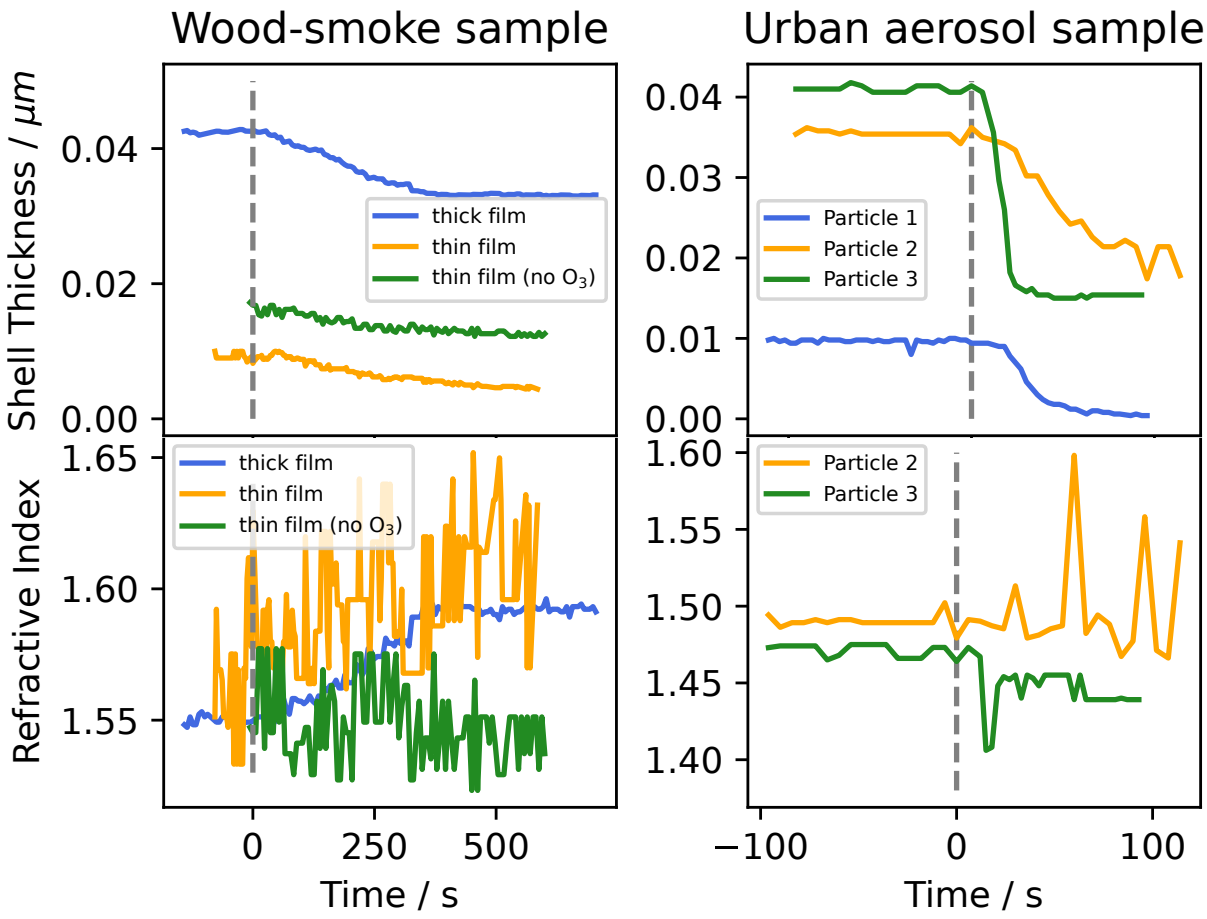

Figure 3: The left panels show how the refractive index (at 598 nm) and the shell thickness of the wood-smoke sample changed upon reaction with ozone. The right panels show the change in refractive index (at 598 nm) and shell thickness of the urban aerosol sample upon reaction with ozone. The grey dashed lines represent the point where the reaction started. The refractive indices of the shells were determined to a precision of 0.00967 and 0.0063 and the thickness of the shell was determined to a precision of 0.2 nm and 0.1 nm for the aged urban and wood-smoke samples respectively, throughout the oxidation process. The average refractive index determined for the two thick films (∼40 nm) of the urban sample were assumed when fitting the thin film with thickness <10 nm.

The core-shell of silica and wood-smoke particle with a relatively thick thin film (∼40 nm) was found to be a stable core-sell morphology for over 500 seconds before it was exposed to ozone. Figure 3 shows the oxidation of a thin film and the change in a thin film when no O_3 is present. Unlike the urban aerosol film on silica, the refractive index of wood-smoke

film did change upon oxidation. The wavelength-dependent refractive indices of all organic thin films studied were in broad agreement with the determined refractive indices of similar samples of homogeneous spheres collected in previous work[30], as shown in Figure 4, giving confidence to this method.

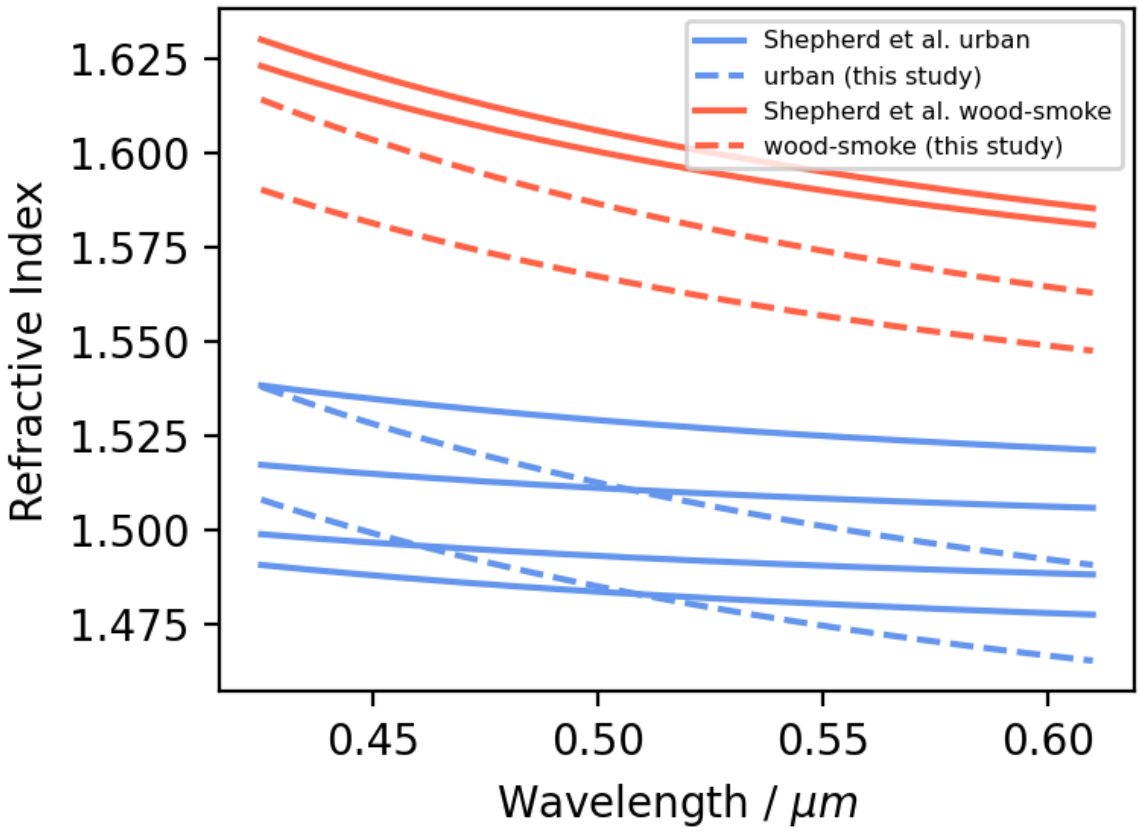

Figure 4: Cauchy curves showing the wavelength-dependent refractive index of the organic samples used in this study compared with the determined refractive index of similar samples used in previous work[30].

Gorkowski *et al.*[7] used optical trapping and Raman spectroscopy to study the morphology of phase separated laboratory generated $\alpha-$pinene secondary organic aerosol at varying relative humidities. Their results combined with literature values of oxidation of phase separated secondary organic aerosol predicted that as oxidation of the material in an aerosol is increased the particles move from partially-engulfed, to core-shell, to homogeneous. This

study has shown that material extracted from the atmosphere also forms core-shell morphologies, like the proxy laboratory materials and that during oxidation on a solid core maintains the core-shell morphology.

It has been demonstrated here that organic materials extracted from atmospheric aerosol form stable core-shell particles with mineral aerosol, and can retain this morphology during oxidation. It has also been shown that optical trapping can be used to study core-shell aerosol with real atmospheric matter. The results in these studies suggest mineral aerosol with organic material can be modelled as mineral core with a thin coating.

Acknowledgement

We wish to acknowledge the support of NERC for funding of grants NE/R012148/1 and NE/T00732X/1. We are also grateful to STFC for support under grant 18130025, and for access to the laboratories of the Central Laser Facility at the Research Complex at Harwell.

Available data

All raw data is published online at DOI: 10.5281/zenodo.5082022.

References

(1) J. Seinfeld, S. P. *Atmospheric Chemistry and Physics*; Wiley, 2016; Vol. 3.

(2) IPCC, *Climate Change 2013: The Physical Science Basis. Contribution of Working Group I to the Fifth Assessment Report of the Intergovernmental Panel on Climate Change*; Cambridge University Press, Cambridge, United Kingdom and New York, NY, USA, 2013.

(3) Haywood, J. M.; Ramaswamy, V.; Soden, B. J. Tropospheric Aerosol Climate Forcing in Clear-Sky Satellite Observations over the Oceans. *Science* **1999**, *283*, 1299–1303.

(4) Jacobson, M. C.; Hansson, H.-C.; Noone, K. J.; Charlson, R. J. Organic atmospheric aerosols: Review and state of the science. *Reviews of Geophysics* **2000**, *38*, 267–294.

(5) Kanakidou, M. et al. Organic aerosol and global climate modelling: a review. *Atmospheric Chemistry and Physics* **2005**, *5*, 1053–1123.

(6) Zhang, R.; Khalizov, A. F.; Pagels, J.; Zhang, D.; Xue, H.; McMurry, P. H. Variability in morphology, hygroscopicity, and optical properties of soot aerosols during atmospheric processing. *Proceedings of the National Academy of Sciences* **2008**, *105*, 10291–10296.

(7) Gorkowski, K.; Donahue, N. M.; Sullivan, R. C. Aerosol Optical Tweezers Constrain the Morphology Evolution of Liquid-Liquid Phase-Separated Atmospheric Particles. *Chem* **2020**, *6*, 204–220.

(8) Xiong, C.; Friedlander, S. K. Morphological properties of atmospheric aerosol aggregates. *Proceedings of the National Academy of Sciences* **2001**, *98*, 11851–11856.

(9) Veghte, D. P.; Altaf, M. B.; Freedman, M. A. Size Dependence of the Structure of Organic Aerosol. *Journal of the American Chemical Society* **2013**, *135*, 16046–16049.

(10) Cheng, T.; Wu, Y.; Chen, H. Effects of morphology on the radiative properties of internally mixed light absorbing carbon aerosols with different aging status. *Optics Express* **2014**, *22*, 15904–15917.

(11) Qiu, Y.; Molinero, V. Morphology of LiquidLiquid Phase Separated Aerosols. *Journal of the American Chemical Society* **2015**, *137*, 10642–10651.

(12) Laskina, O.; Morris, H. S.; Grandquist, J. R.; Qin, Z.; Stone, E. A.; Tivanski, A. V.; Grassian, V. H. Size Matters in the Water Uptake and Hygroscopic Growth of Atmo-

spherically Relevant Multicomponent Aerosol Particles. *The Journal of Physical Chemistry A* **2015**, *119*, 4489–4497.

(13) Reid, J. P.; Dennis-Smither, B. J.; Kwamena, N.-O. A.; Miles, R. E. H.; Hanford, K. L.; Homer, C. J. The morphology of aerosol particles consisting of hydrophobic and hydrophilic phases: hydrocarbons, alcohols and fatty acids as the hydrophobic component. *Phys. Chem. Chem. Phys.* **2011**, *13*, 15559–15572.

(14) Mitchem, L.; P. Reid, J. Optical manipulation and characterisation of aerosol particles using a single-beam gradient force optical trap. *Chemical Society Reviews* **2008**, *37*, 756–769.

(15) Dennis-Smither, B. J.; Hanford, K. L.; Kwamena, N.-O. A.; Miles, R. E. H.; Reid, J. P. Phase, Morphology, and Hygroscopicity of Mixed Oleic Acid/Sodium Chloride/Water Aerosol Particles before and after Ozonolysis. *The Journal of Physical Chemistry A* **2012**, *116*, 6159–6168.

(16) Ray, A. K.; Nandakumar, R. Simultaneous determination of size and wavelength-dependent refractive indices of thin-layered droplets from optical resonances. *Applied Optics* **1995**, *34*, 7759–7770.

(17) Huckaby, J. L.; Ray, A. K. Layer Formation on Microdroplets: A Study Based on Resonant Light Scattering. *Langmuir* **1995**, *11*, 80–86.

(18) Garland, E. R.; Lee, A. D.; Baer, T.; Clarke, L. I. Growth Dynamics and Morphology of Oleic Acid Vapor-Deposited on a Silica Surface. *The Journal of Physical Chemistry C* **2009**, *113*, 2141–2148.

(19) Kaiser, T.; Roll, G.; Schweiger, G. Investigation of coated droplets in an optical trap: Raman-scattering, elastic-light-scattering, and evaporation characteristics. *Applied Optics* **1996**, *35*, 5918–5924.

(20) Li, W.; Rassat, S. D.; Foss, W. R.; Davis, E. J. Formation and Properties of Aerocolloidal TiO2-Coated Microspheres Produced by Alkoxide Droplet Reaction. *Journal of Colloid and Interface Science* **1994**, *162*, 267–278.

(21) Abo Riziq, A.; Trainic, M.; Erlick, C.; Segre, E.; Rudich, Y. Extinction efficiencies of coated absorbing aerosols measured by cavity ring down aerosol spectrometry. *Atmospheric Chemistry and Physics* **2008**, *8*, 1823–1833.

(22) Katrib, Y.; Martin, S. T.; Hung, H.-M.; Rudich, Y.; Zhang, H.; Slowik, J. G.; Davidovits, P.; Jayne, J. T.; Worsnop, D. R. Products and Mechanisms of Ozone Reactions with Oleic Acid for Aerosol Particles Having CoreShell Morphologies. *The Journal of Physical Chemistry A* **2004**, *108*, 6686–6695.

(23) Wang, X.; Meng, X.; Wang, Y.; Cao, Y. Simulation of the Optical and Thermal Properties of Multiple CoreShell Atmospheric Fractal Soot Agglomerates under Visible Solar Radiation. *The Journal of Physical Chemistry C* **2019**, *123*, 24225–24233.

(24) Jones, S. H.; King, M. D.; Ward, A. D. The study of thin films on solid aerosol particles using optical trapping and Mie scattering from a broadband white LED. Optical Trapping and Optical Micromanipulation XI. 2014; p 91641X.

(25) King, M. D.; Thompson, K. C.; Ward, A. D. Laser Tweezers Raman Study of Optically Trapped Aerosol Droplets of Seawater and Oleic Acid Reacting with Ozone: Implications for Cloud-Droplet Properties. *Journal of the American Chemical Society* **2004**, *126*, 16710–16711.

(26) Song, M.; Marcolli, C.; K. Krieger, U.; M. Lienhard, D.; Peter, T. Morphologies of mixed organic/inorganic/aqueous aerosol droplets. *Faraday Discussions* **2013**, *165*, 289–316.

(27) Buajarern, J.; Mitchem, L.; Reid, J. P. Characterizing Multiphase Organic/Inorganic/Aqueous Aerosol Droplets. *The Journal of Physical Chemistry A* **2007**, *111*, 9054–9061.

(28) Betzer, P. R.; Carder, K. L.; Duce, R. A.; Merrill, J. T.; Tindale, N. W.; Uematsu, M.; Costello, D. K.; Young, R. W.; Feely, R. A.; Breland, J. A.; Bernstein, R. E.; Greco, A. M. Longrange transport of giant mineral aerosol particles. *Nature* **1988**, *336*, 568–571.

(29) Jones, S. H.; King, M. D.; Ward, A. D.; Rennie, A. R.; Jones, A. C.; Arnold, T. Are organic films from atmospheric aerosol and sea water inert to oxidation by ozone at the air-water interface? *Atmospheric Environment* **2017**, *161*, 274–287.

(30) Shepherd, R. H.; King, M. D.; Marks, A.; Brough, N.; Ward, A. D. Determination of the refractive index of insoluble organic extracts from atmospheric aerosol over the visible wavelength range using optical tweezers. *Atmospheric Chemistry and Physics Discussions* **2017**, *2017*, 1–25.

(31) Ashkin, A.; Dziedzic, J. M.; Yamane, T. Optical trapping and manipulation of single cells using infrared laser beams. *Nature* **1987**, *330*, 769.

(32) H. Jones, S.; D. King, M.; D. Ward, A. Determining the unique refractive index properties of solid polystyrene aerosol using broadband Mie scattering from optically trapped beads. *Physical Chemistry Chemical Physics* **2013**, *15*, 20735–20741.

(33) Wills, J. B.; Knox, K. J.; Reid, J. P. Optical control and characterisation of aerosol. *Chemical Physics Letters* **2009**, *481*, 153–165.

(34) Ashkin, A. Optical trapping and manipulation of neutral particles using lasers. *Biological Sciences - Biophysics* **1997**, *94*, 4853–4860.

(35) Ashkin, A.; Dziedzic, J. M.; Bjorkholm, J. E.; Chu, S. Observation of a single-beam gradient force optical trap for dielectric particles. *Optics Letters* **1986**, *11*, 288–290.

(36) Preston, T. C.; Mason, B. J.; Reid, J. P.; Luckhaus, D.; Signorell, R. Size-dependent

position of a single aerosol droplet in a Bessel beam trap. *Journal of Optics* **2014**, *16*, 025702.

(37) Thanopulos, I.; Luckhaus, D.; Preston, T. C.; Signorell, R. Dynamics of submicron aerosol droplets in a robust optical trap formed by multiple Bessel beams. *Journal of Applied Physics* **2014**, *115*, 154304.

(38) David, G.; Esat, K.; Hartweg, S.; Cremer, J.; Chasovskikh, E.; Signorell, R. Stability of aerosol droplets in Bessel beam optical traps under constant and pulsed external forces. *The Journal of Chemical Physics* **2015**, *142*, 154506.

(39) Gorkowski, K.; Donahue, N. M.; Sullivan, R. C. Emerging investigator series: determination of biphasic coreshell droplet properties using aerosol optical tweezers. *Environmental Science: Processes & Impacts* **2018**, *20*, 1512–1523.

(40) McGrory, M. R.; King, M. D.; Ward, A. D. Using Mie Scattering to Determine the Wavelength-Dependent Refractive Index of Polystyrene Beads with Changing Temperature. *The Journal of Physical Chemistry A* **2020**, *124*, 9617–9625.

(41) Jones, S. H.; King, M. D.; Ward, A. D. Atmospherically relevant core-shell aerosol studied using optical trapping and Mie scattering. *Chem. Commun.* **2015**, *51*, 4914–4917.

(42) Herrmann, H. Kinetics of Aqueous Phase Reactions Relevant for Atmospheric Chemistry. *Chemical Reviews* **2003**, *103*, 4691–4716.

(43) Mishchenko, M. I.; Liu, L.; Mackowski, D. W. Morphology-dependent resonances of spherical droplets with numerous microscopic inclusions. *Optics Letters* **2014**, *39*, 1701–1704, Publisher: Optical Society of America.

(44) Gorkowski, K.; Donahue, N. M.; Sullivan, R. C. Emulsified and LiquidLiquid Phase-Separated States of -Pinene Secondary Organic Aerosol Determined Using Aerosol Op-

tical Tweezers. *Environmental Science & Technology* **2017**, *51*, 12154–12163, Publisher: American Chemical Society.

(45) Aden, A. L.; Kerker, M. Scattering of Electromagnetic Waves from Two Concentric Spheres. *Journal of Applied Physics* **1951**, *22*, 1242–1246.

(46) Bohren, C. F.; Huffman, D. R. *Absorption and Scattering of Light by Small Particles*, new edition ed.; Wiley Science Paperback Series; Wiley-VCH, 2008.

(47) Leinonen, J. Python code for calculating Mie scattering from single- and dual-layered spheres. 2016; `https://github.com/jleinonen/pymiecoated/`.

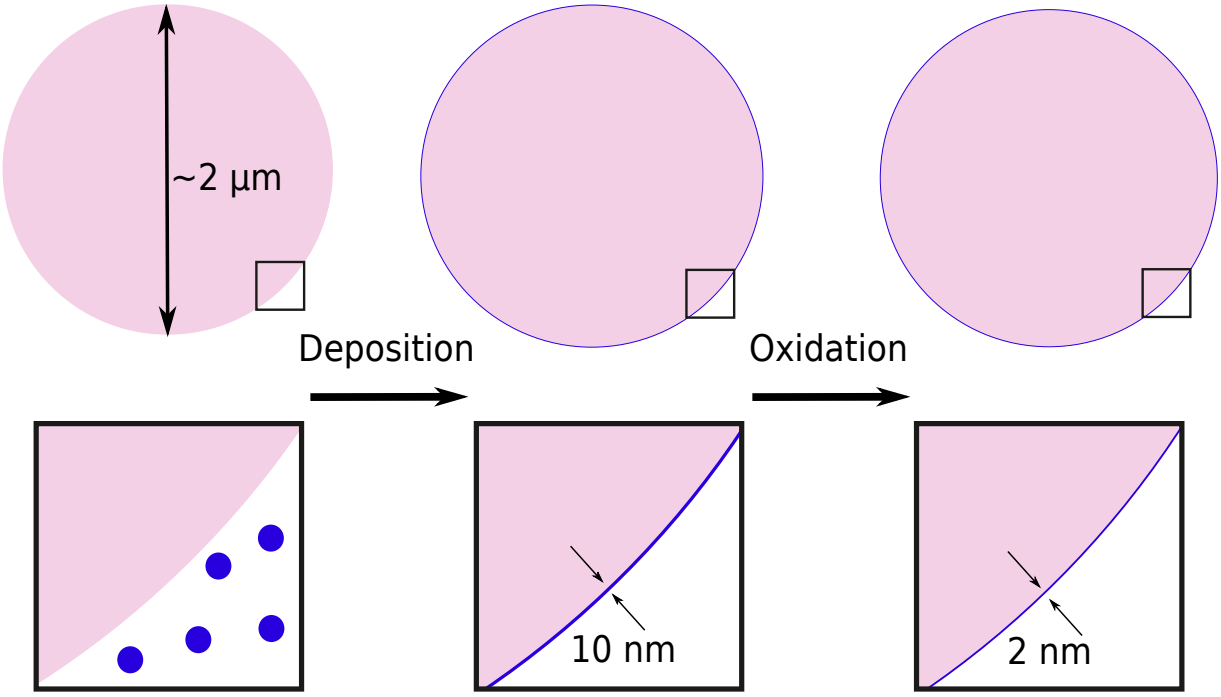

Figure 5: Table Of Contents Graphic

Supplementary information: Atmospheric organic matter may form core-shell aerosol particles on mineral surfaces

Megan R. McGrory,[†,‡] Andrew D. Ward,[†] and Martin D. King[*,‡]

†*STFC, Central Laser Facility, Research Complex at Harwell, Rutherford Appleton Laboratory, Harwell Oxford, Didcot, Oxfordshire, OX11 0FA, UK*

‡*Department of Earth Sciences, Royal Holloway University of London, Egham, Surrey, TW20 0EX, UK*

E-mail: m.king@rhul.ac.uk

Available data

All raw data is published online at DOI: 10.5281/zenodo.5082022.

Optical trapping of airbourne particles

The optical trap used in this experiment was able to trap and hold silica beads (Corpuscular) in a gas phase atmosphere while organic samples from the atmosphere where deposited onto their surface, and throughout the process of oxidation by gas-phase ozone.

A schematic of the equipment is shown in Figure S1 and consisted of a 1064 nm Nd:YAG laser (Laser Quantum) coupled to two single-mode fibre-optic cables via a beam-splitter coupling port (Oz Optics), delivering laser beams of power 10 mW and 15 mW (measured at

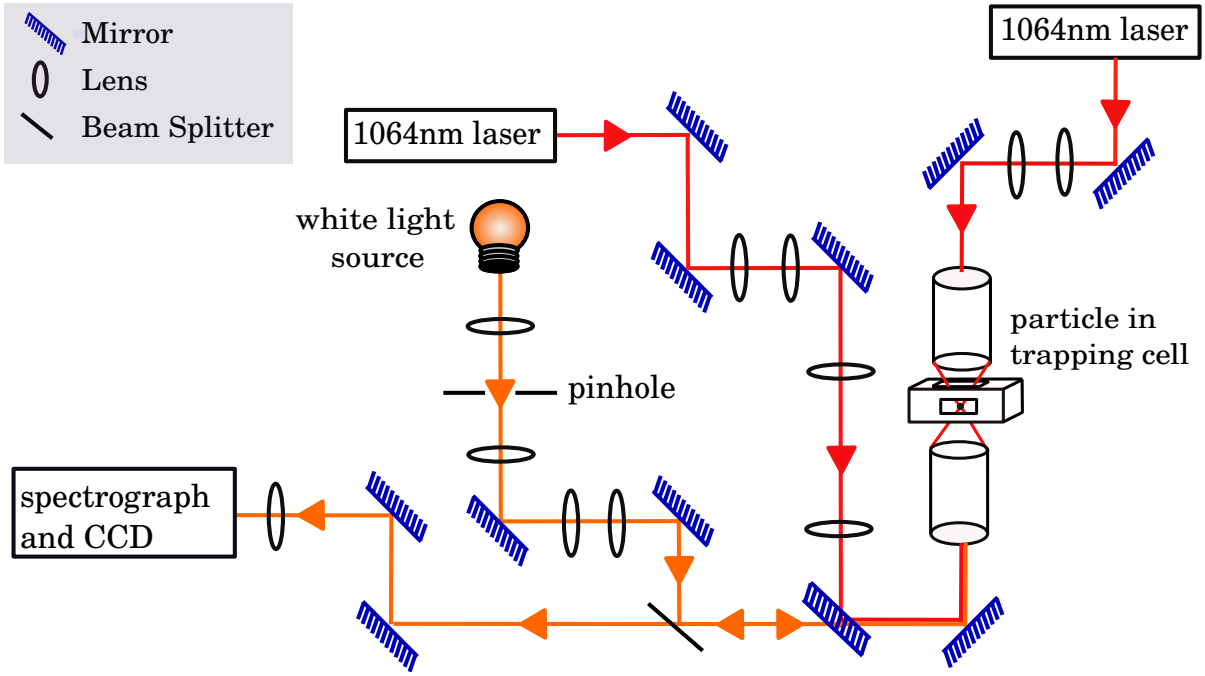

Figure 1: Set-up of optical trap used.

the point of focus) pointing upwards and downwards respectively. The beams were focused into an aluminium trapping cell using two Mitutoyo M Plan Apo x50 NA 0.42 objectives.

The silica beads were aerosolized using an atomizer (Topas, ATM 220) and multiple beads were delivered into the aluminium trapping cell through an inlet in the back of the cell, via a diffusion dryer filled with silica gel. The trapping cell was then adjusted to sub-micron accuracy, using a 3-axis piezo-electric stage (Physik Instrumente), relative to the laser focus until a single bead was trapped at the point of focus. The remaining beads were removed by collisions with the cell walls over a period of approximately 2 minutes.

Aerosol collection and extraction

The aged urban aerosol sample was collected from a site at Royal Holloway, University of London, which is located a few kilometers from three of Englands busiest motorways, and a

very large international airport (Heathrow airport). The wood-smoke sample was collected from the burning of wood from air dried wild cherry trees using a domestic log burner popular as a form of heating domestic houses. Both samples were collected using an air pump which pulled air through clean stainless-steel tubes at a flow rate of 30 lmin^{-1}, onto a Quartz filter (pre-combusted Whatman QM-A) inside a PFA (perfluoroalkoxy) Savillex filter holder. The collected samples were stored in darkness at $-18\,^{\circ}\mathrm{C}$ until the samples were extracted.

To prepare the atmospheric aerosol samples for optical trapping, the quartz filters were each placed in a mixture of 10 ml of chloroform (Sigma-Aldrich, 0.51% ethanol as stabiliser) and 10 ml of ultrapure water. The mixture was then agitated for 10 min to ensure all atmospheric aerosol organic (non-aqueous) extract was dissolved in the chloroform.

The mixture was then filtered through pre-combusted quartz filters to remove filter debris and any unextracted material. The filtrate was poured into a glass-separating funnel and the chloroform layer containing the aerosol extracts was drawn off. The samples were stored in chloroform in darkness at $-18\,^{\circ}\mathrm{C}$ until the experiments were carried out. Finally, the chloroform was removed from the atmospheric aerosol extracts by blowing down under dry nitrogen before the experiments. Once all the chloroform had been removed, the samples were mixed with propan-1-ol was for the experiments.

The filter holder was dissembled in a clean glove box to prevent contamination, and all instrumentation used in the collection and extraction of the samples was cleaned with ultrapure water and chloroform before use.

Uncertainties

The uncertainties in the refractive index and shell thicknesses were found by determining the refractive index and shell thickness of an example particle over 10 consecutive spectra, where the particle properties would not be expected to change. The standard deviation in the refractive indices and shell thickness determined was then taken as the uncertainty for

that parameter. The method used of estimating the uncertainties was carried out on an example particle from each sample, as it combines all sources of error, including changes in the spectrum due to noise, errors in peak finding and all fitting errors, to give an overall estimate of the uncertainty.

Supporting Figures

Figure S2 demonstrates how the shell of a core-shell trapped particle became less volatile and more stable as the volume/thickness of the shell was increased by multiple collisions of organic aerosol with the particle, due to the shell becoming richer in less volatile components.

Figure 2 in the paper shows how a thin film of aged urban aerosol on a silica core was completely removed by oxidation with gas-phase ozone, as the Mie spectra returned to that of pure silica. Figures S3 and S4 here however demonstrates that if a thick enough film is formed, the film will not get completely removed upon reaction with gas-phase ozone, as demonstrated by the fact that the Mie spectra do not return to that of pure silica.

Figure S5 demonstrates the phenomenon that was discovered when fitting the shell thickness and refractive index of the thin films simultaneously. It was found that the core-shell Mie spectra were much more sensitive to shell thickness than refractive index, particularly for thinner films. This is demonstrated in the top panel of the figure as a plot of refractive index against 'average peak difference' which is a measure of how good a fit is, shows a much clearer minimum was determined for thicker shells. Spectra were generated using Philip Lavens Mieplot[1] for this test at a refractive index of 1.52. The bottom panel demonstrates that an equally clear minimum average peak difference can be determined for any thickness of shell from 1 nm.

Figure S6 shows the output spectrum of the Comar 555 LED white light source used in this study to illuminate particles in the trapping chamber.

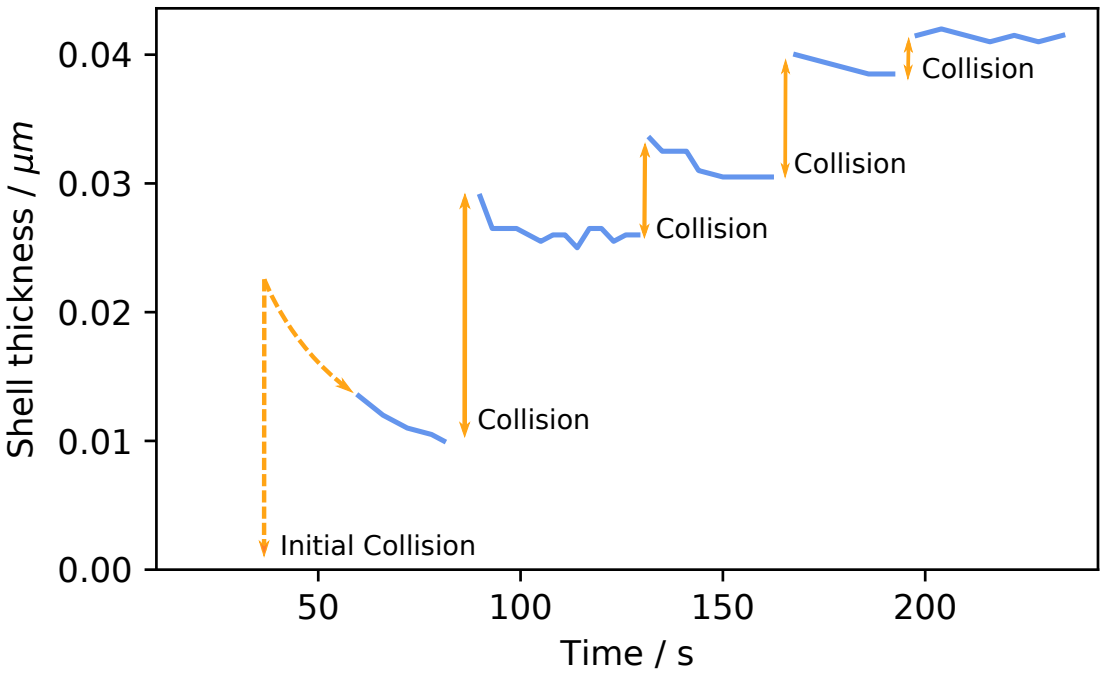

Figure 2: Silica/wood-smoke core-shell particles experienced a sudden increase in radius followed by a slower decrease owing, presumably, to the loss of volatile components within the organic mixture after each collision. The decrease in radius slows with each collision as the mixture forming the film becomes richer in heavier weight films. After 4-5 collisions a thicker film ($\sim$ 40 nm) was formed, assumed to be rich in less volatile components that did not rapidly evaporate, as understood by its constant film thickness with time. The rate of acquisition was too slow to accurately determine the shell thickness at the first collision, the dashed lines show the assumed behaviour during this time.

References

(1) Philip Laven, MiePlot. 2021; `http://philiplaven.com/mieplot.htm`.

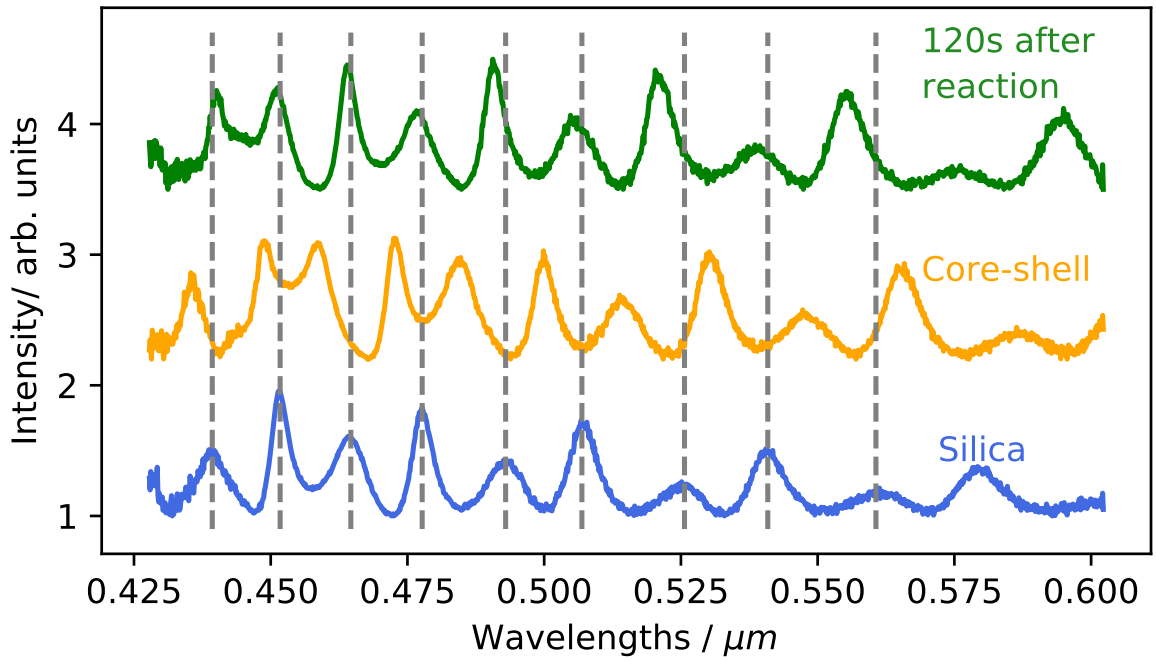

Figure 3: Mie spectra of silica core, silica/urban aerosol core-shell particle 2 before reaction and 120s after reaction, demonstrating that the thin film was not removed from surface completely, leaving a core-shell particle.

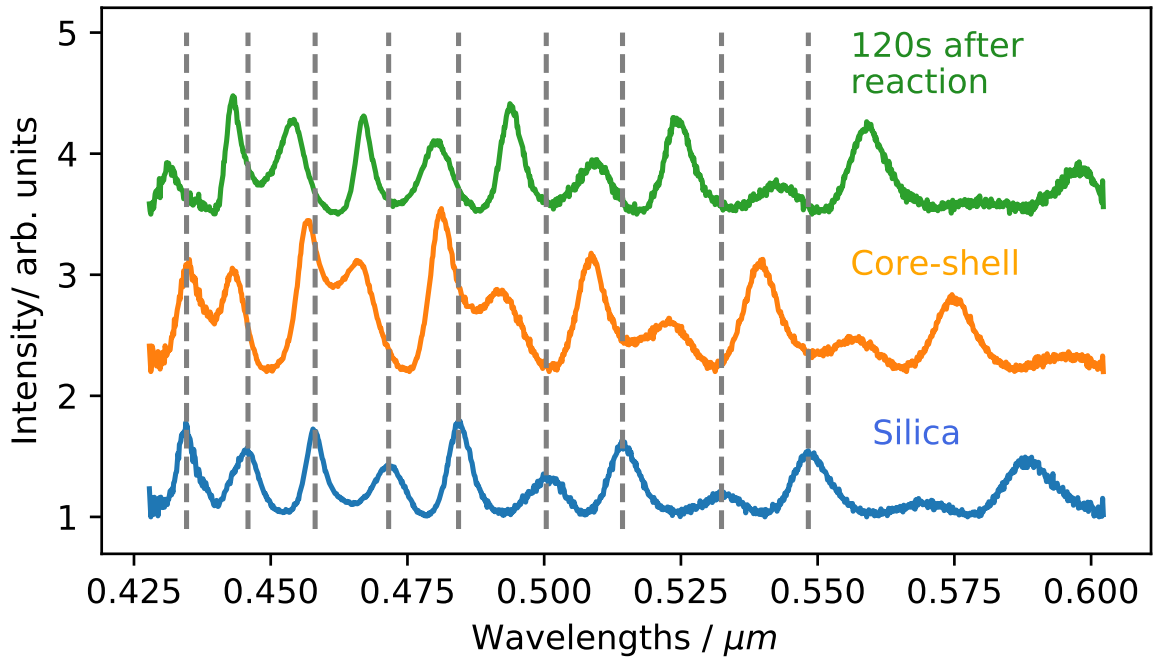

Figure 4: Mie spectra of silica core, silica/urban aerosol core-shell particle 3 before reaction and 120s after reaction, demonstrating that the thin film was not removed from surface completely, leaving a core-shell particle.

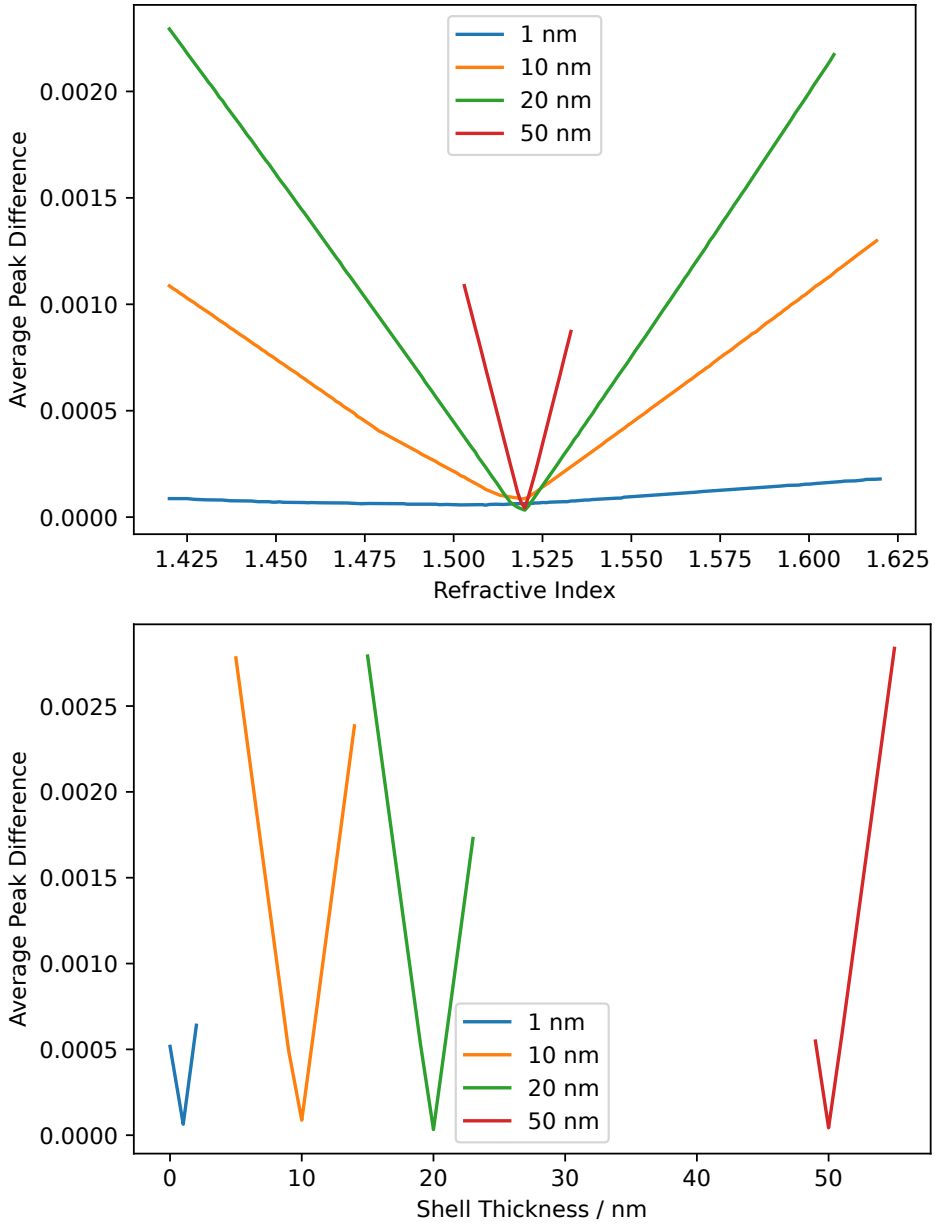

Figure 5: The top panel shows a plot of refractive index against 'average peak difference' for a range of shell thickness' between 1 nm and 50 nm. The correct refractive index for the generated plots studied is 1.52. A much more accurate and precise minimum was determined for thicker shells. The bottom panel demonstrates that an equally clear minimum average peak difference can be determined for any thickness of shell from 1 nm.

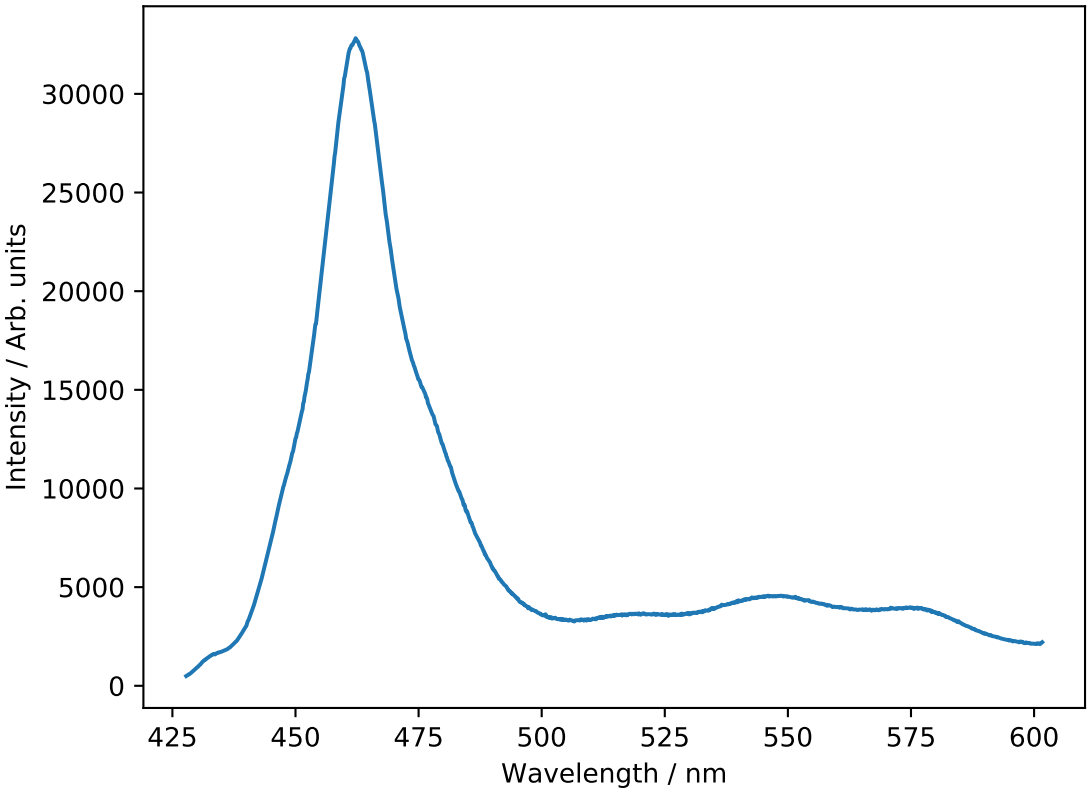

Figure 6: Spectrum of the Comar 555 white LED light source used to study Mie scattering in this study.

Chapter 6

Formation of core-shell particles using silica beads and sulfuric acid

Megan R. McGrory, Rosalie H. Shepherd, Martin D. King, Nicholas Davidson, Francis D. Pope, Matthew Watson, Roy G. Grainger, Anthony C. Jones and Andrew D. Ward

Publication status: Published in the Journal of physical chemistry, chemical physics (PCCP) (February 2022)

I declare I have made the following contributions to the piece of co-authored work:

- Contributed to the conclusions drawn from the experiments conducted
- Developed method for analysis and completed analysis on all data collected

PCCP

ARTICLE TYPE

Cite this: DOI: 00.0000/xxxxxxxxxx

Mie scattering from optically levitated mixed sulfuric acid-silica core-shell aerosols: observation of core-shell morphology for atmospheric science†

Megan R. McGrory,[a,b] Rosalie H. Shepherd,*[a,b] Martin D. King,[b] Nicholas Davidson,[c] Francis D. Pope,[c] I. Matthew Watson,[d] Roy G. Grainger,[e] Anthony C. Jones[f,g] and Andrew D. Ward*[a] †

Received Date
Accepted Date

DOI: 00.0000/xxxxxxxxxx

Sulfuric acid is shown to form a core-shell particle on a micron-sized, optically-trapped spherical silica bead. The refractive indices of the silica and sulfuric acid, along with the shell thickness and bead radius were determined by reproducing Mie scattered optical white light as a function of wavelength in Mie spectroscopy. Micron-sized silica aerosols (silica beads were used as a proxy for atmospheric silica minerals) were levitated in a mist of sulfuric acid particles; continuous collection of Mie spectra throughout the collision of sulfuric acid aerosols with the optically trapped silica aerosol demonstrated that the resulting aerosol had a core-shell morphology. Contrastingly, the collision of aqueous sulfuric acid aerosols with optically trapped polystyrene aerosol resulted in a partially coated system. The light scattering from the optically levitated aerosols was successfully modelled to determine the diameter of the core aerosol (± 0.003 μm), the shell thickness (± 0.0003 μm) and the refractive index (± 0.007). The experiment demonstrated that the presence of a thin film rapidly changed the light scattering of the original aerosol. When a 1.964 μm diameter silica aerosol was covered with a film of sulfuric acid 0.287 μm thick, the wavelength dependent Mie peak positions resembled sulfuric acid. Thus mineral aerosol advected into the stratosphere would likely be coated with sulfuric acid, with a core-shell morphology, and its light scattering properties would be effectively indistinguishable from a homogenous sulfuric acid aerosol if the film thickness was greater than a few 100s of nm.

1 Introduction

Stratospheric aerosols have a large impact on the Earth's climate [1–7]; the scattering of incoming solar radiation [8] depends on the shape, composition and refractive index of the aerosol [5,9,10]. Quantification of the optical properties of stratospheric aerosol is needed to fully understand the influence of stratospheric aerosols upon the planet's radiative balance [11]. Sulfuric acid aerosols are relatively abundant in the stratosphere [12–14]: the number density of sulfuric acid in the stratosphere has been determined from balloon-borne mass spectrometer experiments to be $10^4 - 10^5$ molecules cm^{-3} below an altitude of 30 km and $10^6 - 10^7$ molecules cm^{-3} between 30 to 35 km [15,16]. Anthropogenic emissions, biogenic processes and volcanic emissions act as the major sources of stratospheric sulfuric acid [17–19]. Owing to the abundance of sulfuric acid within the stratosphere, the condensation of sulfuric acid onto other stratospheric aerosol occurs readily [20,21]: Saunders et al. [22] estimated an encounter occurring purely from Brownian motion between a mineral dust particle with a radii of 0.0015 μm and a sulfuric acid aerosol with radii of 0.25 μm would take approximately 4 days. Deshler et al. [23] demonstrated that volcanic eruptions have influenced stratospheric aerosol size distributions for twenty of the last thirty years. Glass fragments make up a large proportion (60 to 80 %) of mineralogy from volcanic eruptions [24] and tend to become coated in sulfuric acid, as shown by U2 flights in Mount St Helen's ash cloud [24]. The formation of a thin film of sulfuric acid on a strato-

[a] a. Central Laser Facility, Research Complex, STFC Rutherford Appleton Laboratory, Oxford, OX11 0FA, UK. E-mail: andy.ward@stfc.ac.uk
[b] b. Department of Earth Sciences, Royal Holloway, University of London, Egham, Surrey, TW20 0EX, UK.
[c] School of Geography, Earth & Environmental Sciences, University of Birmingham, Birmingham, B15 2TT, UK .
[d] School of Earth Science, University of Bristol, Wills Memorial Building, Bristol, BS8 1RJ, UK.
[e] National Centre for Earth Observation, Atmospheric, oceanic and Planetary Physics, University of Oxford, Parks Road, Oxford OX1 3PU, UK.
[f] Met Office, Fitzroy Road, Exeter, EX1 3PB, UK
[g] College of Engineering Maths and Physical Sciences, University of Exeter, Exeter, EX4 4PY, UK

† Electronic Supplementary Information (ESI) available: Raw data for the work presented here is available. See DOI: DOI: 10.5281/zenodo.5041496

spheric mineral aerosol would change the refractive index of the mineral aerosol and hence change the amount of incoming solar radiation that the aerosol scatters[25,26]. Stratospheric mineral aerosol coated in a thin film of stratospheric sulfuric acid could effectively have the optical properties of (a) the mineral aerosol, (b) the mineral aerosol slightly modified by thin film development or (c) sulfuric acid resulting from a core-shell aerosol resembling the sulfuric acid shell to a first approximation. In the study presented, the light scattering from an optically trapped silica bead coated in a thin film of sulfuric acid has been studied. The study will (a) determine that aqueous sulfuric acid can wet and uniformly coat mineral aerosol to form an aerosol with core-shell morphology and (b) record the back-scattered, visible Mie scattered light to size the aerosol and determine the refractive index and shell thickness. Additionally, the Mie scattering as sulfuric acid collides with polystyrene aerosol was monitored: in the presented study it was observed that sulfuric acid did not wet on polystyrene aerosols, thus demonstrating the lack of core-shell geometry. The polystyrene-sulfuric acid system provides an exemplar of a control experiment to demonstrate that a Mie spectra for a non core-shell morphology is readily apparent in the Mie scattering. Comparison between the two systems that used either silica or polystyrene as the core aerosol provided additional evidence for the formation of core-shell aerosol when sulfuric acid collided with silica aerosol. Atmospheric films on liquid or solid aerosols have been studied previously[25,25–42]and inorganic coatings on atmospheric aerosol have also been investigated[26,27,43–45]. For example, Rkiouak et al.[26] applied Raman spectroscopy to follow the development of sulfuric acid films on silica aerosol, whilst Tang et al.[44] studied the heterogeneous reaction of N_2O_5 on silica particles. Film development on atmospheric aerosols has previously been studied through application of optical trapping techniques,[26,27,46]. For example, Jones et al.[25] determined the refractive index change as a film of oleic acid developed on a silica aerosol. Organic coatings of liquid core particles with a mixture of organic materials (from the oxidation of α-pinene) have also been studied[47–51]. Other studies have focused on the deliberate injection of particles into the stratosphere as a method of combating climate change[10,21,52–54]. It is reported that the injection of particles with a large refractive index may greatly increase the amount of solar radiation reflected back to space. Sulfates released into the stratosphere (and which later convert into sulfuric acid[55]) have been suggested as a material to purposefully implant into the stratosphere[56]. However, very little attention has been given to the microphysical interactions between the perturbing material and the ambient stratospheric aerosol layer. Owing to the composition and size of the acid aerosols[52], sulfuric acid does not have the desirable characteristics of a highly reflective aerosol and therefore recent studies have begun to explore other, non-sulfate possibilities such as silica or titania[27,52]. Understanding how a thin film of sulfuric acid alters the scattering properties of the mineral aerosol is crucial to estimate how effective mineral aerosols are at scattering solar radiation.

2 Experimental

To investigate the light scattering from a sulfuric acid film of varying thickness upon a mineral aerosol, single mineral aerosols were optically levitated using vertically aligned, counter-propagating laser beams[57–60]. The counter-propagating laser beams provided a contact free method of levitating aerosols, allowing a replication of airborne processes with the correct aerosol morphology. Mie theory was applied to the backscattered spectrum to determine aerosol radius and refractive index using the relationship between wavelength and refractive index expressed in the Cauchy equation[61]:

$$n = A + \frac{B}{\lambda^2} + \frac{C}{\lambda^4} \quad (1)$$

where the unknown parameters can be determined as a function of wavelength. Within the Cauchy equation, n is the refractive index, λ is wavelength and A, B and C are the Cauchy coefficients. To study core-shell systems, it was important to study the core and shell material separately at the beginning of the study. The application of Mie theory allowed the refractive index of sulfuric acid aerosols and the refractive index and size of the core mineral aerosol to be determined prior to formation of a core-shell system. Afterwards, a film of sulfuric acid could be formed on the silica aerosol from a mist of sulfuric acid in air generated from a bulk aqueous sulfuric acid solution. The airborne aqueous sulfuric acid aerosols wetted and spread on the core mineral aerosol. Backscattered white light was recorded as a function of wavelength to produce a Mie spectra. Mie spectra were continuously collected whilst sulfuric acid aerosols collided with the silica aerosol; the experimental Mie spectra were then simulated allowing the refractive index, radius and film thickness of the core-shell system to be characterised. For the purpose of the study, silica was used as a proxy-mineral aerosol.

2.1 Sulfuric Acid and Silica Aerosol

VWR Chemicals supplied aqueous sulfuric acid as a 50% w/w solution. Dilutions were made by weight using water with conductivity below 18 MΩ cm^{-1}. Spherical silica beads were sourced from Bangs Laboratories Inc., product number SS04N, lot number 7920. The beads are reported as non-porous with a reported density of 2 g cm^{-3} and a radius of approximately 1.035 μm. To determine the refractive index and radius of a trapped aerosol Mie spectroscopy requires the shape of the aerosol to be accurately known, and thus use of mineral aerosol samples extracted from the atmosphere was not possible. Additionally, Bangs Laboratories Inc. supplied polystyrene beads: product number PS04N, lot number 12487. The polystyrene beads had a density of $1.04 - 1.15$ g cm^{-3} and a radius of approximately 1.04 μm.

2.2 Aerosol Generation

An ultrasonic nebuliser (aerosonic travel ultrasonic nebuliser) delivered sulfuric acid aerosols to the sample cell. The radius of the trapped aqueous sulfuric acid aerosol varied from 0.1 μm to over 5 μm. Aerosols in the range 1.4 to 2.0 μm were used for Mie scattering studies. An atomiser (Topas, ATM 220) with diffusion dryer

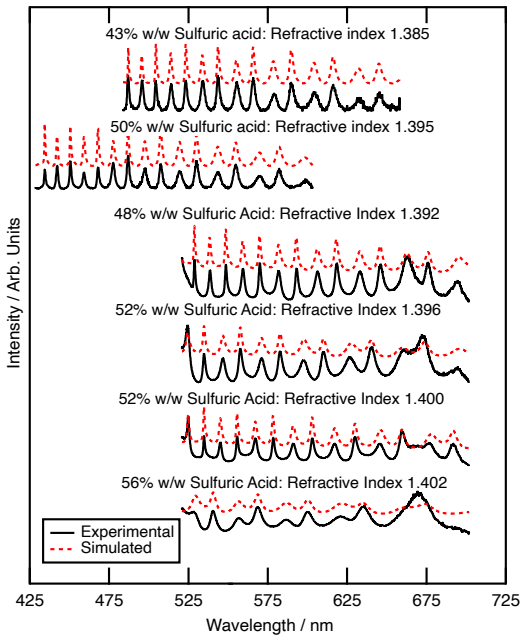

Fig. 1 Measured and simulated Mie spectra for optically trapped sulfuric acid aerosols, each of the six spectra represent a sulfuric acid aerosol that originates from a different concentration bulk aqueous sulfuric acid solution. Simulated Mie spectra for each experimental Mie spectra are additionally shown. The displayed spectra are offset to provide a clear depiction of the spectra.

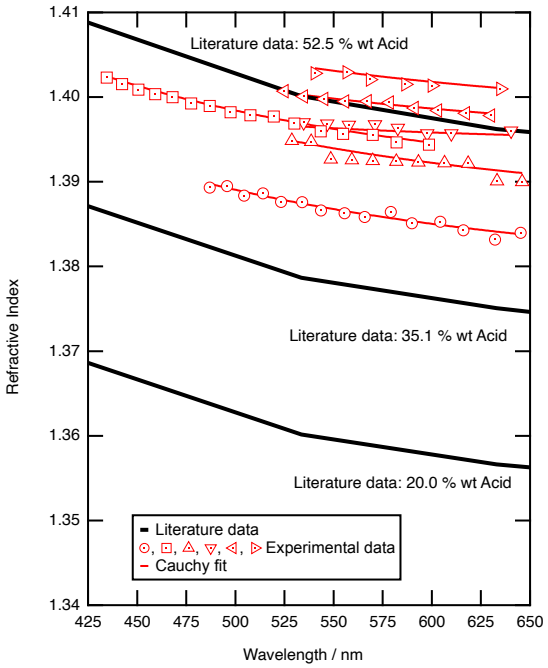

Fig. 2 Experimental (red diamond) refractive index of trapped sulfuric acid aerosols as a function of wavelength are compared to literature values for aqueous sulfuric acid solutions that have different mass ratios of sulfuric acid to water at a temperature of 21°C[62].

(Topas, DDU 570/L) was used to deliver silica and polystyrene to the sample cell from aqueous suspensions. Prior to atomisation, the silica or polystyrene beads were dispersed in water at a concentration of 2 % w/w.

2.3 Optical Trapping

A 1064 nm, continuous wave Nd:YAG laser beam (Ventus, Laser Quantum) was split into two paths. The beams were delivered, via beam expansion optics, to two opposing microscope objective lenses (Mitutoyo NIR ×50, NA 0.42) that focused the two beams to form an optical trap[63]. A piezo-stage (Physik-Instrumente) was used to control the x, y and z positions on the upper laser beam pathway allowing accurate alignment of the focused beams. The power of the laser beam at the point of focus was set to 10 mW for the upward propagating beam and 15 mW for the downwards propagating beam. A simplified schematic of the optical trapping equipment is depicted in Jones et al.[58] Optical trapping techniques have recently been reviewed[64]. A custom-made aluminium sample cell was used as a chamber to trap the aerosols. The cell had two-quarter inch fittings to allow entry of the aerosols and to provide an exhaust path. Windows at the top and bottom allowed the laser beam to enter the cell. Brightfield illumination was configured along the same axis using the lower microscope objective for imaging, with an optical filter to attenuate the laser wavelength. The radius of the trapped aerosol was estimated from images with a resolution of 0.5 μm to provide a coarse starting value for aerosol size when modelling the Mie light scattering with wavelength. Brightfield sources were isolated whilst a spectrum was acquired. Brightfield microscopy allowed imaging of aerosols and the surface. By raising the cover slip the trapped aerosol particle could be placed in a clean location to permit inspection. The deposited aerosol was imaged to validate that a silica bead, surrounded by liquid formed the final aerosol

2.4 Acquisitions and Modelling of Mie Spectra

A white-light LED was focussed on the trapped aerosol and the elastic, backscattered light collected using the microscope objective; the light was then dispersed by a spectrometer onto a charge-coupled device detector (Princeton Instrument Spec 10:400 BR), which recorded light intensity as a function of wavelength. Typically a 600 line mm^{-1} grating dispersed the collected light across a wavelength range of 520 to 600 nm with a resolution of 0.06 nm per pixel as shown in figure 1. Henceforth, in the study presented, the spectrum of the intensity of backscattered light versus wavelength will be called a Mie spectrum. An argon pen-ray lamp was used for the wavelength calibration of the spectrometer. To determine the refractive index and radius of the trapped aerosol, the experimental Mie spectrum was compared to a calculated Mie spectrum produced through application of Mie theory based on Bohren and Huffman[65]; the radius and refractive index was varied until a global minimum was determined with the least squares fitting residual between experimental and theoretical peak positions[58,66]. Additionally, core-shell Mie theory[67,68]

Table 1 The mass ratio of sulfuric acid aerosols increased upon trapping, as determined by Mie theory. A, B and C are the Cauchy coefficients from Equation 1.

Bulk Sulfuric Acid	Sulfuric Acid droplet					
Concentration / % w/w	Radius /μm	Concentration / % w/w	Refractive Index (589 nm)	A	B /nm^2	C /nm^4
5	1.349 ± 0.006	56	1.402 ± 0.007	1.395	2425	1.0×10^7
10	1.459 ± 0.006	50	1.395 ± 0.007	1.386	3105	7.9×10^5
10	1.709 ± 0.006	43	1.385 ± 0.007	1.376	3237	7.4×10^6
10	1.733 ± 0.006	52	1.400 ± 0.007	1.393	2210	3.0×10^6
15	1.605 ± 0.006	52	1.396 ± 0.007	1.394	425	8.5×10^7
20	1.785 ± 0.006	48	1.392 ± 0.007	1.384	2750	8.0×10^7

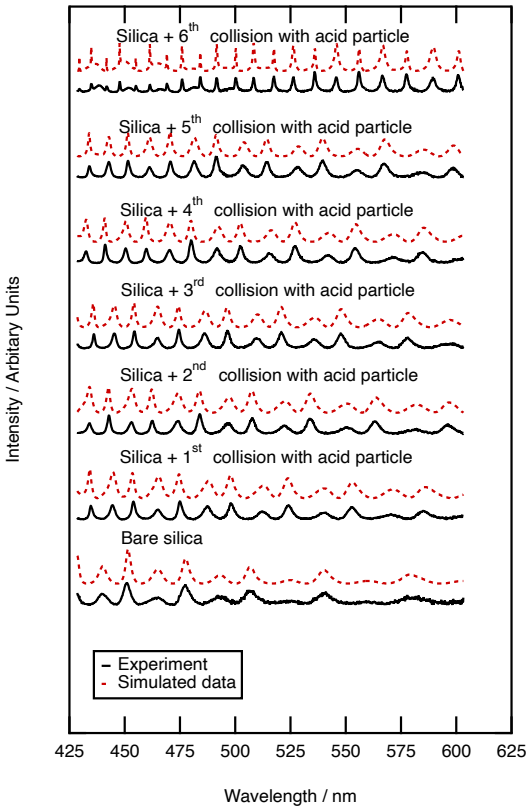

Fig. 3 Mie spectra showing how the Mie scattering of silica aerosol alters upon growth of a film of sulfuric acid. Core-shell Mie theory was applied to determine thickness of the developing shell, the Mie theory simulations are depicted with blue, dashed lines. Seven collisions are depicted: the first collision formed a film of sulfuric acid on the silica of thickness 0.262 μm, whilst the subsequent collisions thickened the film further to a total film thicknesses of $0.287, 0.321, 0.337, 0.369, 0.824$ μm

was applied to calculate the Mie spectra of the core-shell silica-sulfuric acid aerosol; the calculated spectra simulated a series of sulfuric acid films of known thickness on a silica aerosol of known radius and refractive index. The calculated Mie spectra were then compared to experimentally collected core-shell Mie spectra to determine the thickness of the acid film. Further advances in the efficient modelling of core-shell Mie modelling can be found elsewhere[69,70].

3 Results and Disscussion

3.1 Sulfuric Acid

The optical properties of aqueous sulfuric acid has been characterised for a range of sulfuric acid concentrations: Remsburg et al.[71] studied aqueous sulfuric acid in the concentration range 75 to 90 % w/w, whilst Palmer and Williams[72] studied the concentration range 25 to 95.6 % w/w. In more recent years, studies have begun to determine the optical properties of sulfuric acid experiencing stratospheric-like conditions, for example Tisdale et al.[73], Niedziela et al.[74] and Lund-Myhre et al.[75] studied the effect of temperature upon the optical properties of sulfuric acid droplets, whilst Wagner et al.[76] investigated the change in refractive index as a sulfuric acid system was supercooled. In the study presented here, precursory experiments to determine the optical properties, and hence concentration of optically trapped aqueous sulfuric acid aerosols was paramount for calculation of core-shell silica-sulfuric acid systems; the refractive index of optically trapped sulfuric acid was required to create accurate simulations of core-shell silica-sulfuric acid aerosol. Bulk aqueous solutions with the concentrations of 5, 10, 15 or 20 % w/w were prepared and nebulised separately to deliver aerosols to the optical trap.[77] The Mie spectrum for each aerosol was obtained: Figure 2 depicts the experimental and calculated Mie spectra for the aqueous sulfuric acid aerosols for each initial concentration. The refractive index and radius of the optically trapped aerosols are summarised in Table 1. The refractive index can be determined with a precision of 0.007, whilst the radius of the aerosol was determined to $\pm 0.003 \mu$m. Figure 2 compares the refractive index dispersion for the optically trapped sulfuric acid aerosols to literature refractive index dispersions for bulk aqueous sulfuric acid solutions of known mass ratio[78]. The refractive index for experimental sulfuric acid aerosols lie at a refractive index of approximately 1.395 ± 0.007 at 589 nm, which corresponds to a mass ratio of 50 ± 4 % w/w. The mass ratio of sulfuric acid to water of the optically trapped aerosols has increased upon trapping; water has evaporated. The relationship between sulfuric acid concentration and the surrounding environment was demonstrated by Mund and Zellner[79], in particular showing a dependence on the local relative humidity and temperature of the surrounding environment. The relative humidity of the laboratory was measured between 30 and 35 percent during these experiments, which is commensurate with an equilibrium of 50 to 53 % w/w sulfuric acid[80]. The sulfuric acid to water ratio is controlled by local relative humidity, and this is refined by the microenvironment of the

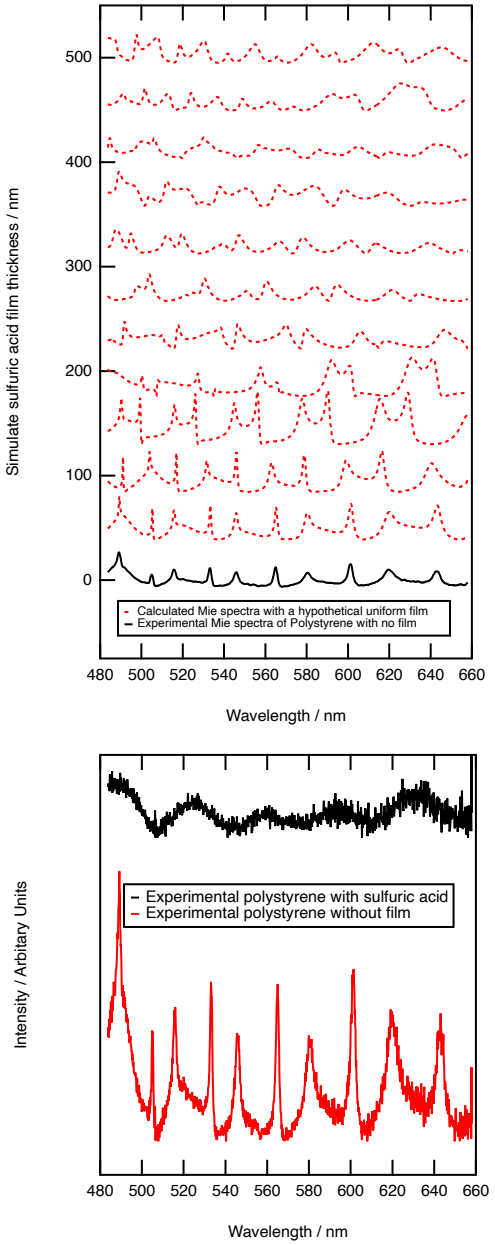

Fig. 4 Graphs depicting (a) the Mie-theory simulated spectra for sulfuric acid film development on the experimental obtained Mie spectrum for pure polystyrene and (b) the experimentally obtained Mie spectra for the growth of a film of sulfuric acid on polystyrene.

aerosol. For all experiments hereafter, it is assumed that nebulised sulfuric acid aerosols will equilibrate with the surrounding environment to reach a concentration of 50 % w/w with a refractive index of 1.395 ± 0.007 at 589 nm; the assumed refractive index will be used in calculations of core-shell silica-sulfuric acid aerosol.

3.2 Silica Aerosol

Simulation of Mie spectra for core-shell aerosols requires the size and refractive index of the core aerosol to be measured first. The silica Mie spectrum depicted in Figure 3 is typical of mineral aerosol.

Eighteen separate silica beads were individually optically trapped and gave an average and standard deviation radius of $0.958 \pm 0.005 \mu$m, whilst the refractive index was measured as 1.383 ± 0.018 at 589 nm. The variation in values of refractive index with wavelength were calculated to be 1.374 ± 0.018, 2763 ± 483 nm^2 and 1×10^8 nm^4 for A, B and C respectively as defined in Equation 1. The measured values of refractive index for silica is notably lower than published values, for example 1.458 at 589 nm was determined by Malitson et al.[78]. Variation in refractive index for different silica samples could be attributed to the mass density of silica.[25] The density determined by the manufacturers and our own densitometer measurements is also lower than bulk silica. Previously low refractive index values of silica beads has been attributed to particle porosity as demonstrated by Tisdale et al.[81] who measured the refractive index for silica beads to range from 1.38 to 1.42; increased porosity would reduce the density of the bead.

3.3 Sulfuric Acid Film Growth on Silica Aerosol

Mie spectra of the optically trapped aerosol were obtained throughout the collision of sulfuric acid with silica aerosol. Figure 3 depicts the Mie light scattering spectra during growth of a film of sulfuric acid upon the silica. The film thickness of the sulfuric acid film was calculated by assuming a constant silica core surrounded by a shell of increasing thickness with the refractive index of a 50 % w/w aqueous sulfuric acid solution. After the first collision, the thickness of the acid film was 0.262 ± 0.0003 μm, requiring a sulfuric acid aerosol with a volume of 4.097 μm^3 to collide with the silica aerosol. After the second collision the film was 0.287 ± 0.0003 μm thick; to develop the film a second sulfuric acid aerosol with a volume of 0.496 μm^3 collided with the silica aerosol. To determine whether the film of sulfuric acid alters the light scattering properties of the core silica aerosol, the Mie scattering properties of the core-shell aerosol were compared with those of pure sulfuric acid.The product of the first collision had a radius of 1.244 ± 0.0003 μm, and has a similar Mie spectrum to a sulfuric acid aerosol with a larger radius of 1.246 μm. The product aerosol particles from the second and all of the subsequent collisions had Mie spectra similar to that of a pure homogenous aerosol particle with the same radius as a core-shell aerosol within error. Therefore, we infer that when a micron-sized sulfuric acid aerosol collides with an optically trapped silica aerosol the resultant core-shell aerosol will begin to resemble a sulfuric acid aerosol of the same diameter as the shell becomes thicker.

3.4 Sulfuric Acid Film Growth on Polystyrene Aerosol

As further evidence for demonstrating the sensitivity of the technique to core-shell aerosol formation, a system unlikely to form a core-shell system was chosen. Hydrophobic polystyrene aerosols were trapped and the collision of aqueous sulfuric acid with the polystyrene followed with Mie spectroscopy. Figure 4a depicts calculated core-shell Mie spectra as a film of sulfuric acid develops on a polystyrene aerosol; the simulation shows an increase in the

number of resonances as the film thickens. Contrastingly, the experimental results depicted in Figure 4b demonstrate a loss of resonances as the sulfuric acid collided with the polystyrene aerosol. The contrast in Mie spectra shown in Figures 4a and 4b indicate that sulfuric acid and polystyrene do not form a core-shell geometry. Owing to the contrast in hydrophobic and hydrophilic nature of polystyrene and aqueous sulfuric acid, the condensation product may represent a partially engulfed system.[47,82]Phase separation between contrasting liquids in aerosols has been extensively studied[83–86]. In particular, Reid et al.[82] investigated the morphology of mixed phase systems through application of optical trapping techniques; concentrating on compounds containing hydrophobic and hydrophilic domains demonstrated that systems containing partitioning constituents do not always form core-shell morphology.

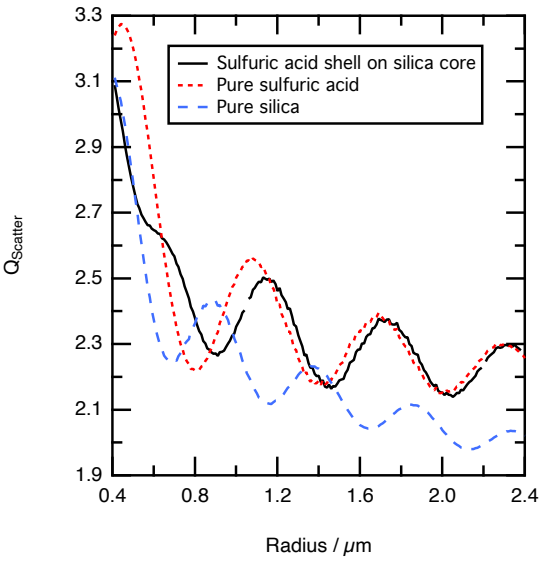

Fig. 5 The scattering efficiency of a silica, a sulfuric acid and core-shell silica-sulfuric acid aerosol particle as a function of median aerosol diameter. $Q_{scatter}$ is calculated over a log-normal size distribution with a geometric standard deviation of 1.5. When the shell upon a 0.8 μm core aerosol is 0.75 μm thick, the optical properties resemble the sulfuric acid shell. The wavelength of light is 532 nm.

3.5 Stratospheric Implications

Owing to the relative abundance of sulfuric acid aerosols residing in the stratospheric aerosol layer[12–14], the consequences of the collision of sulfuric acid aerosols with solid aerosols is highly relevant to understanding the optical scattering efficiency of the stratosphere. The difference in optical properties of a coated aerosol in comparison to an uncoated sphere has drawn significant attention in recent years[25,87–91]: in particular Kahnert et al.[89] has modelled the encapsulation of aggregates by a sulfate film whilst Soewono and Rogak[88] and Wu et al.[90]have explored the effect of a sulfate film on a soot particle.

As demonstrated in the study presented, sulfuric acid collides with a silica aerosol, and then wets and spreads over the surface of the silica aerosol to form a symmetrical core-shell aerosol. Laboratory experiments, at room temperature and pressure, demonstrated that the light scattering properties of the core-shell aerosol system moved rapidly away from the mineral aerosol, and began to represent the Mie spectra of a pure aqueous sulfuric acid aerosol. Assuming similar behaviour at the lower temperatures and pressures of the stratosphere the scattering efficiency of a typical stratospheric silica aerosol was calculated as a function of sulfuric acid film thickness. In the calculation a refractive index of 1.55-0.002i to represent the silica aerosol[24], 1.44-0i to represent sulfuric acid[62,72] and 0.80 μm as the median core diameter[23,24] for a log-normally distributed silica particle size distribution with a geometric standard deviation of 1.5. The shell thickness was increased in 0.03 μm increments until the total diameter of the core-shell system had reached 4.80 μm. The results are compared to the scattering efficiency of a pure sulfuric acid aerosol with the refractive index of 1.44-0i and a pure silica aerosol with the refractive index of 1.55-0.002i in Figure 5. All refractive index values are taken at a wavelength of 532 nm. Figure 5 demonstrates that the structure of the scattering efficiency of the core-shell aerosol begin to represent the shell sulfuric acid quickly; similar results were determined with the laboratory results. As explained in section 3.3, Mie spectra of optically trapped core-shell aerosol represented the Mie spectra of pure aqueous sulfuric acid when the film of the aqueous sulfuric acid becomes thicker. Additionally, Figure 5 depicts the structure and intensity of the scattering efficiency for the core-shell system and sulfuric acid aligning once a film 0.75 μm thick had developed. Consequently, the formation and resultant optical properties of core-shell aerosols ought to be carefully considered in future modelling of stratospheric aerosols.

4 Conclusions

The study presented here demonstrates that sulfuric acid successfully forms a core-shell geometry aerosol upon collision with silica. Through application of optical trapping techniques alongside Mie spectroscopy, it was observed that when a sulfuric acid aerosol collides with a silica aerosol, the system would begin to resemble a sulfuric acid aerosol of similar diameter to the combined aerosol. Secondly, the study experimentally demonstrates that mineral aerosol emitted to the stratosphere will soon adopt the light scattering patterns associated with a pure sulfuric acid aerosol. The implication of the study to stratospheric science is that hydrophilic stratospheric mineral aerosol will rapidly resemble the optical properties of sulfuric acid through natural collision processes and the formation of core-shell morphology.

Conflicts of interest

There are no conflicts to declare.

Data

Raw data for the work presented here is available at the following DOI: 10.5281/zenodo.5041496.

Acknowledgements

The authors are grateful for STFC for allowing access to the optical trapping laboratory at the Central Laser Facility, Rutherford

Appleton Laboratories under the access grant 14230020. Rosalie H. Shepherd would like to thank STFC for funding the student grant ST\L504279\1. Megan McGrory would like to thank NERC for funding of grant NE\R012148 \1. The work presented here has been supported by NERC grant NE/T00732X/1 for ADW and MDK. IMW was funded by EPSRC/NERC/STFC under EP/l01473X/1.RGG was funded as part of NERC's support of the National Centre for Earth Observation grant NE/R016518/1.

Notes and references

1 S. M. Andersson, B. G. Martinsson, J.-P. Vernier, J. Friberg, C. A. M. Brenninkmeijer, M. Hermann, P. F. J. van Velthoven and A. Zahn, *Nature Communications*, 2015, **6**, 7692.

2 R. Auchmann, F. Arfeuille, M. Wegmann, J. Franke, M. Barriendos, M. Prohom, A. Sanchez-Lorenzo, J. Bhend, M. Wild, D. Folini, P. Štěpánek and S. Brönnimann, *Journal of Geophysical Research: Atmospheres*, 2013, **118**, 9064–9077.

3 D. Baumgardner, G. Kok and G. Raga, *Geophysical Research Letters*, 2004, **31**, year.

4 C. Brühl, J. Lelieveld, H. Tost, M. Höpfner and N. Glatthor, *Journal of Geophysical Research: Atmospheres*, 2015, **120**, 2103–2118.

5 A. Lacis, J. Hansen and M. Sato, *Geophysical Research Letters*, 1992, **19**, 1607–1610.

6 G. Myhre, T. F. Berglen, C. E. Myhre and I. S. Isaksen, *Tellus B: Chemical and Physical Meteorology*, 2004, **56**, 294–299.

7 G. Pitari, G. Di Genova, E. Mancini, D. Visioni, I. Gandolfi and I. Cionni, *Atmosphere*, 2016, **7**, 75.

8 O. B. Toon and J. B. Pollack, *American Scientist*, 1980, **68**, 268–278.

9 A. J. Durant, S. P. Harrison, I. M. Watson and Y. Balkanski, *Progress in Physical Geography: Earth and Environment*, 2009, **33**, 80–102.

10 A. C. Jones, J. M. Haywood and A. Jones, *Atmospheric Chemistry and Physics*, 2016, **16**, 2843–2862.

11 K. D. Beyer, A. R. Ravishankara and E. R. Lovejoy, *Journal of Geophysical Research: Atmospheres*, 1996, **101**, 14519–14524.

12 G. K. Yue, L. R. Poole, P.-H. Wang and E. W. Chiou, *Journal of Geophysical Research: Atmospheres*, 1994, **99**, 3727–3738.

13 D. M. Murphy, K. D. Froyd, J. P. Schwarz and J. C. Wilson, *Quarterly Journal of the Royal Meteorological Society*, 2014, **140**, 1269–1278.

14 S. Kremser, L. W. Thomason, M. von Hobe, M. Hermann, T. Deshler, C. Timmreck, M. Toohey, A. Stenke, J. P. Schwarz, R. Weigel, S. Fueglistaler, F. J. Prata, J.-P. Vernier, H. Schlager, J. E. Barnes, J.-C. Antuña-Marrero, D. Fairlie, M. Palm, E. Mahieu, J. Notholt, M. Rex, C. Bingen, F. Vanhellemont, A. Bourassa, J. M. C. Plane, D. Klocke, S. A. Carn, L. Clarisse, T. Trickl, R. Neely, A. D. James, L. Rieger, J. C. Wilson and B. Meland, *Reviews of Geophysics*, 2016, **54**, 278–335.

15 F. Arnold, R. Fabian and W. Joos, *Geophysical Research Letters*, 1981, **8**, 293–296.

16 A. A. Viggiano and F. Arnold, *Geophysical Research Letters*, 1981, **8**, 583–586.

17 S. Solomon, J. S. Daniel, R. R. Neely, J.-P. Vernier, E. G. Dutton and L. W. Thomason, *Science*, 2011, **333**, 866–870.

18 C. A. Brock, P. Hamill, J. C. Wilson, H. H. Jonsson and K. R. Chan, *Science*, 1995, **270**, 1650–1653.

19 R. G. Grainger and E. J. Highwood, *Geological Society, London, Special Publications*, 2003, **213**, 329–347.

20 S. E. Bauer and D. Koch, *Journal of Geophysical Research: Atmospheres*, 2005, **110**, year.

21 D. K. Weisenstein, D. W. Keith and J. A. Dykema, *Atmospheric Chemistry and Physics*, 2015, **15**, 11835–11859.

22 R. W. Saunders, S. Dhomse, W. S. Tian, M. P. Chipperfield and J. M. C. Plane, *Atmospheric Chemistry and Physics*, 2012, **12**, 4387–4398.

23 T. Deshler, *Journal of Geophysical Research*, 2003, **108**, 4167.

24 N. H. Farlow, V. R. Oberbeck, K. G. Snetsinger, G. V. Ferry, G. Polkowski and D. M. Hayes, *Science*, 1981, **211**, 832–834.

25 S. H. Jones, M. D. King and A. D. Ward, *Chem. Commun.*, 2015, **51**, 4914–4917.

26 L. Rkiouak, M. J. Tang, J. C. J. Camp, J. McGregor, I. M. Watson, R. A. Cox, M. Kalberer, A. D. Ward and F. D. Pope, *Phys. Chem. Chem. Phys.*, 2014, **16**, 11426–11434.

27 M. J. Tang, J. C. J. Camp, L. Rkiouak, J. McGregor, I. M. Watson, R. A. Cox, M. Kalberer, A. D. Ward and F. D. Pope, *The Journal of Physical Chemistry A*, 2014, **118**, 8817–8827.

28 E. R. Garland, E. P. Rosen, L. I. Clarke and T. Baer, *Phys. Chem. Chem. Phys.*, 2008, **10**, 3156–3161.

29 Y. Li, M. J. Ezell and B. J. Finlayson-Pitts, *Atmospheric Environment*, 2011, **45**, 4123 – 4132.

30 A. K. Ray, B. Devakottai, A. Souyri and J. L. Huckaby, *Langmuir*, 1991, **7**, 525–531.

31 A. Abo Riziq, M. Trainic, C. Erlick, E. Segre and Y. Rudich, *Atmospheric Chemistry and Physics*, 2008, **8**, 1823–1833.

32 J. B. Gilman, T. L. Eliason, A. Fast and V. Vaida, *Journal of Colloid and Interface Science*, 2004, **280**, 234 – 243.

33 E. González-Labrada, R. Schmidt and C. E. DeWolf, *Phys. Chem. Chem. Phys.*, 2007, **9**, 5814–5821.

34 M. D. King, A. R. Rennie, K. C. Thompson, F. N. Fisher, C. C. Dong, R. K. Thomas, C. Pfrang and A. V. Hughes, *Phys. Chem. Chem. Phys.*, 2009, **11**, 7699–7707.

35 C. Pfrang, F. Sebastiani, C. O. M. Lucas, M. D. King, I. D. Hoare, D. Chang and R. A. Campbell, *Physical Chemistry Chemical Physics*, 2014, **16**, 13220–13228.

36 L. F. Voss, M. F. Bazerbashi, C. P. Beekman, C. M. Hadad and H. C. Allen, *Journal of Geophysical Research: Atmospheres*, 2007, **112**, year.

37 L. F. Voss, C. M. Hadad and H. C. Allen, *The Journal of Physical Chemistry B*, 2006, **110**, 19487–19490.

38 M. D. King, S. H. Jones, C. O. M. Lucas, K. C. Thompson, A. R. Rennie, A. D. Ward, A. A. Marks, F. N. Fisher, C. Pfrang, A. V. Hughes and R. A. Campbell, *Physical Chemistry Chemical Physics*, 2020, 10.1039.D0CP03934A.

39 B. Woden, M. W. A. Skoda, A. Milsom, C. Gubb, A. Maestro, J. Tellam and C. Pfrang, *Atmospheric Chemistry and Physics*, 2021, **21**, 1325–1340.

40 F. Sebastiani, R. A. Campbell, K. Rastogi and C. Pfrang, *Atmospheric Chemistry and Physics*, 2018, **18**, 3249–3268.

41 S. H. Jones, M. D. King, A. D. Ward, A. R. Rennie, A. C. Jones and T. Arnold, *Atmospheric Environment*, 2017, **161**, 274–287.

42 R. H. Shepherd, M. D. King, A. A. Marks, N. Brough and A. D. Ward, *Atmospheric Chemistry and Physics*, 2018, **18**, 5235–5252.

43 M. N. Romanías, H. Ourrad, F. Thévenet and V. Riffault, *The Journal of Physical Chemistry A*, 2016, **120**, 1197–1212.

44 M. J. Tang, P. J. Telford, F. D. Pope, L. Rkiouak, N. L. Abraham, A. T. Archibald, P. Braesicke, J. A. Pyle, J. McGregor, I. M. Watson, R. A. Cox and M. Kalberer, *Atmospheric Chemistry and Physics*, 2014, **14**, 6035–6048.

45 Y. Fang, M. Tang and V. H. Grassian, *The Journal of Physical Chemistry A*, 2016, **120**, 4016–4024.

46 M. D. King, O. R. Hunt, A. D. Ward and C. Pfrang, 3.

47 K. Gorkowski, H. Beydoun, M. Aboff, J. S. Walker, J. P. Reid and R. C. Sullivan, *Aerosol Science and Technology*, 2016, **50**, 1327–1341.

48 K. Gorkowski, N. M. Donahue and R. C. Sullivan, *Environmental Science & Technology*, 2017, **51**, 12154–12163.

49 K. Gorkowski, N. M. Donahue and R. C. Sullivan, *Environmental Science: Processes & Impacts*, 2018, **20**, 1512–1523.

50 K. Gorkowski, N. M. Donahue and R. C. Sullivan, *Chem*, 2020, **6**, 204–220.

51 R. C. Sullivan, H. Boyer-Chelmo, K. Gorkowski and H. Beydoun, *Accounts of Chemical Research*, 2020, **53**, 2498–2509.

52 F. D. Pope, P. Braesicke, R. G. Grainger, M. Kalberer, I. M. Watson, P. J. Davidson and R. A. Cox, *Nature Climate Change*, 2012, **2**, 713–719.

53 K. E. McCusker, D. S. Battisti and C. M. Bitz, *Geophysical Research Letters*, 2015, **42**, 4989–4997.

54 A. Laakso, H. Kokkola, A.-I. Partanen, U. Niemeier, C. Timmreck, K. E. J. Lehtinen, H. Hakkarainen and H. Korhonen, *Atmospheric Chemistry and Physics*, 2016, **16**, 305–323.

55 D. Eatough, F. Caka and R. Farber, *Israel Journal of Chemistry*, 1994, **34**, 301–314.

56 P. J. Rasch, S. Tilmes, R. P. Turco, A. Robock, L. Oman, C.-C. J. Chen, G. L. Stenchikov and R. R. Garcia, *Philosophical Transactions of the Royal Society A: Mathematical, Physical and Engineering Sciences*, 2008, **366**, 4007–4037.

57 A. D. Ward, M. Zhang and O. Hunt, *Opt. Express*, 2008, **16**, 16390–16403.

58 S. H. Jones, M. D. King and A. D. Ward, *Physical Chemistry Chemical Physics*, 2013, **15**, 20735–20741.

59 G. David, K. Esat, I. Ritsch and R. Signorell, *Phys. Chem. Chem. Phys.*, 2016, **18**, 5477–5485.

60 Z. Gong, Y.-L. Pan, G. Videen and C. Wang, *Journal of Quantitative Spectroscopy and Radiative Transfer*, 2018, **214**, 94–119.

61 F. A. Jenkins and H. White, *Fundamentals of optics*, McGraw-Hill, 2001.

62 U. K. Krieger, J. C. Mössinger, B. Luo, U. Weers and T. Peter, *Appl. Opt.*, 2000, **39**, 3691–3703.

63 E. Fällman and O. Axner, *Appl. Opt.*, 1997, **36**, 2107–2113.

64 C. Wang, Y.-L. Pan and G. Videen, *Measurement Science and Technology*, 2021, **32**, 102005.

65 C. F. Bohren and D. R. Huffman, *Absorption and Scattering of Light by Small Particles*, Wiley-VCH Verlag GmbH & Co, 2004.

66 A. K. Ray and R. Nandakumar, *Appl. Opt.*, 1995, **34**, 7759–7770.

67 A. L. Aden and M. Kerker, *Journal of Applied Physics*, 1951, **22**, 1242–1246.

68 O. B. Toon and T. P. Ackerman, *Appl. Opt.*, 1981, **20**, 3657–3660.

69 B. Vennes and T. C. Preston, *Journal of the Optical Society of America A*, 2019, **36**, 2089.

70 B. Vennes and T. C. Preston, *Physical Review A*, 2020, **101**, 063812.

71 E. E. Remsberg, D. Lavery and B. C. Jr, 3.

72 K. F. Palmer and D. Williams, *Appl. Opt.*, 1975, **14**, 208–219.

73 R. T. Tisdale, D. L. Glandorf, M. A. Tolbert and O. B. Toon, *Journal of Geophysical Research: Atmospheres*, 1998, **103**, 25353–25370.

74 R. F. Niedziela, M. L. Norman, R. E. Miller and D. R. Worsnop, *Geophysical Research Letters*, 1998, **25**, 4477–4480.

75 C. E. Lund Myhre, D. H. Christensen, F. M. Nicolaisen and C. J. Nielsen, *The Journal of Physical Chemistry A*, 2003, **107**, 1979–1991.

76 R. Wagner, S. Benz, H. Bunz, O. Möhler, H. Saathoff, M. Schnaiter, T. Leisner and V. Ebert, *The Journal of Physical Chemistry A*, 2008, **112**, 11661–11676.

77 O. R. Hunt, A. D. Ward and M. D. King, *RSC Advances*, 2013, **3**, 19448.

78 I. H. Malitson, *J. Opt. Soc. Am.*, 1965, **55**, 1205–1209.

79 C. Mund and R. Zellner, *ChemPhysChem*, 2003, **4**, 638–645.

80 *Handbook of Chemistry and Physics*, ed. W. M. Haynes, CRC Press, 97th edn, 2016.

81 Z. Hu and D. C. Ripple, *J Res Natl Inst Stand Technol*, 2014, **119**, 674–682.

82 J. P. Reid, B. J. Dennis-Smither, N.-O. A. Kwamena, R. E. H. Miles, K. L. Hanford and C. J. Homer, *Physical Chemistry Chemical Physics*, 2011, **13**, 15559.

83 Y. Qiu and V. Molinero, *Journal of the American Chemical Society*, 2015, **137**, 10642–10651.

84 R. E. O'Brien, B. Wang, S. T. Kelly, N. Lundt, Y. You, A. K. Bertram, S. R. Leone, A. Laskin and M. K. Gilles, *Environmental Science & Technology*, 2015, **49**, 4995–5002.

85 C. Cai, R. E. H. Miles, M. I. Cotterell, A. Marsh, G. Rovelli, A. M. J. Rickards, Y.-h. Zhang and J. P. Reid, *The Journal of Physical Chemistry A*, 2016, **120**, 6604–6617.

86 Y. You and A. K. Bertram, *Atmospheric Chemistry and Physics*, 2015, **15**, 1351–1365.

87 Y. Wu, T. Cheng, X. Gu, L. Zheng, H. Chen and H. Xu, *Journal of Quantitative Spectroscopy and Radiative Transfer*, 2014, **135**, 9 – 19.

88 A. Soewono and S. N. Rogak, *Aerosol Science and Technology*, 2013, **47**, 267–274.

89 M. Kahnert, T. Nousiainen and H. Lindqvist, *Opt. Express*, 2013, **21**, 7974–7993.
90 Y. Wu, T. Cheng, L. Zheng and H. Chen, *Journal of Quantitative Spectroscopy and Radiative Transfer*, 2016, **182**, 1 – 11.
91 S. China, C. Mazzoleni, K. Gorkowski, A. C. Aiken and M. K. Dubey, *Nature Communications*, 2013, **4**, 2122.

6.A Appendix

To keep the paper in this thesis consistent with the published version, the following appendix includes information and clarifications that were requested by the examiners after the paper had been accepted for publication.

Density measurements

It is stated in section 3.2 that measured density values of the silica beads used in this study were lower than that of literature values for the density of bulk silica. The density value measured for this silica, using an Anton Parr densitometer, was 1.96 g/cm^3 and literature values for the density of bulk silica are between 2.2 and 2.65 g/cm^3, meaning the density of the silica beads used had a density value between 0.24 and 0.69 g/cm^3 lower than that of bulk silica.

Non-uniform increase in shell thickness

There were seven collisions of sulfuric acid with the silica particle, each one increasing the thickness of the sulfuric acid shell. The first collision formed a film of sulfuric acid on the silica of thickness 0.262 µm, whilst the subsequent collisions thickened the film further to film thicknesses of 0.287, 0.321, 0.337, 0.369, 0.824 µm. This non-uniform increase in shell thickness is believed to be due to the randomness of the volume of the sulfuric acid droplets being released into the trapping chamber- some are much larger than others, and will therefore increase the shell volume by a much larger amount.

Chapter 7

Discussion and conclusion

The scattering of light by atmospheric aerosol is the largest cause of uncertainty in climate modelling. The aim of the work carried out in this thesis is to provide new methods and information that could be used to reduce this uncertainty in a number of ways. Optical trapping, Mie spectroscopy and computational modeling of Mie spectra were all used to achieve this aim.

The first way in which this work could improve our understanding of atmospheric aerosol is by providing information for increased accuracy of aerosol measurements, both in field experiments using instruments such as nephelometers, and in lab experiments using Mie scattering to study single particles. Polystyrene and silica beads are both commonly used as test aerosol for the calibration of aerosol measuring instrumentation. It has been demonstrated in papers 1 and 2 in this thesis that there are factors affecting the accuracy of these particles as test aerosol which are generally not considered, leading to potential errors in measurements. In paper 1 it is shown that the refractive index of polystyrene beads is dependent on temperature. When taking aerosol measurements in climates above room temperature, the temperature of the polystyrene test aerosol should be considered to avoid error. A simple formula has been provided in paper 1 which can be used to easily determine the refractive index of polystyrene beads at a given temperature and wavelength. This formula has been used by Piszko *et al.* [114] to study bubble growth processes during foaming of thermoplastic polymers. The inclusion of the temperature dependence of the refractive index of polystyrene allowed Piszko *et al.* to achieve more accurate results. In paper 2 information on the size and re-

fractive index values of commercially available silica beads is provided. It is determined in this paper that across the 4 brands studied there is a wide range of values of refractive index ranging from 1.35 – 1.46. This means that when silica beads are used as test aerosol for calibration of equipment there is potentially a very large error in the assumed refractive index of up to 0.11. It is demonstrated in this paper that an error of 0.11 in refractive index could lead to an error in size measurements by a nephelometer of up to 20%. This paper will alert anyone who uses silica beads to use caution when assuming the refractive index of silica beads, and will also provide guidance on which brands produce beads with the most reliable size and refractive index values. For this study it would have been advantageous to have been able to include a larger sample size from each of the brands, however the sample size used was sufficient to show the variation in refractive index values of different silica beads, to determine how accurate the quoted values of each were, and to compare the spread of values amongst the different brands. As the brands that produce the silica beads do not share the exact details of their manufacturing process, it is not possible to know exactly why each of the samples had different results of size and refractive index. It would perhaps be useful to determine the specific details of the Stöber processes which produce silica beads of specific refractive indices for future development of reliable silica beads.

A method has been described in paper 1 for studying airborne particles at high temperatures ($20-240\,^{\circ}C$). Other available methods of determining the temperature dependence of the refractive index of particles require them to be suspended in a liquid medium, thus this method can therefore only be used on solid particles. The method described in paper 1 could be used on solid or liquid atmospheric aerosol proxies to gain an understanding of the effect of high temperatures on the chemistry of airborne aerosol particles produced at high temperatures for example from wildfires, volcanoes etc.

Along with the method described in paper 3 for the study of real atmospheric samples, the effect of high temperatures could also be studied by heating real atmospheric samples. This could provide valuable insight into the effects of aerosol produced during events such as wildfires or volcanic eruptions. Higher temperatures than $240\,^{\circ}C$ could potentially be reached with improved insulation on the heating cell. This method could also be used to determine the temperature dependence of the refractive index of silica beads to add to the information provided in paper 2 for the calibration of equipment using silica particles.

The temperature in the troposphere, which contains almost all atmospheric aerosol, ranges from -60−20 °C [1]. Therefore for atmospherically realistic temperature variation on atmospheric aerosol, it would be beneficial to cool the cell to study aerosol at low temperatures as well. Cooling the cell could potentially be achieved using Peltier cooling, where a DC current is applied across two semiconductors causing a temperature variation where one side gets hotter and the other goes below room temperature. A heat sink keeps the hotter side at ambient temperature while the cold side is used for cooling [115]. Cooling the cell would also allow for the expansion of our results for the refractive index of polystyrene as a function of temperature, to below room temperature. The trapping cell would likely need improved insulation for cooling experiments to be possible.

Although the laser will have a small heating effect on the particle, it is negligible compared with the changes in temperature studied using this method. The heating caused by an optical trap will depend on the laser power and the medium of the specific trap, although the general rule is that the particle will experience 1.45 °C of heating per every 100 mW of laser power for a 1064 nm laser [116, 117]. The laser power used to study the temperature dependence of the refractive index of polystyrene was 15 mW and 10 mW for the top and bottom beams respectively, meaning heating of ∼0.36 °C would be experienced by the particle. This also applies to all other optical trapping experiments carried out in this thesis, meaning that the particles will remain at room temperature and heating by the laser does not need to be taken into consideration.

Another effect that could be caused by the laser when using optical trapping is deformation of the particle. This effect is also dependent on parameters such as medium, laser power and particle size. Counter-propagating optical traps certainly have the potential to deform aerosol particles and are intentionally used for this purpose in 'optical stretching' experiments, for example in a study by Lim *et al.* [118, 119] to study the stretching of red blood cell membranes. However at the laser power used in all experiments in this thesis the deformation of the particles by the laser will be negligible. A study by Rafferty *et al.* [120] showed a 5 µm NaCl droplet to be deformed by 4 nm (0.08%) under a laser power of 1 W. Assuming a linear relationship between percentage deformation and laser power, a typical 2 µm particle studied in this thesis would experience deformation of 1.6 nm (0.08%) at a laser power of 1 W and 0.056 nm (0.0028%) at the 0.035 W laser power typically used.

For the analysis of all aerosol studied in this thesis, a program has been written which can determine the size and wavelength-dependent refractive index of aerosol particles from their Mie spectrum. This program has improved upon the previous method of Mie spectrum analysis by increasing efficiency in two major ways: automation and performance. The automation of the process means that once all the parameters have been set, the code can be left to fit a batch of spectra for long periods of time, including overnight, with no manual effort required. This feature was utilised in papers 1 and 3 as large batches of spectra needed to be analysed when studying the effects of temperature change and oxidation on aerosol particles, over long periods of time. Parallelisation was used to allow multiple theoretical spectra to be generated at once, hugely increasing the speed of the fitting process. This increased the speed compared with previous methods so much so that it allowed for the film thickness and wavelength-dependent refractive index of thin films of organic material on aerosol particles to be determined simultaneously- which was not feasible with previous methods, as it would have taken too much time and a huge amount of manual effort to produce all of the required theoretical spectra and compare them by eye. This means that thin films of unknown refractive index on core-shell particles can be studied using this method. As discussed in section 2.6 core-shell spectra are much less sensitive to changes in refractive index than homogeneous spectra, particularly for core-shell particles with thin films ($<$10 nm). Therefore, the second step in the homogeneous program, the Cauchy fitting step, is not able to be used in the core-shell fitting program as it is not possible to determine the wavelength-dependant refractive index to the precision required for Cauchy fitting, at the refractive indices and shell thicknesses studied. It could potentially be possible to incorportate this step for much thicker shells.

The potential precision of the results obtained by the program for both homogeneous and core-shell particles is dependent on the number and shape of the Mie resonances (peaks) present in the experimental spectrum being studied. More, sharper peaks will generally allow for a better fit with a lower average peak difference in the grid-scan step and a better Cauchy fit in the second step. In paper 1 the Mie spectra produced by the polystyrene beads had many sharp peaks and were ideal examples to first test the program on, and therefore had relatively low uncertainty values of 0.0014 in refractive index and 0.8 nm in radius. In paper 2 some of the silica samples, for example the Corpuscular sample had many sharp peaks and were able to be fitted to a much higher precision than others, such as

the Bangs sample, many of which only had 4-5 broad peaks. Although the Corpuscular silica beads had a similar number of peaks to the polystyrene beads, as the peaks were much broader the calculated uncertainty values for the Corpuscular beads of 0.0022 in refractive index and 1.2 nm in radius, were higher than those for the polystyrene beads, highlighting that both number and shape of peaks are important factors.

A graphical user interface is currently being developed to combine both programs in a much more user-friendly format. The program can then be documented and published online for others in the field to use.

In papers 3 and 4 the morphology of two atmospherically realistic two-phase aerosol particles has been shown to be core-shell. When modelling the scattering of light by sulfuric acid and organic aerosol in the presence of solid mineral aerosol particles, it has been demonstrated that core-shell morphology can be assumed as a first order approximation. Silica beads with the closest refractive index to that of natural silica were able to be chosen for the core based on the results from paper 2. The two-phase particles were assumed to be symmetrical with an even coating of sulfuric acid on the silica core. Modelling of an uneven surface or non-spherical particle was not possible with the computational model available, although the Mie resonances remaining in the Mie spectra when the sulfuric acid was deposited, implies spherical symmetry. Sulfuric acid was also deposited onto polystyrene beads for comparison. When the sulfuric acid collided with the polystyrene particle the Mie resonances in the Mie spectrum disappeared, implying a lack of spherical symmetry, meaning it is likely to have formed a partially-engulfed two-phase particle.

It would have been ideal to confirm this morphology, but it was not possible within this project to model the two-phase polystyrene-sulfuric acid particles as partially-engulfed with the computational models available. There are two computational methods available for modelling the Mie spectra of multi-phase non-spherical particles, the 'T-matrix' method, also known as null field method [121, 122, 123] and the Direct Dipole Approximation method for which the software is named 'DDSCAT' [124]. There are multiple implementations of both of these programs in multiple languages available online. An attempt was made within this project to carry out a fitting procedure using the T-matrix method on the polystyrene/sulfuric acid two-phase particles to confirm a partially-engulfed morphology. However, after $\sim$ 6 months of effort trying to recreate the spectra it was determined that it would not be feasible with this model due to the enormous

quantity of potential shapes that would need to be considered, the huge increase in computational power required to model non-spherical particles, and limitations within the particular implementation of the model used. An attempt was not made to model the particles using DDSCAT as it is primarily designed for modeling forward-scattering of light, and we are studying the back-scatter of light. It was also immediately apparent that it would require an extreme amount of computational power which would not have been easily accessed within the timescale available.

Future studies hoping to model non-spherical two-phase particles should work with a particle system with a predictable morphology, or perhaps in conjunction with other methods of imaging to give an idea of the particles morphology before attempting to model it. To replicate the fitting method used for spherical homogeneous and core-shell particles in this thesis, for non-spherical particles, it would have to be carried out on a supercomputer to obtain results within a reasonable time. In future studies different models could also be used to confirm that the shell formed is uniformly spread across the cores surface, as is assumed in the model used here.

Two-phase particles with core-shell morphology have been previously studied. However, in paper 3, two phase particle made from real atmospheric samples were shown to adopt core-shell morphology for the first time. As there was only a limited amount of both organic samples and it required a large amount of sample being released into the trapping cell to get a single collision of the organic with the silica, it was only possible to obtain spectra of 3 two-phase particles for each sample. It was also difficult to control the amount of collisions, and therefore the volume and thickness of the shell were largely unknown until after the experiment when the results were analysed. While the results obtained were enough to clearly demonstrate the behaviour of thick and thin films of both samples on a silica core it would have been advantageous to have films of a wider range of thicknesses for further comparison.

A further result was obtained from paper 3, when the core-shell particles formed were exposed to ozone. The effect of oxidation on the thickness and refractive index of organic wood-smoke and aged urban aerosol shells on a mineral silica core were shown. The thickness of the shells of both samples were found to decrease upon oxidation. However, the refractive index of the wood-smoke was found to increase, whereas the refractive index of the aged urban sample did not change upon oxidation. This shows that different organic aerosol will have a unique reaction to

oxidation and it is therefore important to study the oxidation of a range of organic aerosol particles in order to get a complete understanding of the effect of oxidation on the scattering properties of atmospheric aerosol. The method used for studying the oxidation of aerosol particles has potential to be used to study many other oxidation reactions, including those at elevated temperatures by combining the methods from papers 1 and 3.

All of the work carried out in this thesis has the potential to decrease the uncertainty in climate modelling introduced by the scattering of light by atmospheric aerosol. This has been achieved by 1) providing information to improve the accuracy of aerosol measurements by instruments which use silica or polystyrene test aerosol for calibration, 2) Providing a new method of analysis of Mie spectra, and 3) Two atmospherically realistic two-phase particles have been shown to form a core-shell morphology, and the effect of oxidation with gas-phase ozone of an organic shell on a mineral core has been presented. This information can be used to improve accuracy in climate models, including General Circulation Models (GCM) which simulate regional climate responses to forcing agents, including atmospheric aerosol.

7.1 Future work

There are many further experiments that could be carried out using the techniques demonstrated in this thesis, and further computational developments that could be made to improve upon the current data analysis capabilities demonstrated.

Polystyrene and silica as calibration aerosol

The aim of the work presented in this thesis is to reduce the uncertainty in the scattering of radiation by atmospheric aerosol. One of the ways this is achieved is through providing information on the optical properties of polystyrene and silica particles, as they are commonly used for calibration of aerosol measuring equipment, such as nephelometers.

It was shown in paper 2 that when silica beads are used as test aerosol for calibration of equipment the error caused by the uncertainty in refractive index of commercially available silica beads could lead to an error in size measurements by a nephelometer of up to 20%. It is believed that

the variation in silica beads is due to differences in the specific Stöber processes used to produce the beads. To better understand this phenomenon a detailed analysis on the effect of different aspects of the Stöber processes on the porosity of the silica beads produced should be carried out. This would allow for the production of more reliable silica beads in the future.

The temperature dependence of the refractive index polystyrene beads was reported in paper 1, which will allow for temperature to be considered when using polystyrene test aerosol for calibration of equipment. A similar study should be carried out on silica beads so the same considerations can be made for equipment being calibrated with silica.

Further heating and oxidation experiments

In this thesis, methods have been demonstrated for determining the optical properties of airborne particles as a function of temperature, and as they are being oxidised. There are many experiments which could be carried out using both of these techniques to provide understanding of the scattering of light by atmospheric aerosol.

The heating method demonstrated could be used to study the effects of heating solid or liquid atmospheric aerosol proxies, or real atmospheric aerosol samples. This could provide understanding of the chemistry of airborne aerosol particles produced at high temperatures for example from wildfires, volcanoes etc.

Different sources of organic aerosol will have a unique reaction to oxidation and it is therefore important to study the oxidation of a range of organic aerosol particles in order to get a complete understanding of the effect of oxidation on the scattering properties of atmospheric aerosol. The method described in paper 3 for studying the oxidation of aerosol particles could be used to study many other oxidation reactions, including those at elevated temperatures by combining the methods from papers 1 and 3.

Developments could be made to the heating setup such that the refractive index at temperatures higher than 240 °C and lower than room temperature could be studied. This could be achieved with improved insulation on the heating cell and cooling of the cell.

All the experiments carried out in this thesis only considered scattering of light in the visible wavelength range. The study of atmospheric aerosol in the UV wavelength range is an incredibly important area of research,

and it would be beneficial to extend any of the results presented here into the UV wavelength range.

Modeling of shaped particles, including partially engulfed

One of the main achievements of this thesis was the development of a computational method for the analysis of the Mie spectra of aerosol with core-shell morphology.

In paper 4, partially-engulfed particles were produced from polystyrene beads and sulfuric acid but it was not possible to confirm this morphology through computational modeling. There are models which can replicate the Mie scattering of partially-engulfed particles. However, to adapt these models into fitting methods similar to those used in this thesis for studying homogeneous and core-shell particles would require access to a supercomputer to obtain results within a reasonable time.

The development of a fitting program for partially-engulfed particles would be a very useful future development. This could perhaps be carried out simply using very powerful computational resources, or in conjunction with other methods of imaging to give an idea of the particles morphology and inform the input to the model.

Bibliography

[1] S. Pandis J. Seinfeld. *Atmospheric Chemistry and Physics*. Vol. 3. Wiley, 2016.

[2] IPCC. *Climate Change 2013: The Physical Science Basis. Contribution of Working Group I to the Fifth Assessment Report of the Intergovernmental Panel on Climate Change*. Cambridge University Press, Cambridge, United Kingdom and New York, NY, USA, 2013.

[3] Terry Deshler. "A review of global stratospheric aerosol: Measurements, importance, life cycle, and local stratospheric aerosol". en. In: *Atmospheric Research*. 17th International Conference on Nucleation and Atmospheric Aerosols 90.2 (Nov. 2008), pp. 223–232.

[4] T. Anderson. "Climate Forcing by Aerosols- A Hazy Picture". In: *Atmospheric Science* 300 (2003), pp. 1103–1104.

[5] A. G. Tlatov A. Kh. Aliev. "Growth in the Atmospheric Aerosol Concentration as a Climate Forcing Agent". In: *Geomagnetism and Aeronomy* 52 (2012), pp. 1107–1112.

[6] Wood R Donner L Rosenfeld D Sherwood S. "Climate Effects of Aerosol-Cloud Interactions". In: *SCIENCE* 343 (2014).

[7] Jiming Sun and Parisa A. Ariya. "Atmospheric organic and bioaerosols as cloud condensation nuclei (CCN): A review". en. In: *Atmospheric Environment* 40.5 (Feb. 2006), pp. 795–820.

[8] Rosalie H. Shepherd et al. "Determination of the refractive index of insoluble organic extracts from atmospheric aerosol over the visible wavelength range using optical tweezers". English. In: *Atmospheric Chemistry and Physics* 18.8 (Apr. 2018), pp. 5235–5252.

[9] G. K. Yue et al. “Stratospheric aerosol acidity, density, and refractive index deduced from SAGE II and NMC temperature data”. en. In: *Journal of Geophysical Research: Atmospheres* 99.D2 (1994), pp. 3727–3738.

[10] D. M. Murphy et al. “Observations of the chemical composition of stratospheric aerosol particles”. en. In: *Quarterly Journal of the Royal Meteorological Society* 140.681 (2014), pp. 1269–1278.

[11] Stefanie Kremser et al. “Stratospheric aerosolObservations, processes, and impact on climate”. en. In: *Reviews of Geophysics* 54.2 (2016), pp. 278–335.

[12] Neil H. Farlow et al. “Size Distributions and Mineralogy of Ash Particles in the Stratosphere from Eruptions of Mount St. Helens”. In: *Science* 211.4484 (1981), pp. 832–834.

[13] Barbara Ervens et al. “Prediction of cloud condensation nucleus number concentration using measurements of aerosol size distributions and composition and light scattering enhancement due to humidity”. In: *Journal of Geophysical Research: Atmospheres* 112.D10 (2007), n/a–n/a.

[14] Muhammad Bilal Altaf et al. “Effect of Particle Morphology on Cloud Condensation Nuclei Activity”. In: *ACS Earth and Space Chemistry* 2.6 (June 2018), pp. 634–639.

[15] Wanguano Li et al. “Formation and Properties of Aerocolloidal TiO2-Coated Microspheres Produced by Alkoxide Droplet Reaction”. en. In: *Journal of Colloid and Interface Science* 162.2 (Feb. 1994), pp. 267–278.

[16] C. Frohlich and Glenn E. Shaw. “New determination of Rayleigh scattering in the terrestrial atmosphere”. In: *Appl. Opt.* 19.11 (June 1980), pp. 1773–1775.

[17] Francis A Jenkins and Harvey Elliott White. *Fundamentals of optics*. New York: Mc Graw-Hill Primis Custom Publ., 2010.

[18] Chelsea L. Price et al. “Simultaneous Retrieval of the Size and Refractive Index of Suspended Droplets in a Linear Quadrupole Electrodynamic Balance”. In: *The Journal of Physical Chemistry A* 124.9 (Mar. 2020), pp. 1811–1820.

[19] Michael I. Cotterell et al. "A complete parameterisation of the relative humidity and wavelength dependence of the refractive index of hygroscopic inorganic aerosol particles". en. In: *Atmospheric Chemistry and Physics* 17.16 (Aug. 2017), pp. 9837–9851.

[20] Michael I. Cotterell et al. "Sensitivity and accuracy of refractive index retrievals from measured extinction and absorption cross sections for mobility-selected internally mixed light absorbing aerosols". In: *Aerosol Science and Technology* 54.9 (Sept. 2020), pp. 1034–1057.

[21] William D. Dick, Paul J. Ziemann, and Peter H. McMurry. "Multi-angle Light-Scattering Measurements of Refractive Index of Submicron Atmospheric Particles". In: *Aerosol Science and Technology* 41.5 (Apr. 2007), pp. 549–569.

[22] Tomoki Nakayama et al. "Measurements of aerosol optical properties in central Tokyo during summertime using cavity ring-down spectroscopy: Comparison with conventional techniques". In: *Atmospheric Environment* 44.25 (Aug. 2010), pp. 3034–3042.

[23] Thomas C. Preston and Jonathan P. Reid. "Determining the size and refractive index of microspheres using the mode assignments from Mie resonances". EN. In: *JOSA A* 32.11 (Nov. 2015), pp. 2210–2217.

[24] Weixiong Zhao et al. "Wavelength-Resolved Optical Extinction Measurements of Aerosols Using Broad-Band Cavity-Enhanced Absorption Spectroscopy over the Spectral Range of 445480 nm". In: *Analytical Chemistry* 85.4 (Feb. 2013), pp. 2260–2268.

[25] Tibor Ajtai et al. "Inter-comparison of optical absorption coefficients of atmospheric aerosols determined by a multi-wavelength photoacoustic spectrometer and an Aethalometer under sub-urban wintry conditions". en. In: *Journal of Aerosol Science* 42.12 (Dec. 2011), pp. 859–866.

[26] Jiumeng Liu et al. "Optical properties and aging of light-absorbing secondary organic aerosol". In: *Atmospheric Chemistry and Physics* 16.19 (2016), pp. 12815–12827.

[27] R. K. Chakrabarty et al. "Brown carbon in tar balls from smoldering biomass combustion". English. In: *Atmospheric Chemistry and Physics* 10.13 (July 2010), pp. 6363–6370.

[28] B. A. Flowers et al. “Optical-chemical-microphysical relationships and closure studies for mixed carbonaceous aerosols observed at Jeju Island; 3-laser photoacoustic spectrometer, particle sizing, and filter analysis”. English. In: *Atmospheric Chemistry and Physics* 10.21 (Nov. 2010), pp. 10387–10398.

[29] Seung Park and Jaemyeong Yu. “Chemical and light absorption properties of humic-like substances from biomass burning emissions under controlled combustion experiments”. In: *Atmospheric Environment* 136 (July 2016), pp. 114–122.

[30] M. Gyawali et al. “In situ aerosol optics in Reno, NV, USA during and after the summer 2008 California wildfires and the influence of absorbing and non-absorbing organic coatings on spectral light absorption”. en. In: *Atmospheric Chemistry and Physics* 9.20 (Oct. 2009), pp. 8007–8015.

[31] P. B. Russell et al. “Absorption Angstrom Exponent in AERONET and related data as an indicator of aerosol composition”. English. In: *Atmospheric Chemistry and Physics* 10.3 (Feb. 2010), pp. 1155–1169.

[32] J. Sandradewi et al. “A study of wood burning and traffic aerosols in an Alpine valley using a multi-wavelength Aethalometer”. en. In: *Atmospheric Environment* 42.1 (Jan. 2008), pp. 101–112.

[33] Yangang Liu and Peter H. Daum. “Relationship of refractive index to mass density and self-consistency of mixing rules for multicomponent mixtures like ambient aerosols”. In: *Journal of Aerosol Science* 39.11 (Nov. 2008), pp. 974–986.

[34] Noémi Utry et al. “Mass specific optical absorption coefficient of HULIS aerosol measured by a four-wavelength photoacoustic spectrometer at NIR, VIS and UV wavelengths”. en. In: *Atmospheric Environment* 69 (Apr. 2013), pp. 321–324.

[35] M. Kanakidou et al. “Organic aerosol and global climate modelling: a review”. English. In: *Atmospheric Chemistry and Physics* 5.4 (Mar. 2005), pp. 1053–1123.

[36] Jonathan P. Reid et al. “The morphology of aerosol particles consisting of hydrophobic and hydrophilic phases: hydrocarbons, alcohols and fatty acids as the hydrophobic component”. In: *Phys. Chem. Chem. Phys.* 13.34 (2011), pp. 15559–15572.

[37] Kyle Gorkowski, Neil M. Donahue, and Ryan C. Sullivan. "Aerosol Optical Tweezers Constrain the Morphology Evolution of Liquid-Liquid Phase-Separated Atmospheric Particles". en. In: *Chem* 6.1 (Jan. 2020), pp. 204–220.

[38] Yuqing Qiu and Valeria Molinero. "Morphology of LiquidLiquid Phase Separated Aerosols". In: *Journal of the American Chemical Society* 137.33 (Aug. 2015), pp. 10642–10651.

[39] Renyi Zhang et al. "Variability in morphology, hygroscopicity, and optical properties of soot aerosols during atmospheric processing". en. In: *Proceedings of the National Academy of Sciences* 105.30 (July 2008), pp. 10291–10296.

[40] C. Xiong and S. K. Friedlander. "Morphological properties of atmospheric aerosol aggregates". en. In: *Proceedings of the National Academy of Sciences* 98.21 (Oct. 2001), pp. 11851–11856.

[41] Daniel P. Veghte, Muhammad Bilal Altaf, and Miriam Arak Freedman. "Size Dependence of the Structure of Organic Aerosol". In: *Journal of the American Chemical Society* 135.43 (Oct. 2013), pp. 16046–16049.

[42] Tianhai Cheng, Yu Wu, and Hao Chen. "Effects of morphology on the radiative properties of internally mixed light absorbing carbon aerosols with different aging status". EN. In: *Optics Express* 22.13 (June 2014), pp. 15904–15917.

[43] Olga Laskina et al. "Size Matters in the Water Uptake and Hygroscopic Growth of Atmospherically Relevant Multicomponent Aerosol Particles". en. In: *The Journal of Physical Chemistry A* 119.19 (May 2015), pp. 4489–4497.

[44] Benjamin J. Dennis-Smither et al. "Phase, Morphology, and Hygroscopicity of Mixed Oleic Acid/Sodium Chloride/Water Aerosol Particles before and after Ozonolysis". In: *The Journal of Physical Chemistry A* 116.24 (June 2012), pp. 6159–6168.

[45] Mijung Song et al. "Morphologies of mixed organic/inorganic/aqueous aerosol droplets". en. In: *Faraday Discussions* 165.0 (2013), pp. 289–316.

[46] Asit K. Ray and R. Nandakumar. "Simultaneous determination of size and wavelength-dependent refractive indices of thin-layered droplets from optical resonances". EN. In: *Applied Optics* 34.33 (Nov. 1995), pp. 7759–7770.

[47] James L. Huckaby and Asit K. Ray. "Layer Formation on Microdroplets: A Study Based on Resonant Light Scattering". en. In: *Langmuir* 11.1 (Jan. 1995), pp. 80–86.

[48] Eva R. Garland et al. "Growth Dynamics and Morphology of Oleic Acid Vapor-Deposited on a Silica Surface". In: *The Journal of Physical Chemistry C* 113.6 (Feb. 2009), pp. 2141–2148.

[49] T. Kaiser, G. Roll, and G. Schweiger. "Investigation of coated droplets in an optical trap: Raman-scattering, elastic-light-scattering, and evaporation characteristics". EN. In: *Applied Optics* 35.30 (Oct. 1996), pp. 5918–5924.

[50] A. Abo Riziq et al. "Extinction efficiencies of coated absorbing aerosols measured by cavity ring down aerosol spectrometry". In: *Atmospheric Chemistry and Physics* 8.6 (Mar. 2008), pp. 1823–1833.

[51] Yasmine Katrib et al. "Products and Mechanisms of Ozone Reactions with Oleic Acid for Aerosol Particles Having CoreShell Morphologies". In: *The Journal of Physical Chemistry A* 108.32 (Aug. 2004), pp. 6686–6695.

[52] Xiaojin Wang et al. "Simulation of the Optical and Thermal Properties of Multiple CoreShell Atmospheric Fractal Soot Agglomerates under Visible Solar Radiation". In: *The Journal of Physical Chemistry C* 123.39 (Oct. 2019), pp. 24225–24233.

[53] Barbara E. Wyslouzil et al. "Experimental evidence for internal structure in aqueousorganic nanodroplets". en. In: *Physical Chemistry Chemical Physics* 8.1 (2006), pp. 54–57.

[54] Alla H. Falkovich et al. "Adsorption of organic compounds pertinent to urban environments onto mineral dust particles". In: *Journal of Geophysical Research: Atmospheres* 109.D2 (Jan. 2004).

[55] Stephanie H. Jones, Martin D. King, and Andrew D. Ward. "The study of thin films on solid aerosol particles using optical trapping and Mie scattering from a broadband white LED". In: *Optical Trapping and Optical Micromanipulation XI*. Vol. 9164. International Society for Optics and Photonics, Sept. 2014, p. 91641X.

[56] Martin D. King, Katherine C. Thompson, and Andrew D. Ward. "Laser Tweezers Raman Study of Optically Trapped Aerosol Droplets of Seawater and Oleic Acid Reacting with Ozone: Implications for Cloud-Droplet Properties". In: *Journal of the American Chemical Society* 126.51 (Dec. 2004), pp. 16710–16711.

[57] James F. Davies et al. "Influence of organic films on the evaporation and condensation of water in aerosol". In: *Proceedings of the National Academy of Sciences of the United States of America* 110(22) (2013), pp. 8807–8812.

[58] D. J. Donaldson and Veronica Vaida. "The Influence of Organic Films at the AirAqueous Boundary on Atmospheric Processes". In: *Chemical Reviews* 106.4 (2006), pp. 1445–1461.

[59] M. O. Andreae and D. Rosenfeld. "Aerosolcloudprecipitation interactions. Part 1. The nature and sources of cloud-active aerosols". In: *Earth-Science Reviews* 89.1 (2008), pp. 13 –41.

[60] Kyle Gorkowski, Neil M. Donahue, and Ryan C. Sullivan. "Emerging investigator series: determination of biphasic coreshell droplet properties using aerosol optical tweezers". en. In: *Environmental Science: Processes & Impacts* 20.11 (Nov. 2018), pp. 1512–1523.

[61] Ciuraru R et al. "Photosensitized production of functionalized and unsaturated organic compounds at the air-sea interface." In: *Scientific Reports* 5 (2015), p. 12741.

[62] James E. Hansen and Larry D. Travis. "Light scattering in planetary atmospheres". In: *Space Science Reviews* 16.4 (Oct. 1974), pp. 527–610.

[63] Posfai M. et al. "Wet and dry sizes of atmospheric aerosol particles: An AFM-TEM Study". In: *Geophysical Research Letters* 25(11) (1998), pp. 1907–1910.

[64] Capel P. D. et al. "Carbon Speciation and Surface Tension of Fog". In: *Environmental Science & Technology* 24(5) (1990), pp. 722–727.

[65] S. Takahama, S. Liu, and L. M. Russell. "Coatings and clusters of carboxylic acids in carbon-containing atmospheric particles from spectromicroscopy and their implications for cloud-nucleating and optical properties". In: *Journal of Geophysical Research: Atmospheres* 115.D1 (2010), n/a–n/a.

[66] Celia N. Cruz and Spyros N. Pandis. "The effect of organic coatings on the cloud condensation nuclei activation of inorganic atmospheric aerosol". In: *Journal of Geophysical Research: Atmospheres* 103.D11 (1998), pp. 13111–13123.

[67] Donaldson D. J. "Adsorption of Atmospheric Gases at the AirWater Interface". In: *Journal of Physical Chemistry* 103(1) (1999), pp. 62–70.

[68] S. H. Jones, M. D. King, and A. D. Ward. "Atmospherically relevant core-shell aerosol studied using optical trapping and Mie scattering". In: *Chem. Commun.* 51.23 (2015), pp. 4914–4917.

[69] Hideto Takekawa, Hiroaki Minoura, and Satoshi Yamazaki. "Temperature dependence of secondary organic aerosol formation by photo-oxidation of hydrocarbons". en. In: *Atmospheric Environment* 37.24 (Aug. 2003), pp. 3413–3424.

[70] Paul E. Sheehan and Frank M. Bowman. "Estimated Effects of Temperature on Secondary Organic Aerosol Concentrations". In: *Environmental Science & Technology* 35.11 (June 2001), pp. 2129–2135.

[71] Philip B. Russell and Patrick Hamill. "Spatial Variation of Stratospheric Aerosol Acidity and Model Refractive Index: Implications of Recent Results". EN. In: *Journal of the Atmospheric Sciences* 41.11 (June 1984), pp. 1781–1790.

[72] Maofa Ge et al. "Important Oxidants and Their Impact on the Environmental Effects of Aerosols". In: *The Journal of Physical Chemistry A* (Mar. 2021).

[73] J. M. Flores et al. "Evolution of the complex refractive index in the UV spectral region in ageing secondary organic aerosol". English. In: *Atmospheric Chemistry and Physics* 14.11 (June 2014), pp. 5793–5806.

[74] Hwajin Kim, Brian Barkey, and Suzanne E. Paulson. "Real refractive indices of - and -pinene and toluene secondary organic aerosols generated from ozonolysis and photo-oxidation". en. In: *Journal of Geophysical Research: Atmospheres* 115.D24 (2010).

[75] Tomoki Nakayama et al. "Effect of Oxidation Process on Complex Refractive Index of Secondary Organic Aerosol Generated from Isoprene". In: *Environmental Science & Technology* 52.5 (Mar. 2018), pp. 2566–2574.

[76] R. M. Varma et al. "Light extinction by secondary organic aerosol: an intercomparison of three broadband cavity spectrometers". English. In: *Atmospheric Measurement Techniques* 6.11 (Nov. 2013), pp. 3115–3130.

[77] Diego Troya Robert C. Chapleski Jr. Yafen Zhang and John R. Morris. "Heterogeneous chemistry and reaction dynamics of the atmospheric oxidants, O3, NO3, and OH, on organic surfaces". In: *Chemical Society Reviews* 45(3) (2016), pp. 3731–3746.

[78] T. L. Eliason et al. "Processing of unsaturated organic acid films and aerosols by ozone". In: *Atmospheric Environment* 37.16 (2003), pp. 2207 –2219.

[79] Alexander Vlasenko, Ingrid J. George, and Jonathan P. D. Abbatt. "Formation of Volatile Organic Compounds in the Heterogeneous Oxidation of Condensed-Phase Organic Films by Gas-Phase OH". In: *The Journal of Physical Chemistry A* 112.7 (2008), pp. 1552–1560.

[80] L Nieto-Gligorovski et al. "Interactions of ozone with organic surface films in the presence of simulated sunlight: impact on wettability of aerosols". In: *Physical Chemistry Chemical Physics* 10.20 (2008), pp. 2964–2971.

[81] C. Y. Lim et al. "Rapid heterogeneous oxidation of organic coatings on submicron aerosols". en. In: *Geophysical Research Letters* 44.6 (2017), pp. 2949–2957.

[82] Ulrich K. Krieger, Claudia Marcolli, and Jonathan P. Reid. "Exploring the complexity of aerosol particle properties and processes using single particle techniques". In: *Chemical Society Reviews* 41.19 (Sept. 2012), pp. 6631–6662.

[83] David J. Griffiths. *Introduction to electrodynamics*. eng. Prentice Hall, 1999.

[84] Lebedev P. N. "Experimental examination of light pressure". In: *Ann. der Physik* 6.433 (1901).

[85] A. Ashkin. "Acceleration and Trapping of Particles by Radiation Pressure". In: *Phys. Rev. Lett.* 24.4 (1970), pp. 156–159.

[86] A. Ashkin and J. M. Dziedzic. "Optical Levitation of Liquid Drops by Radiation Pressure". In: *Science* 187.4181 (1975), pp. 1073–1075.

[87] Arthur Ashkin. "Optical trapping and manipulation of neutral particles using lasers". In: *Biological Sciences - Biophysics* 94.10 (1997), pp. 4853–4860.

[88] Zhiyong Gong et al. "Optical trapping and manipulation of single particles in air: Principles, technical details, and applications". In: *Journal of Quantitative Spectroscopy and Radiative Transfer* 214 (July 2018), pp. 94–119.

[89] Astrid van der Horst et al. "High trapping forces for high-refractive index particles trapped in dynamic arrays of counterpropagating optical tweezers". EN. In: *Applied Optics* 47.17 (June 2008), pp. 3196–3202.

[90] Richard W. Bowman and Miles J. Padgett. "Optical trapping and binding". en. In: *Reports on Progress in Physics* 76.2 (Jan. 2013), p. 026401.

[91] A Ashkin and JM Dziedzic. "Optical trapping and manipulation of viruses and bacteria". In: *Science* 235.4795 (1987), pp. 1517–1520.

[92] Pascal Guyon et al. "Refractive index of aerosol particles over the Amazon tropical forest during LBA-EUSTACH 1999". en. In: *Journal of Aerosol Science* 34.7 (July 2003), pp. 883–907.

[93] Jiang He, Wei Liu, and Yao-Xiong Huang. "Simultaneous Determination of Glass Transition Temperatures of Several Polymers". In: *PLOS ONE* 11.3 (Mar. 2016), e0151454.

[94] Andrew T. Lambe et al. "Relationship between Oxidation Level and Optical Properties of Secondary Organic Aerosol". In: *Environmental Science & Technology* 47.12 (June 2013), pp. 6349–6357.

[95] J. M. Flores et al. "Complex refractive indices in the near-ultraviolet spectral region of biogenic secondary organic aerosol aged with ammonia". In: *Phys. Chem. Chem. Phys.* 16.22 (2014), pp. 10629–10642.

[96] Junling Li et al. "Development and application of the multi-wavelength cavity ring-down aerosol extinction spectrometer". en. In: *Journal of Environmental Sciences* 76 (Feb. 2019), pp. 227–237.

[97] Erik Fällman and Ove Axner. "Design for fully steerable dual-trap optical tweezers". EN. In: *Applied Optics* 36.10 (Apr. 1997), pp. 2107–2113.

[98] Matthew A. Tarr, Guangxuan Zhu, and Richard F. Browner. "Fundamental Aerosol Studies with an Ultrasonic Nebulizer". EN. In: *Applied Spectroscopy* 45.9 (Sept. 1991), pp. 1424–1432.

[99] Gustav Mie. "Beiträge zur Optik trüber Medien, speziell kolloidaler Metallösungen". en. In: *Annalen der Physik* 330.3 (1908), pp. 377–445.

[100] Craig F. Bohren and Donald R Huffman. *Absorption and Scattering of Light by Small Particles*. eng. New edition. Wiley Science Paperback Series. Wiley-VCH, Sept. 2008.

[101] A. D. Ward, M. Zhang, and O. Hunt. "Broadband Mie scattering from optically levitated aerosol droplets using a white LED". In: *Opt. Express* 16.21 (Oct. 2008), pp. 16390–16403.

[102] Arthur L. Aden and Milton Kerker. "Scattering of Electromagnetic Waves from Two Concentric Spheres". In: *Journal of Applied Physics* 22.10 (Oct. 1951), pp. 1242–1246.

[103] Christopher Palmer and Erwin Loewen. *Diffraction grating handbook*. 6th ed. Newport Corporation, 2005.

[104] Stephanie H. Jones, Martin D. King, and Andrew D. Ward. "Determining the unique refractive index properties of solid polystyrene aerosol using broadband Mie scattering from optically trapped beads". In: *Physical Chemistry Chemical Physics* 15.47 (2013), pp. 20735–20741.

[105] L. J. Nugent Lew, Michelle V. Ting, and Thomas C. Preston. "Determining the size and refractive index of homogeneous spherical aerosol particles using Mie resonance spectroscopy". EN. In: *Applied Optics* 57.16 (June 2018), pp. 4601–4609.

[106] Peter R. Conwell et al. "Efficient automated algorithm for the sizing of dielectric microspheres using the resonance spectrum". EN. In: *JOSA A* 1.12 (Dec. 1984), pp. 1181–1187.

[107] Grégory David et al. "Ultraviolet broadband light scattering for optically-trapped submicron-sized aerosol particles". en. In: *Physical Chemistry Chemical Physics* 18.7 (2016), pp. 5477–5485.

[108] Michael Schmitz, Thomas Rothe, and Alwin Kienle. "Evaluation of a spectrally resolved scattering microscope". EN. In: *Biomedical Optics Express* 2.9 (Sept. 2011), pp. 2665–2678.

[109] SciPy 1.0 Contributors et al. "SciPy 1.0: fundamental algorithms for scientific computing in Python". en. In: *Nature Methods* 17.3 (Mar. 2020), pp. 261–272.

[110] Friedrich Menges. *Spectragryph*. 2021.

[111] William M Haynes. *CRC Handbook of Chemistry and Physics*. Vol. 95. CRC Press, 2014.

[112] Philip Laven. *MiePlot*. 2021.

[113] J. Leinonen. *Python code for calculating Mie scattering from single- and dual-layered spheres*.

[114] Maximilian Piszko et al. "Mutual and Thermal Diffusivities in Polystyrene Melts with Dissolved Nitrogen by Dynamic Light Scattering". In: *Macromolecules* 54.12 (June 2021), pp. 5662–5672.

[115] Robert A. Taylor and Gary L. Solbrekken. "Comprehensive system-level optimization of thermoelectric devices for electronic cooling applications". In: *IEEE Transactions on Components and Packaging Technologies* 31.1 (Mar. 2008), pp. 23–31.

[116] Frederic Català et al. “Influence of experimental parameters on the laser heating of an optical trap”. en. In: *Scientific Reports* 7.1 (Nov. 2017), p. 16052.

[117] Steven P. Gross. “8. Application of optical trapsin Vivo”. en. In: *Methods in Enzymology*. Vol. 361. Biophotonics, Part B. Academic Press, Jan. 2003, pp. 162–174.

[118] C. T. Lim et al. “Large deformation of living cells using laser traps”. en. In: *Acta Materialia* 52.7 (Apr. 2004), pp. 1837–1845.

[119] C. T. Lim et al. “Large deformation of living cells using laser traps”. en. In: *Acta Materialia* 52.7 (Apr. 2004), pp. 1837–1845.

[120] Aidan Rafferty et al. “Optical deformation of single aerosol particles”. en. In: *Proceedings of the National Academy of Sciences* 116.40 (Oct. 2019), pp. 19880–19886.

[121] P.C. Waterman. “Matrix formulation of electromagnetic scattering”. In: *Proceedings of the IEEE* 53.8 (Aug. 1965), pp. 805–812.

[122] Michael I. Mishchenko, Larry D. Travis, and Daniel W. Mackowski. “T-matrix computations of light scattering by nonspherical particles: A review”. en. In: *Journal of Quantitative Spectroscopy and Radiative Transfer*. Light Scattering by Non-Spherical Particles 55.5 (May 1996), pp. 535–575.

[123] Michael I. Mishchenko, Li Liu, and Daniel W. Mackowski. “Morphology-dependent resonances of spherical droplets with numerous microscopic inclusions”. EN. In: *Optics Letters* 39.6 (Mar. 2014), pp. 1701–1704.

[124] Bruce T. Draine and Piotr J. Flatau. “DDSCAT: The discrete dipole approximation for scattering and absorption of light by irregular particles”. In: *Astrophysics Source Code Library* (Aug. 2000).